
Electronic Thesis and Dissertation Repository

8-22-2016 12:00 AM

Evaluation of VOC Degradation in Photo-Catalytic Air Reactors: TiO₂ Immobilization, Energy Efficiency and Kinetic Modeling

Cristina S. Lugo Vega
The University of Western Ontario

Supervisor
Hugo de Lasa
The University of Western Ontario

Graduate Program in Chemical and Biochemical Engineering
A thesis submitted in partial fulfillment of the requirements for the degree in Doctor of
Philosophy
© Cristina S. Lugo Vega 2016

Follow this and additional works at: <https://ir.lib.uwo.ca/etd>

 Part of the [Catalysis and Reaction Engineering Commons](#), and the [Environmental Engineering Commons](#)

Recommended Citation

Lugo Vega, Cristina S., "Evaluation of VOC Degradation in Photo-Catalytic Air Reactors: TiO₂ Immobilization, Energy Efficiency and Kinetic Modeling" (2016). *Electronic Thesis and Dissertation Repository*. 4019.
<https://ir.lib.uwo.ca/etd/4019>

This Dissertation/Thesis is brought to you for free and open access by Scholarship@Western. It has been accepted for inclusion in Electronic Thesis and Dissertation Repository by an authorized administrator of Scholarship@Western. For more information, please contact wlsadmin@uwo.ca.

Abstract

The high emissions of VOCs from anthropogenic sources are detrimental to both the environment and humans, contributing with ground-level ozone and particle matter formation. All this has an impact on human health both in the short and long term. Heterogeneous photocatalysis provides significant potential for VOC degradation, and the mineralization of VOCs into CO₂ and H₂O. However, the approaches to be used for photocatalyst immobilization in scaled and highly efficient photoreactors are still not well established. Furthermore, there is a lack of reported photonic efficiencies and a shortage of required methods to establish these efficiencies.

To address these issues, this PhD Dissertation reports the study of photonic efficiencies, TiO₂ immobilization and kinetic models in a scaled-up Photo-CREC-Air Reactor using supported TiO₂ on a stainless steel mesh. Acetone and acetaldehyde are considered as model VOC with a 25-320 μmole/L initial concentration range. The irradiation field is experimentally evaluated in order to estimate the photon absorption on the TiO₂ film through macroscopic balances. Absorbed radiation based Quantum Yields (QYs) and Photochemical Thermodynamic Efficiency Factors (PTEFs) are established. This methodology also allows decoupling photocatalyst efficiency and photoreactor efficiency.

TiO₂ coatings are prepared using two methods: an Air Assisted Spray with an Automatized Spinning Coating (TiO₂-AAS-ASC) and a Spread Coating (TiO₂-SCM). TiO₂-AAS-ASC shows a more efficient use of the photocatalyst than the TiO₂-SCM. It is also proven that the TiO₂-AAS-ASC displays homogeneity, limited particle agglomeration and stability under flow. It was found that a TiO₂ film thickness of 6-9 microns is proper for full photon absorption.

Calculated QYs limits are 0.5 and 1.2 for acetone and acetaldehyde. While PTEF limits are 0.10 and 0.24 for acetone and acetaldehyde. These findings are encouraging given they show a high degree of photonic energy utilization.

A series-parallel Langmuir-Hinshelwood based kinetic model describes the photodegradation of acetone and acetaldehyde data well with a 0.97-0.98 range correlation coefficient.

The approach reported in the present PhD Dissertation contributes to clarify key engineering issues of significant value for the scale-up of photocatalytic reactors for air treatment.

Keywords

Air treatment, photocatalysis, TiO₂ immobilization methods, Irradiation, Quantum Yields, and Kinetic Modeling

Acknowledgments

I would like to thank the National Council of Science and Technology in Mexico (CONACyT), for the scholarship awarded to me and the Department of Public Education (SEP), for the supplementary scholarship granted to me.

I would also like to express my immense gratitude to Dr. de Hugo Lasa for being a wonderful advisor and professor. I have learned a great deal from him. It has been a pleasure to work with him developing this very interesting project. Furthermore, I am thankful to Dr. Benito Serrano for his co-advisory role and for his support during my PhD studies.

I would also like to thank my PhD Examination Board: Serge Kaliaguine, Ajay Ray, Shahzad Barghi and Johanna Blacquiere. I appreciate their contributions with their knowledge and valuable feedback for my work.

My sincere thanks to Pastor Solano and Jose Muñoz for their assistance in the development of the experimental part of this PhD project. They shared valuable knowledge in the areas of characterization techniques and photoreactors.

I would like to acknowledge Jesus Moreira and Patricio Valadez Pelayo for their help with the mathematical methods in this work. In addition, I would also express my gratitude to Florencia de Lasa for her great contribution during the preparation of manuscripts and PhD dissertation.

I am appreciative of the assistance and advice of my colleagues, Salvador Escobedo Salas and Gabriela Navarro Tovar. I also would like to thank Sorphia Heng and her family for their unconditional support. I am very grateful to have found people in Canada that make me feel loved. Finally, I would especially like to thank my parents, Maria Salome Vega Niño and Jose Luis Lugo Iñiguez for all their love and support. I am very grateful to have these wonderful parents who did everything in their power to enable me to pursue a high quality education. I thank them for all their work and I would like to dedicate this thesis to them.

Table of Contents

Abstract.....	i
Acknowledgments.....	iii
Table of Contents.....	iv
List of Tables.....	viii
List of Figures.....	x
List of Appendices.....	xviii
Nomenclature.....	xix
Chapter 1.....	1
1 Introduction.....	1
Chapter 2.....	6
2 Literature Review.....	6
2.1 VOC Emissions.....	6
2.2 Techniques and Challenges of Technology for VOC Air Pollution.....	9
2.3 Photocatalytic Oxidation in the Photodegradation of VOCs.....	11
2.4 Reactor Design for Photocatalytic Air Treatment.....	14
2.5 Irradiation Source for Photocatalytic Air Treatment.....	15
2.6 Photo-CREC-Air Reactors.....	16
2.7 Immobilization Methods.....	20
2.8 Energy Efficiencies in Photocatalytic Reactors.....	22
2.9 Photoreaction Kinetics and Kinetic Models.....	24
2.9.1 Langmuir-Hinshelwood Model.....	24
2.10 Future perspectives.....	28
Chapter 3.....	32

3	Scope of Research	32
3.1	General Objectives	32
3.2	Particular Objectives	32
3.2.1	<i>Mesh Characterization - Chapter 5</i>	35
3.2.2	<i>Irradiation Evaluation and Establishment of Energy Efficiency Parameters – Chapter 6</i>	35
3.2.3	<i>Effect of TiO₂ Loading and Photon Utilization while using the TiO₂-SC and TiO₂-AAS-ASC Meshes – Chapter 7</i>	36
3.2.4	<i>Energy efficiency Limits –Chapter 8</i>	36
3.2.5	<i>Kinetic Analysis – Chapter 9</i>	36
	Chapter 4	38
4	Experimental methods	38
4.1	TiO ₂ Photocatalyst Immobilization	38
4.2	Mesh Characterization	40
4.3	Photocatalytic Reactor Setup	41
4.4	Irradiation Measurements	44
4.5	Acetone Photocatalytic Degradation	48
4.6	Adsorption Isotherm	49
4.7	Conclusions	50
	Chapter 5	51
5	Results and Discussion: Characterization of TiO ₂ -SC and TiO ₂ -AAS-ASC	51
5.1	Gravimetric method	51
5.2	Energy Dispersive X-Ray Spectroscopy (EDX)	52
5.3	Scanning Electron Microscopy (SEM)	53
5.4	Stability of the Immobilized TiO ₂ using the TiO ₂ -AAS-ASC Method	56
5.5	Conclusions	57

Chapter 6.....	58
6 Results and Discussion: Energy efficiency evaluation	58
6.1 Quantum Yield.....	58
6.2 Reaction rates for $\bullet OH$ Radicals.....	61
6.3 Radiation Flux Balance and Photon Number.....	64
6.4 Monte-Carlo Evaluation of the Irradiation Field	67
6.5 Photochemical Thermodynamic Efficiency Factor	70
6.6 Conclusions.....	75
Chapter 7.....	76
7 Results and Discussion: Effect of TiO_2 loading and photon utilization on TiO_2 -SC and TiO_2 -AAS-ASC.....	76
7.1 Effect of the TiO_2 Loading	76
7.2 Effect of the Initial Acetone Concentration	77
7.3 Quantum Yields for TiO_2 -SC and TiO_2 -AAS-ASC.....	81
7.4 Physically Based Model for the Effect of TiO_2 Loading.....	85
7.5 Conclusions.....	86
Chapter 8.....	88
8 Results and Discussion: Energy Efficiency Limits in Photo-CREC-Air Reactors	88
8.1 High Acetone and Acetaldehyde Concentrations	88
8.2 PTEFs.....	92
8.3 Practical Limits for QYs and PTEFs	93
8.4 Conclusions.....	94
Chapter 9.....	96
9 Results and Discussion: Kinetic Analysis for the Photodegradation of Acetone and Acetaldehyde ‘	96
9.1 Langmuir Isotherms	98

9.2 Acetone Kinetic Model and Parameter Estimation.....	100
9.2.1 <i>Series- Parallel and L-H Model for Acetone</i>	100
9.2.2 <i>Parameter Estimation for Acetone Photo-Conversion</i>	103
9.2.3 <i>Kinetic Model for Low Concentrations</i>	108
9.3 Acetaldehyde Modeling	110
9.3.1 <i>Series- Parallel and L-H Model for Acetaldehyde</i>	110
9.3.2 <i>Parameter Estimation for Acetaldehyde Photo-Conversion</i>	114
9.4 Significance of the Kinetic Model Developed.....	119
9.5 Conclusions.....	120
Chapter 10.....	122
10 Conclusions and Recommendations	122
10.1 Conclusions.....	122
10.2 Future Work and Recommendations	124
References or Bibliography	125
Appendices.....	138
Curriculum Vitae	157

List of Tables

Table 1. Characteristics of Techniques for VOC Removal.	10
Table 2. Advantages and Disadvantages of Photoreactors for VOC Removal.....	14
Table 3. Artificial UV Mercury Lamp Properties.....	16
Table 4. Summary of Quantum Parameters Reported in the Literature	23
Table 5. Summary of Kinetic Studies for Acetaldehyde Reported in the Literature.....	26
Table 6. Summary of Kinetic Studies for Acetone Reported in the Literature.....	27
Table 7. EDX Analysis of Different Area Sections of the TiO ₂ Coated Stainless Steel Meshes Using TiO ₂ -SC and TiO ₂ -AAS-ASC Methods.....	52
Table 8. Calculated Photon Flux and Irradiation for Three Locations: a) On the surface of the mesh, b) Transmitted through the mesh and c) Reflected by the mesh.	66
Table 9. Parameters considered for MCRT	69
Table 10. Initial Acetone Photoconversion Rates per Unit Photocatalyst Weight in the Photo-CREC-Air Reactor using TiO ₂ -SC and TiO ₂ -AAS-ASC. Three initial acetone concentrations were considered: 25, 37 and 50 µmol/L.	77
Table 11. Langmuir Parameters for the Adsorption of Acetone, Acetaldehyde and Formaldehyde at equilibrium conditions on Immobilized Degussa P25 TiO ₂	99
Table 12. Parameter Boundary Estimation at Initial Conditions.....	104
Table 13. Estimated Parameters with a 0.98 Correlation Coefficient for Acetone Photodegradation using 1% wt% TiO ₂ -AAS-ASC.....	105
Table 14. Cross-Correlation Coefficient Matrix for the Estimated Parameters in the Case of Acetone Photodegradation using 1% wt% TiO ₂ -AAS-ASC.	105

Table 15. Estimated Parameters with a 0.97 Correlation Coefficient for Acetone Photodegradation using 1% wt% TiO ₂ -AAS-ASC.....	110
Table 16. Estimated Parameters with a 0.97 Correlation Coefficient for Acetaldehyde Photodegradation using a 1% wt% TiO ₂ -AAS-ASC mesh.....	114
Table 17. Cross-Correlation Coefficient Matrix for Estimated Parameters. Acetaldehyde Photodegradation using 1% wt% TiO ₂ -AAS-ASC mesh.	115
Table 18. Calibration slopes for the periscopic device	141
Table 19. GC parameters of Injection and Detection	142
Table 20. Calibration Slopes between FID Response and VOC Concentration in the Photo-CREC-Air Reactor	145

List of Figures

Figure 1: Schematization of the VOC Emissions from the Product Manufacturing to Its Final Use and Disposal.	7
Figure 2: VOC Indoor Concentrations in North America Residences since 1990.	7
Figure 3: VOC Emissions by Source in Canada from 1990 to 2014.	8
Figure 4: Schematic Illustration of the Electron-Hole Generation in a Photocatalyst Particle.	11
Figure 5: Molecular Structure of (a) Anatase, (b) Rutile and (c) Brookite.....	13
Figure 6: Schematic Diagram of the 14.7 Liter Photo-CREC Air Reactor.	18
Figure 7: Schematic Diagram of the 14.7 Liter Photo-CREC Air Reactor.	18
Figure 8: Generic Schematic Description of the Parallel-Series Model in the Photodegradation of the Pollutants and Various Intermediate Species.	26
Figure 9: Schematic Description of the Particular Objectives Expected to be Achieved in this PhD Dissertation.	34
Figure 10: Schematic Diagram of the Automatized Spray Coating (ASC) System.	39
Figure 11: a) Photo of the Entire 55.4 cm x 34.7 cm TiO ₂ Coated Stainless Steel Mesh. b) Schematic Representation of the 20 Identified Area Sections of the TiO ₂ Impregnated Mesh Sample. c) Photo of the 1 in ² Impregnated Mesh Considered for Further Analyses.	41
Figure 12: Schematic Diagram of the Photo-CREC Degradation System: (1) Reaction section, (2) Venturi section, (3) Blower, (4) Cooler, (5) Automatic sampling ports and (6) Injection port.	43

Figure 13: (a) Schematic Diagram of the Reaction Section: (1) Surrounding UV lamps, (2) Coated stainless steel mesh, (3) Quartz glass and (4) Perforated plate. (b) Schematic Diagram of the Cross-Flow Air Circulation through the TiO ₂ Coated Mesh in the Photo-CREC-Air Reactor.	44
Figure 14: a) Orientation of the Periscopic Device in the Photo-CREC-Air Reactor. b) Schematics Description of the Periscopic Device Components.	45
Figure 15: a) Schematic Representation of the Irradiation Sample Ports and their Locations (Port 1 and Port 2). Location of the near UV lamps is also provided, b) Description of the Photon Trajectory for Near-UV Lamps, Traversing the Quartz Glass and Reaching the Mesh.	46
Figure 16: (a) Schematic Diagram of the Selected Control Volume for Macroscopic Local Radiation Balances. (b) Schematic Diagram of the Optical Probe Locations in the Photo-CREC-Air Reactor for Radiation Measurements..	47
Figure 17: TiO ₂ Local Weight Loading Distribution on the Mesh Prepared using a) the TiO ₂ -SC method and b) the TiO ₂ -AAS-ASC method.	51
Figure 18: SEM Micrographs of Stainless Steel Mesh Coated with a) 3wt% TiO ₂ using the TiO ₂ -SC and b) 1% TiO ₂ using the TiO ₂ -AAS-ASC.....	53
Figure 19: SEM Micrographs of Measured TiO ₂ Coating Thicknesses Using a) TiO ₂ -SC and b) TiO ₂ -AAS-ASC.	54
Figure 20: Effect of the TiO ₂ loading on the film thickness for a) TiO ₂ -SC and b) TiO ₂ -SC.....	54
Figure 21: SEM Micrographs of the Surface of the Impregnated TiO ₂ : a) TiO ₂ -SC and b) TiO ₂ -AAS-ASC..	55
Figure 22: Changes of TiO ₂ Loading with a TiO ₂ -AAS-ASC Mesh during 1000 Hours of Operation.....	56

Figure 23: Schematic Representation of the Proposed Mechanism for the Photodegradation of Acetone in the Photo-CREC-Air Reactor.	62
Figure 24: Color Mapping of the Radiation Field Distribution in the Photo-CREC-Air Reactor as Measured with a Solatell Spectoradiometer. a) Describes the incident radiation reaching the mesh, b) Describes the reflected radiation from the mesh surface and c) Describes the transmitted radiation traversing the mesh.	65
Figure 25: Experimental and Modeled Irradiation for Incident, Transmitted, Reflected and Absorbed Radiation obtained with the Monte Carlo Model.	69
Figure 26. Schematics of the Energy Balance on the Photocatalyst Surface.....	70
Figure 27. Schematic Description of Enthalpy States with Assumed Hypothetical Intermediate States (Hypothetical path).....	72
Figure 28: Effect of the TiO ₂ Loading on the Initial Reaction Rate per Mesh Irradiated Area when Using the TiO ₂ -SC and the TiO ₂ -AAS-ASC.....	76
Figure 29: Changes of Acetone Concentration with Irradiation Time Using the 1wt% TiO ₂ -AAS-ASC Mesh. Three different initial concentrations were considered: a) 25, b) 37 and c) 50 μmol/L.....	79
Figure 30: Changes of CO ₂ Production for Acetone Photodegradation using the 1wt% TiO ₂ -AAS-ASC Mesh. Three different initial acetone concentrations were considered: a) 25, b) 37 and c) 50 μmol/L.	79
Figure 31: Changes of Acetone Concentration with Irradiation Time using the 3% TiO ₂ -SC Mesh. Three different initial concentrations were considered: a) 25, b) 37 and c) 50 μmol/L.	80
Figure 32: Changes of CO ₂ Production with Acetone Photodegradation Using the 3wt% TiO ₂ -SC Mesh. Three different initial acetone concentrations were considered: a) 25, b) 37 and c) 50 μmole/L.....	80

Figure 33: Calculated QYs during the Photocatalytic Degradation of Acetone Using Immobilized: a) TiO ₂ -SC and b) TiO ₂ -AAS-ASC. Three initial concentrations were considered: 25, 37 and 50 μmol/L.	81
Figure 34: Calculated η _w during the Photocatalytic Degradation of Acetone Using Immobilized: a) TiO ₂ -SC and b) TiO ₂ -AAS-ASC. Three initial concentrations were considered: 25 μmol/L, 37 μmol/L and 50 μmol/L.	83
Figure 35: Schematic Representation of the Particle Agglomeration and the Utilization of Photons on the TiO ₂ Coatings: a) TiO ₂ -AAS-ASC and b) TiO ₂ -SC.	84
Figure 36: Influence of the TiO ₂ Loading on the Initial Acetone Photodegradation in the Photo-CREC-Air Reactor Using a TiO ₂ -AAS-ASC Mesh.	86
Figure 37: a) Acetone Concentration Changes and b) CO ₂ Concentration Changes with Irradiation Time. Three different initial acetone concentrations were used: 50, 124 and 247 μmole/L.	89
Figure 38: Quantum Yields for the Degradation of Acetone at various Irradiation Times. Three different initial acetone concentrations were considered: 50, 124 and 247 μmole/L.	89
Figure 39: a) Acetaldehyde Concentration Changes and b) CO ₂ Concentration Changes with Irradiation Time. Three different initial acetaldehyde concentrations were considered: 65, 162 and 324 μmole/L.	90
Figure 40: Quantum Yields for the Degradation of Acetaldehyde at various Irradiation Times. Three different initial acetaldehyde concentrations were considered: 65, 162 and 324 μmole/L.	90
Figure 41: a) Average QYs for the photodegradation of acetone. Three different initial acetone concentrations were considered: 49.8, 124 and 247 μmole/L. b) Overall QYs for the photodegradation of acetaldehyde. Three different initial acetaldehyde concentrations were considered: 65, 162 and 324 μmole/L.	91

Figure 42: a) PTEFs for the photodegradation of acetone. Three different initial acetone concentrations were considered: 50, 124 and 247 $\mu\text{mole/L}$. b) PTEFs for the photodegradation of acetaldehyde. Three different initial acetaldehyde concentrations were considered: 65, 162 and 324 $\mu\text{mole/L}$	92
Figure 43: Changes in the Initial <i>PTEFs</i> and <i>QYs</i> with the Initial Concentrations of Acetone and Acetaldehyde.	93
Figure 44: a) Langmuir Adsorption Isotherm of Acetone, Acetaldehyde and Formaldehyde on Degussa P25 TiO_2	99
Figure 45: Schematic Representation of the Proposed Mechanism for the Photodegradation of Acetone in the Photo-CREC-Air Reactor.	101
Figure 46: Effect of the Initial Acetone Concentration on the Initial Reaction Rate of Acetone and CO_2	104
Figure 47: Comparison of the Experimental Data and the L-H Model using the 3 Fitted Parameters for the Photodegradation of Acetone using 1% wt% TiO_2 -AAS-ASC.....	106
Figure 48: Acetone Concentration Changes with Irradiation Time using the 1% wt% TiO_2 -AAS-ASC. Codes: a) Empty Symbols Shows Experimental Concentrations; b) Full Lines Describes Concentration as per the L-H Method Five initial concentrations of acetone were considered: a) 124, 247 $\mu\text{mole/L}$; b) 25, 37 and 50 $\mu\text{mole/L}$	106
Figure 49: CO_2 Concentration Changes with Irradiation Time during the Photocatalytic Degradation of Acetone using the 1% wt% TiO_2 -AAS-ASC. Empty Symbols Shows Experimental Data, Full line displays L-H Model Predictions. Five initial concentrations of acetone were considered: a) 124, 247; b) 25, 37 and 50 $\mu\text{mole/L}$	107
Figure 50: Total Carbon Concentration in both gas and solid phases during Photocatalytic Degradation of Acetone using the 1% wt% TiO_2 -AAS-ASC at various irradiation times. Filled Symbols shows experimental data, Full lines represent L-H Model Predictions.	

Five initial concentrations of acetone were used: a) 124, 247; b) 25, 37 and 50 $\mu\text{mole/L}$	108
Figure 51: Changes of Acetone and CO_2 Concentrations and the estimated concentration profiles obtained by L-H method using the 1%wt% TiO_2 -AAS-ASC. Five initial concentrations of acetone were considered: 25, 37 and 50 $\mu\text{mol/L}$	110
Figure 52: Concentration Profiles during the Photodegradation of 324 $\mu\text{mole/L}$ Acetaldehyde on 1% wt% TiO_2 -AAS-ASC. a) Acetaldehyde, CO_2 b) Formaldehyde, Formic Acid and Methanol.	111
Figure 53: Schematic Representation of the Proposed Mechanism for the Photodegradation of Acetaldehyde in the Photo-CREC-Air Reactor.....	112
Figure 54: Schematic Representation of the Simplified Proposed Mechanism for the Photodegradation of Acetaldehyde in the Photo-CREC-Air Reactor.....	112
Figure 55: Comparison of the Experimental Data and the L-H Model Using 3 Fitted Parameters for the Photodegradation of Acetaldehyde using 1%wt% TiO_2 -AAS-ASC mesh.	115
Figure 56: Changes of Acetaldehyde Concentration with irradiation time. Empty symbols represent experimental data and full lines calculated concentrations obtained by L-H Model using the 1%wt% TiO_2 -AAS-ASC mesh. Five initial concentrations of acetaldehyde were considered: a) 31, 45 and 59 $\mu\text{mole/L}$; b) 152, 316 $\mu\text{mole/L}$	116
Figure 57: Changes CO_2 Concentrations with Irradiation time. Empty Symbols Export Experimental Data. Full lines describe Calculated Concentration Profiles Obtained by L-H Model, Using the 1%wt% TiO_2 -AAS-ASC mesh. Five initial concentrations of acetaldehyde were considered: a) 31, 45 and 59 $\mu\text{mole/L}$; b) 152, 316 $\mu\text{mole/L}$	117
Figure 58: Changes of One Carbon Containing Species Concentrations with Irradiation Time. Empty Symbols represent Experimental Data and Full lines describe Concentration Profiles Obtained by L-H Method Using the 1%wt% TiO_2 -AAS-ASC.	

Five initial concentrations of acetaldehyde were considered: a) 31, 45 and 59 $\mu\text{mole/L}$; b) 152, 316 $\mu\text{mole/L}$	117
Figure 59: Changes of Total Carbon Concentration in the Gas and Solid Phases with Irradiation time. Empty symbols represent Experimental Data and Full Lines Calculated Concentration by L-H Model Using the 1% wt% $\text{TiO}_2\text{-AAS-ASC}$. Five initial concentrations of acetaldehyde were considered: a) 31, 45 and 59 $\mu\text{mole/L}$; b) 152, 316 $\mu\text{mole/L}$	118
Figure 60: a) Schematic representation of the photons reaching the semiconductor surface through the TiO_2 film, b) Incident photons moving through the photocatalyst film as represented by the RTE model as shown in Appendix H.	120
Figure 61: Effect of the Air Pressure in the Atomized TiO_2 Slurry Flow	139
Figure 62: Spectral Intensity of a Polychromatic EiKO Global UV Lamp.	140
Figure 63: Calibration of the Periscopic Device in respect with the Optic Probe	141
Figure 64: GC parameters of the column separation method	142
Figure 65: Chromatogram obtained during the photodegradation of acetaldehyde in the Photo-CREC-Air reactor.....	143
Figure 66: Chromatogram obtained during the photodegradation of acetone in the Photo-CREC-Air reactor.	143
Figure 67: Full chromatogram obtained during the photodegradation of acetaldehyde in the Photo-CREC-Air reactor using automatized multi-injection.....	144
Figure 68: Full chromatogram obtained during the photodegradation of acetone in the Photo-CREC-Air reactor using automatized multi-injection.....	144
Figure 69: Calibration curves of acetone, acetaldehyde and CO_2	145
Figure 70: Calibration curves of methanol and acetaldehyde.....	145

Figure 71: Concentration monitoring of acetone and CO ₂ with time at dark conditions with no mesh. A wide concentration range was considered (25-250 μmole/L).	146
Figure 72: Differential equations in MATLAB code for parameter estimation. Photodegradation of acetone with acetaldehyde as intermediate species was considered.	154
Figure 73: Differential equations in MATLAB code for parameter estimation. Photodegradation of acetone with no intermediate species was considered.....	155
Figure 74: Differential equations in MATLAB code for parameter estimation. Photodegradation of acetaldehyde with enclosed 1 carbon intermediate species was considered.	156

List of Appendices

Appendix A: Proposed Mechanism of OH^\bullet Radical Formation.....	138
Appendix B: Effect of the Air Pressure in the TiO_2 Slurry Volumetric Flow and Selected AAS Conditions.....	139
Appendix C: Spectral Intensity and Radiation Distribution of the UV Lamps	140
.Appendix D: Calibration of the Periscopic Device with Optic Probe	140
Appendix E: GC Parameters, Chromatograms and Calibration Curves.....	141
Appendix F: Photo-CREC-Air Reactor Leaks.....	146
Appendix G: Evaluation of the Heat of Formation of OH^\bullet Groups.	146
Appendix H: Radiative Transfer for Photon Absorption in the Film	148
Appendix I: Electron-hole Kinetics	151
Appendix J: Physical Based Model for Photoactivity on the Film as a Function of Coating Thickness.	152
Appendix K: Parameter Estimation Coding for Differential Equations.	154

Nomenclature

Arabic letters

A_{irr}	irradiated mesh area holding the catalyst, cm^2	P_{ref}	rate of photons reflected by the TiO_2 coated mesh (photon/s)
A_c	coated mesh area, cm^2	P_{trans}	rate of photons passing through the TiO_2 coated mesh (photon/s)
E_{av}	average energy of a photon at a wavelength range, J/mole photon	$q(\theta, z, \lambda)$	irradiation measured by the spectrometer ($\text{W}/\text{cm}^2\text{-nm}$)
K'_i	linear adsorption constant of species "i", dimensionless	<i>PTFE</i>	Photochemical Thermodynamic Efficiency Factor
K^A_i	adsorption constant of species "i", $1/\mu\text{mole}$	Q	energy (J/min)
k^k_i	kinetic constant of the reaction step j ($\mu\text{mole}/\text{cm}^2_{irr}\text{-min}$)	$Q_{absorbed}$	photon energy absorbed by the photocatalyst (J/min)
C_C	total carbon concentration, $\mu\text{mole}/\text{l}$	Q_{lost}	energy lost during the OH^\bullet formation process (J/min)
C_i	total concentration of species "i", $\mu\text{mole}/\text{l}$	Q_{used}	energy used for mineralization of the pollutant (J/min)
$C_{i,0}$	concentration of species "i" at $t=0$, $\mu\text{mole}/\text{l}$	Q_i	amount of species adsorbed on the solid, $\mu\text{mole}/\text{g}_{cat}$
$C_{i,g}$	concentration of species "i" in the gas phase, $\mu\text{mole}/\text{l}$	$Q_{i,max}$	maximum amount of species adsorbed on the solid, $\mu\text{mole}/\text{g}_{cat}$
$C_{i,s}$	concentration of species "i" in the solid phase, $\mu\text{mole}/\text{l}$	<i>QY</i>	quantum yield based on $\bullet\text{OH}$ radical consumption
C_e	equilibrium pollutant concentration, $\mu\text{mole}/\text{L}$	r	radiation measurement radius (cm)
L_{opt}	optimum TiO_2 coating thickness, cm	$r_{i,g}$	reaction rate of species "I" in the gas phase, $\mu\text{mole}/\text{cm}^2_{irr}\text{-min}$
N_i	number of moles of i (μmole)	$r_{i,j}$	reaction rate of component i in reaction step j , $\mu\text{mole}/\text{cm}^2_{irr}\text{-min}$
P	rate of photons (photon/s)	$r_{i,T}$	total reaction rate of species "I", $\mu\text{mole}/\text{cm}^2_{irr}\text{-min}$
P_{abs}	rate of photons adsorbed by the TiO_2 surface (photon/s)	V	total system volume, L
P_{irr}	rate of photons reaching the surface of the TiO_2 coated mesh (photon/s)	W	photocatalyst weight (g_{cat})
P_{ref}	rate of photons reflected by the TiO_2 coated mesh (photon/s)		

Greek letters

α	fraction of acetone following the partial oxidation step to acetaldehyde	$\Delta H^{\circ}_{f,OH^{\bullet}_{ads}}$	standard enthalpy of formation of OH^{\bullet} (J/mole)
ε	TiO ₂ coating porosity	$\Delta H^{\circ}_{f,O_2(g)}$	standard enthalpy of formation of O ₂ (J/mole)
$\eta_{OH^{\bullet}}$	fraction of photon energy used in forming an OH^{\bullet} radical	$\Delta H^{\circ}_{f,H_2O(g)}$	standard enthalpy of formation of H ₂ O (J/mole)
η_w	quantum yield per photocatalyst weight, 1/g	<i>IC</i>	refer to organic species containing one carbon in their structure
$\eta_{w, optimum}$	optimum quantum yield per photocatalyst weight, 1/g	Subscripts	
ρ_{TiO_2}	mass density of TiO ₂ , g/cm ³	<i>abs</i>	absorbed
$\nu_{\bullet OH}$	stoichiometric coefficient for the consumption of the $\bullet OH$ radical	<i>acetone</i>	refer to acetone species
$\nu_{Acetone}$	stoichiometric coefficient of acetone in the conversion of acetone to acetaldehyde	<i>acetal</i>	refer to acetaldehyde species
$\nu_{CO_2,a}$	stoichiometric coefficient of CO ₂ in the conversion of acetone to acetaldehyde	<i>ads</i>	adsorbed
$\nu_{\bullet OH,j}$	stoichiometric coefficient of the $\bullet OH$ radical in reaction step <i>j</i>	<i>app</i>	apparent
$\nu_{H_2O,j}$	stoichiometric coefficient of H ₂ O in reaction step <i>j</i>	<i>av</i>	average
$\nu_{h,j}$	stoichiometric coefficient of component <i>h</i> in reaction step <i>j</i>	<i>irr</i>	irradiated
$\nu_{i,j}$	stoichiometric coefficient of component <i>i</i> in reaction step <i>j</i>	<i>max</i>	maximum
θ	tangential coordinate	<i>methanol</i>	refer to methanol species
λ	radiation wavelength, nm	<i>formaldehyde</i>	refer to formaldehyde species
λ_{max}	upper bound of wavelength in the range of interest, nm	<i>min</i>	minimum
λ_{min}	lower bound of wavelength in the range of interest, nm	<i>opt</i>	optimum
$\Delta H_{OH^{\bullet}}$	enthalpy to produce a mole of OH^{\bullet} from H ₂ O and O ₂ (J/mole)	<i>ref</i>	reflected
ΔH_T	enthalpy to produce OH^{\bullet} from H ₂ O and O ₂ (J/mole)	<i>trans</i>	transmitted

Chapter 1

1 Introduction

Volatile Organic Compounds (VOCs) are among the most common and harmful pollutants emitted by anthropogenic sources. VOCs are found in: a) outdoor environments, contributing with ground-level ozone and particle matter formation (Pun, Wu, & Seigneur, 2002) and b) indoor environments, affecting human health (Hulin, Simoni, Viegi, & Annesi-Maesano, 2012).

The sources of the emissions of VOCs are mainly from transportation, firewood burning, agriculture, paints, solvents, and the oil and gas industry. The increasing number of regulations with respect to VOC emissions and concentrations values has led to looking for new green technologies and more sustainable processes. The emission of VOCs is one of the main problems faced today regarding air quality. There are still great challenges to be solved in order to address this issue.

Several methods have been proposed for air cleaning such as biofiltration, membrane separation adsorption, oxidation, condensation, absorption, among others. However, heterogeneous photocatalysis is a most valuable method for the complete degradation of indoor contaminants, converting VOCs into CO₂ and H₂O at low temperatures. It can degrade most air contaminants such as aldehyde, aromatics, alkanes, olefins and others. However, the approaches to be used for photocatalyst immobilization in scaled and highly efficient photoreactors are still not well established. Furthermore, there is a lack of reported photonic efficiencies and a shortage of required methods to establish these efficiencies.

PCO (Photo-Catalytic Oxidation) requires a semiconductor and a radiation source providing photons with higher energy than the semiconductor band gap (Fujishima, Zhang, & Tryk, 2008). The photocatalysis reaction steps for the photodegradation of VOCs in air can be divided into: a) *Excitation*: This involves the absorption of photons on the semiconductor surface. This photon absorption leads to electron displacement from the valence band to the conduction band, leaving an electron (-) and a hole (+); b)

Adsorption: This encompasses the adsorption of water, oxygen and organic species; c) *Recombination*: This includes the reverse reaction where electrons and holes recombine with each other releasing heat. This step does not contribute to photoconversion, decreasing the overall efficiency of the PCO reaction (de Lasa, Serrano, & Salaices, 2005b); d) *Trapping and Radical Formation*: This accounts for the adsorbed species interacting with the charge carriers. In this series of redox reactions, the formation of oxygenated radicals (superoxides, hydroxyl radicals, hydrogen peroxide) occurs; e) *Oxidation*: This encompasses the attack of organic molecules via hydroxyl radicals. Successive oxidation steps eventually lead to mineralization with the formation of CO₂ and water. (Turchi & Ollis, 1990).

Studies in photocatalysis in air have mostly focused on semiconductor synthesis with higher photoactivity and lower band gaps for the photodegradation of pollutants in air. However, while larger scale photoreactors (10-100 liter volume range) have already been studied (Han et al., 2012; Lopez et al., 2013; Tompkins et al., 2005; Wang et al., 2012), both the immobilization of nanomaterials to large surfaces and the efficiency evaluation of the photoreactor/photocatalyst were not performed rigorously.

In this respect, both the support and immobilization of TiO₂ play an important role in the photocatalyst performance. A reliable technique for TiO₂ immobilization has to be established to provide the following:

- a) Strong adherence between the TiO₂ and the support.
- b) Unmodified TiO₂ crystal structure during preparation and immobilization.
- c) Uniform coating of different support surfaces and geometries.
- d) High degree of TiO₂ layer irradiation.

The immobilization method has a high effect on the photon absorption and therefore, on the photoactivity. The particle agglomeration, surface area and film thickness have a direct influence on the extent of photonic efficiency. Consequently, one has to establish both an efficient semiconductor immobilization and the extent of photon utilization.

Photon use can be demonstrated with suitable Quantum Yields (QY) (de Lasa, Serrano, & Salaices, 2005a). For instance, the frequently considered QY, based on photoconverted molecules to incident photons, does not provide a phenomenological based performance assessment (Bettoni et al., 2013; Kisch & Bahnemann, 2015; Serpone, 1997; Zhang & Anderson, 2013). A modified and more suitable QY can be considered using the ratio of the $\bullet OH$ radicals consumed over the photons absorbed (Garcia-Hernandez, Rosales, & de Lasa, 2010). The evaluation of absorbed photons is of high relevance for adequate reaction modeling and photoreactor design (Arancibia-Bulnes, Jiménez, & Estrada, 2009). This task which is at times challenging is seldom adopted by researchers, with a few exceptions (Ballari et al., 2015; Muñoz-Batista, Kubacka, Hungría, & Fernández-García, 2015). Furthermore, the joint use of the apparent Quantum Yield (based on incident photons) and the Quantum Yield (based on absorbed photons) can provide an adequate assessment of the photoreactor design and the photocatalyst activity (Muñoz-Batista et al., 2015).

Since the proposed QY is a parameter based on $\bullet OH$ radicals consumed and not entirely based on energy consumed, Serrano et al. (Serrano & de Lasa, 1997) proposed the Photochemical Thermodynamic Efficiency Factor (*PTEF*). The *PTEF* was thus, defined as the energy used by the hydroxyl radicals for organic molecule oxidation over the energy absorbed by the photocatalyst. The *PTEF* was later extended to photocatalytic systems in air (Garcia-Hernandez, Serrano, & de Lasa, 2012).

The establishment of a photoreaction kinetic model is also relevant for photoreactor scale-up. Langmuir-Hinshelwood (L-H) models are suitable for describing the photodegradation of organic pollutants in air (Garcia-Hernandez, Serrano, & de Lasa, 2010; Obee, 1996; Peral & Ollis, 1992). Photodegradation models are required in order to establish Langmuir-Hinshelwood equations for all observable species. There have been significant contributions regarding the development of kinetic models in photocatalysis. In this respect, Salaices, Serrano, and de Lasa (2004) proposed the parallel-series reaction model. The parallel-series mechanism can be linked to the distribution of sites with varying degrees of oxidation strengths (different local concentrations of $\bullet OH$ groups). This leads to a diversity of steps, each of them contributing to oxidation to a different

extent. The estimation of kinetic parameters based on the series-parallel model for photodegradation of VOCs in air is not well studied. Moreover, the adsorption constant is usually not estimated independently, leading to uncertainty due to high cross-correlation.

To summarize this matter, we believe that the adequate analysis of a photoreactor requires the evaluation of a) photocatalyst immobilization, b) irradiation and photonic efficiencies and c) kinetic analysis using a Langmuir Hinshelwood based model.

To address these issues, the present study reports a detailed analysis of a TiO₂ coated mesh in a 55.1 L scaled-up Photo-CREC-Air Reactor for the photodegradation of acetone and acetaldehyde. Two immobilization techniques are considered: Spread Coating (SCM) and Air Assisted Spray (AAS) in conjunction with an Automatized Spinning Coating (TiO₂-AAS-ASC). Homogeneity, reliability and particle agglomeration are evaluated for both procedures. The effect of the immobilization method and photocatalyst film thickness on the photon absorption and photocatalytic activity is studied. Quantum Yields and PTEFs are evaluated using a comprehensive methodology based on absorbed photons and hydroxyl radical consumed. It is demonstrated that *QYs* in the Photo-CREC-Air Unit can reach values close to the theoretical expected maximum of 133% and achieve a *PTEF* of 24% photon energy utilization. It is also shown that apparent Quantum Yields (*QY_{app}*) depend on the combined effect of *QYs*, for the photocatalyst and the photon absorption in the photoreactors.

Additionally, a kinetic analysis is performed for the photodegradation of acetone and acetaldehyde using a broad initial model pollutant concentration in the 25-320 µmole/L range. A series-parallel based Langmuir-Hinshelwood model is used to describe the photodegradation of acetone and acetaldehyde. Adsorption constants are calculated independently and estimated with a 0.97-0.98 range correlation coefficient.

The results obtained in this PhD Dissertation provide evaluation strategies in the following matters: a) homogeneity and reliability of the photocatalyst immobilization method; b) irradiation field and photon-photocatalyst interaction; c) photonic efficiency calculation through Quantum Yields and Photochemical Thermodynamic Efficiency Factor; d) kinetic analysis with series-parallel network models. Results obtained also

demonstrate the special value of experimentally established macroscopic balances. Macroscopic balances allow decoupling photocatalyst efficiency and photoreactor efficiency. This approach is critical to clarify key engineering issues for the scale-up of photocatalytic reactors. It is our view that challenges in the application of photocatalysis for air treatment can only be addressed using comprehensive methodologies as the ones reported here. Adopting these methodologies will lead to the engineering of superior performing photoreactors for the conversion of organic air pollutants.

Chapter 2

2 Literature Review

2.1 VOC Emissions

“Volatile Organic Compounds” (VOCs) are organic chemicals that have high vapour pressure at room temperature. VOCs are emitted from biological (Guenther, 1997) or anthropogenic sources (Goldstein & Galbally, 2007). The anthropogenic release of VOCs is detrimental to both the environment and humans, contributing with ground-level ozone and particle formation (Pun et al., 2002). It affects human health in the short and long term (Hulin et al., 2012). Most of the emitted VOCs are part of organic groups such as: alkanes, branched cycloalkanes, halogenated compounds, alcohols, aldehydes, ketones, esters, aromatic carbons and terpenes (Brown, Sim, Abramson, & Gray, 1994).

VOCs are released through the production and use of organic based goods. Fig. 1 reports a diagram showing VOC discharges at all levels from initial raw material processing to use of the manufactured product. In indoor environments, the presence of VOCs influences the health and safety of:

- ✓ Industrial workplaces: Indoor VOCs come from one or more stages of the industrial production process (Wiederkehr, 1994).
- ✓ Houses and buildings: Indoor VOCs are caused mainly by emissions during the use of the product. Products with high VOC emissions are: cleaning products, paints, furniture and building materials (U.S. Environmental Protection Agency, 1989).

People spend approximately 70 to 90% of their life inside (Aguado, Polo, Bernal, Coronas, & Santamaría, 2004; Finlayson-Pitts & Pitts Jr, 2000). As a result, exposure to VOCs has been described as being one of most significant risk factors for some respiratory and heart diseases (Hulin et al., 2012; WHO, 1999). VOCs are found to be in high concentrations in enclosed spaces (1000 times more concentrated than outdoor air) (Wallace, 1987).

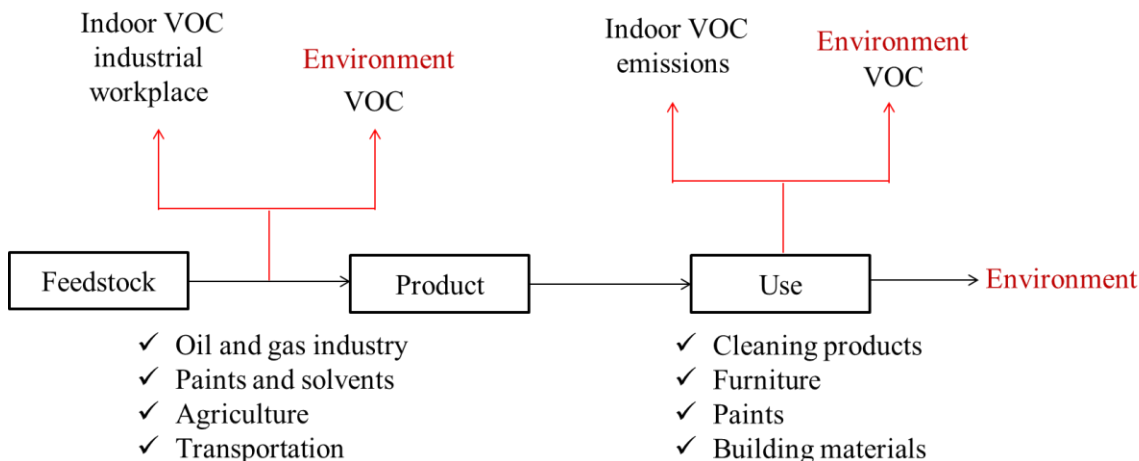


Figure 1: Schematization of the VOC Emissions from the Product Manufacturing to Its Final Use and Disposal.

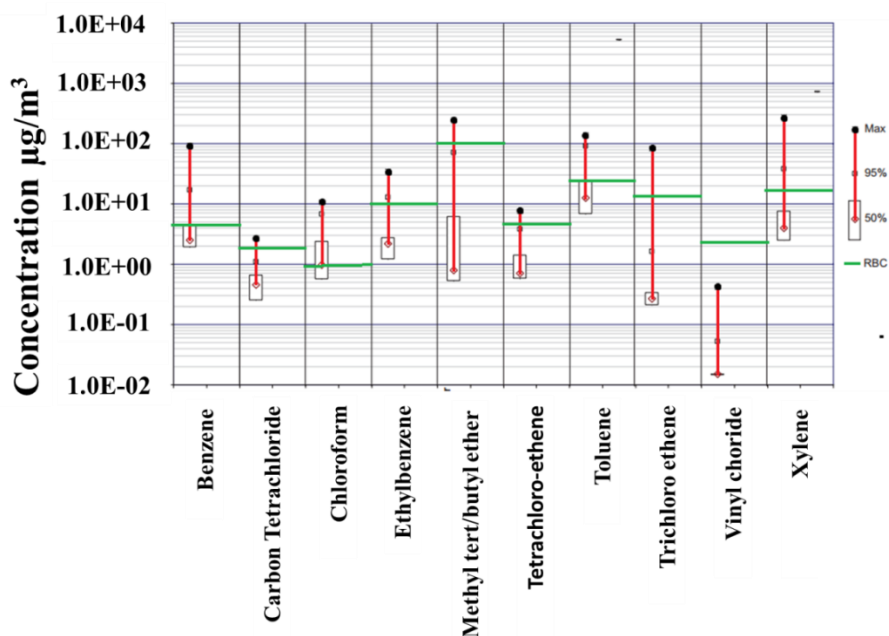


Figure 2: VOC Indoor Concentrations in North America Residences since 1990. Red lines are the range of measured concentrations and green lines are the average risk-based concentrations (RBC). Adapted from Dawson and McAlary (2009).

Fig. 2 reports the total concentration of VOCs measured in North American residences exceeding the concentration levels of exposure considered of risk (Dawson & McAlary, 2009).

In industrial workplaces, the indoor VOC concentrations depend of the production process and the generated products. The concentrations of VOCs in paints (Smith & Brown, 1993), oils (Mo et al., 2015), textiles (Estevan, Sogorb, & Vilanova), and electronic products (Shareefdeen, Taqvi, & Elkamel) among others range in the 30 to 4000 $\mu\text{g}/\text{m}^3$ levels.

Regarding the emissions of VOCs to the atmosphere, VOC sources are mainly from transportation, firewood burning, agriculture, paints, solvents, and oil and gas industries. The VOC emissions from off-road vehicles for example, decreased steadily from 2157 kt from 1990 to 2014 (Environment and Climate Change Canada, 2016).

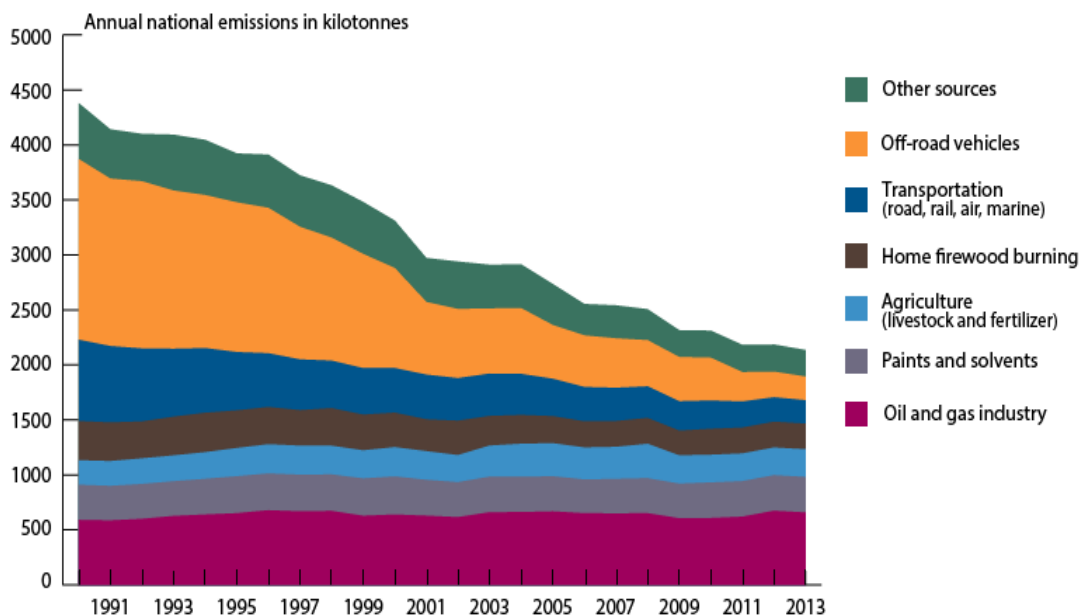


Figure 3: VOC Emissions by Source in Canada from 1990 to 2014 (Environment and Climate Change Canada, 2016).

The VOC decrease in transportation and in agriculture has mainly been the result of a better management of emissions. On the other hand, the VOCs from paints, solvents, and oil and gas industries have remained close to constant since 1990 (refer to Fig. 3). Some

of these VOC sources can be traced to leaks from equipment and piping, storage tanks, heat exchangers, and vessel venting and wastewater streams evaporation.

The Government of Canada initiated many actions in order to address the concern of VOC emissions such as the Automotive Refinishing Products Regulations ([Environment and Climate Change Canada, 2008b](#)), the VOC Concentration Limits for Architectural Coatings Regulations ([Environment and Climate Change Canada, 2008a](#)), the VOC Emission for Certain Products Regulations ([Environment and Climate Change Canada, 2008c](#)), among others. In addition, some authors have reported assessments on VOC emissions and possible technologies to mitigate these emissions. ([Estevan et al. 2016](#); [Mo et al., 2015](#); [Shareefdeen et al., 2016](#); [Smith & Brown, 1993](#); [Wiederkehr, 1994](#)). The Environmental Protection Agency established that a maximum 3-hour concentration of hydrocarbon content of $1.6 \times 10^{24} \text{ kg/m}^3$ (0.24 ppm) should not be exceeded in a year. In addition, the Environmental Protection Agency Standard 40 CFR Part 63 has established an air emission limit of 10 g of Total Organic Carbon per m^3 ([U.S. Environmental Protection Agency, 2008](#))

The increase of awareness of how anthropogenic activities affect human health and environments has drastically motivated us to look for new green technologies and more sustainable processes. The emissions of VOCs are one of the main problems faced regarding air quality. There are still great challenges in order to address this issue.

2.2 Techniques and Challenges of Technology for VOC Air Pollution

Several methods have been proposed for air cleaning such as biofiltration, membrane separation adsorption, oxidation, condensation, absorption, among others. Table 1 reports the characteristics, advantages and disadvantages for VOC removal techniques. Filtration, adsorption, absorption, and membrane separation processes are efficient for the elimination of air pollutants. Thus, the overall process can be considered a transfer of pollutants from one phase (e.g. air) to another phase (e.g. activated carbon). The main disadvantage still lies in having another phase with a high species concentration, without really having converted the pollutants. In this regards, biofiltration does not produce any

hazardous secondary waste and is 100% environmental friendly. However, the process is slow and does not eliminate all types of organic pollutants.

Regarding chemical methods, ozone oxidation is capable of degrading large amounts of pollutants. However, ozone may be, in itself harmful. Catalytic and thermal oxidation require high temperatures and therefore, high amounts of energy.

Table 1. Characteristics of Techniques for VOC Removal. Adapted from *Khan and Ghoshal (2000)*.

Technique	Materials	Secondary Waste	Removal Efficiency	Advantages	Disadvantages	Reference
Biofiltration	Microorganisms	Biomass	60-95%	Environmental friendly	Slow and selective	(Iranpour, Cox, Deshusses, & Schroeder, 2005)
Membrane Separation	Ceramics and Polymers	Exhausted Membranes	90-99%	High removal efficiency	High pressure drop, hazardous second waste	(Huang, Xu, Shi, & Lin, 1997; H. J. Kim, Nah, & Min, 2002)
Adsorption	Activated Carbon and Zeolites	Collected Organic on Adsorbent	80-96%	Easy to implement	Hazardous second waste	(Zhao, Ma, & Lu, 1998)
Oxidation	Ozone, Thermic, Catalytic and Photocatalytic Systems	Combustion Products	90-99%	High removal efficiency, not second waste	Thermal- high energy, ozone-hazardous, photocatalytic-sensitive to reactor config.	(Gervasini, Vezzoli, & Ragaini, 1996; Spivey, 1987)
Condensation	Cooling System	Condensate	70-85%	Easy to implement	High energy, low efficiency, selective	(Dwivedi, Gaur, Sharma, & Verma, 2004)
Absorption	Solvents	Solvent with Collected Organics	90-98%	Well known	Rigorous maintenance, selective and second Waste	(Lin, Liu, & Tan, 2003)

Heterogeneous photocatalysis is a most valuable method for the complete degradation of indoor contaminants, converting VOCs into CO₂ and H₂O. It can degrade most air contaminants such as aldehyde, aromatics, alkanes, olefins and others. Heterogeneous photocatalysis thus, offers a great alternative for the total degradation of the pollutants, (Zhao & Yang, 2003). Heterogeneous photocatalysis efficiency (photocatalyst utilization, radiation efficiency and removal efficiency) is highly affected by the reactor

configuration. Therefore, further research is required in this area in order to make the photocatalytic oxidation feasible for scale-up.

2.3 Photocatalytic Oxidation in the Photodegradation of VOCs

A photocatalytic oxidation reaction takes place once a photon hits a semiconductor surface.



As a result, there is an electron-hole pair which interacts with the reactant molecules (the electron hole h^{+} for oxidation and the e^{-} electron for reduction). This pair yields, super oxide anions and hydrogen peroxide with oxygen and water vapour. Electrons and holes can recombine releasing energy. In this recombination process, excited electrons return to the valence band and do not react with the adsorbed species (de Lasa et al., 2005b). Thus, if one would like to improve the efficiency of the photocatalytic process, one should develop strategies to reduce/eliminate recombination.

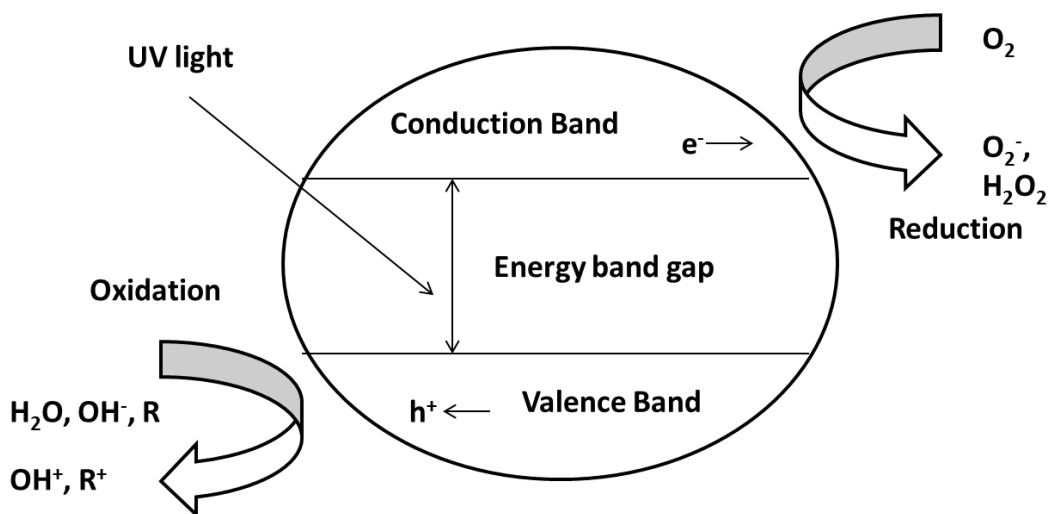
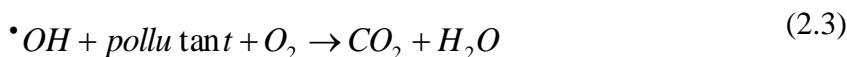


Figure 4: Schematic Illustration of the Electron-Hole Generation in a Photocatalyst Particle.

A linear combination of the mechanism presented in Appendix A leads to the following stoichiometry:



One can see that in this VOC oxidation process, the $\cdot OH$ radicals are the primary oxidants. As a result, the final products of the photooxidation are CO_2 and H_2O .



One should note that photocatalysis does not take place in one single step. Intermediates can be formed in the oxidation of VOCs. The photoconversion of recalcitrant intermediates may reduce the efficiency of the overall process by occupying the active sites of the photocatalyst (Mo, Zhang, Xu, Lamson, & Zhao, 2009).

Moreover, it is important to appreciate that the photooxidation in air is dependent on several factors such as the nature of the photocatalyst, the reactor design and the light source, as well as the air humidity, among others (de Lasa et al., 2005b).

Metal oxides and sulphides are widely used as photocatalysts because of their corrosion resistance and band gap energies. The ones that demonstrate better higher activity are TiO_2 , ZnO , ZrO_2 , SnO_2 , WO_3 , CeO_2 , Fe_2O_3 , Al_2O_3 , ZnS and CdS . The selection of the photocatalyst for a specific process depends, however, not only of the pollutants to be photoconverted but also on the final use of the medium to be decontaminated (e.g. water and air) (Pelaez et al., 2012).

TiO_2 presents several advantages compared with other catalysts such as its low cost, its ability to work at ambient temperature with high photocatalytic activity, and stability. In this case, no other chemical additives outside the photocatalyst itself are strictly required (Hager, Bauer, & Kudielka, 2000).

There are three polymorphs of TiO_2 : anatase, rutile and brookite (Nolan, Seery, & Pillai, 2009). They have energy band gaps of 3.02, 3.23 eV and 3.2, respectively. When the metastable anatase and brookite are calcined at temperatures higher than 600°C , both forms are converted to the most thermodynamically stable TiO_2 : rutile. Figure 5 shows that the central titanium atoms are coordinated with six atoms of oxygen in an octahedral configuration. Regarding anatase and rutile, both have a tetragonal structure while brookite has orthorhombic structure (Hu, Tsai, & Huang, 2003).

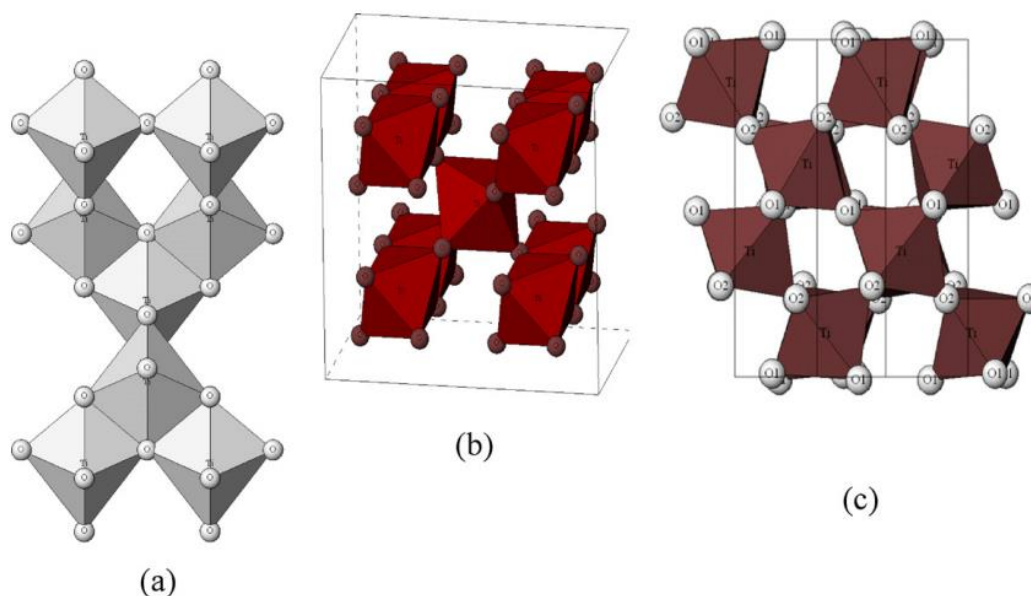


Figure 5: Molecular Structure of (a) Anatase, (b) Rutile and (c) Brookite (Pelaez et al., 2012).

Regarding anatase, it has a number of advantages in photocatalytic oxidation with respect to rutile. The anatase band location gap is smaller than that of rutile. Thus, this creates more favorable reactions where electrons are donated and stable surface peroxides are formed. Degussa P25, more recently designated as Aeroxide, is the commercially available form of TiO_2 . It has a 30 nm average particle diameter, a $50 \text{ m}^2/\text{g}$ of surface area, and a 70wt% anatase/30wt% rutile. Pelaez et al. (2012) reported that the 70wt% anatase/30wt% rutile crystal ratio has higher photocatalytic activity than other TiO_2 blends.

2.4 Reactor Design for Photocatalytic Air Treatment

The design of the photoreactor is one of the most important aspects of a photooxidation process. In the case of air remediation and degradation of VOCs in indoor environments, it is important to design a reactor capable of managing high feed rates with high photoconversion rates, low pressure drop and high energy efficiencies.

In order to obtain high photoconversion rates, it is necessary to guarantee the adequate interaction between the air, the light and the photocatalyst (Dibble & Raupp, 1992). The UV source, the photoreactor configuration, the lamp location, the photocatalyst, the distribution of the radiation, the impregnation of the photocatalyst, and the interaction between the photocatalyst and the air are all factors to be considered (de Lasa et al., 2005b). Examples of some of these reactors are as follows: a) the powder layer unit (Peral & Ollis, 1992), b) the plate reactor (Obee, 1996), c) the honeycomb (Hossain, Raupp, Hay, & Obee, 1999), d) the annular reactor (Jacoby, Blake, Noble, & Koval, 1995), e) the packed bed unit (Mehrvar, Anderson, & Moo-Young, 2002), f) the fluidized bed (Chang, Chen, & Lu, 2003), g) the optical fiber (Choi, Ko, Park, & Chung, 2001) and h) the mop fan unit (Riffat & Zhao, 2007). Table 2 reports the advantages and disadvantages of each photoreactor configuration.

Table 2. Advantages and Disadvantages of Photoreactors for VOC Removal.

Reactor	Advantages	Disadvantages
Plate Reactors	High degree of irradiation	Low interaction of photocatalyst with gas, low surface area
Honeycomb Reactors	High surface area and low pressure drop	Small fraction of photocatalyst irradiation
Fluidized Bed/Packed Bed Reactors	High flow rates, high interaction of air with photocatalyst, low pressure drop	Small fraction of photocatalyst irradiation
Annular Reactors	High flow rates, high degree of irradiation	Challenges with interaction of photocatalyst and gas

The honeycomb photoreactor displays a high surface area and a low pressure drop for high gas flow rates. It contains several channels (generally of the order of 1 mm) covered with thin layers of catalyst (Hayes, Kolaczkowski, & Thomas, 1992). Unfortunately, only a small fraction of the honeycomb is currently irradiated and as a result, only modest photocatalytic activity is expected.

Fluidized bed reactors also permit managing high flow rates keeping good interaction between the photocatalyst and the gas flow. The pressure drop in this configuration is also low (Zhao & Yang, 2003). However, there is a significant difficulty in having large fractions of irradiated photons contacting the entire mass of photocatalyst available. Finally, the annular reactor involves two concentric cylinders. The lamps can be located in the central wall of the photoreactor. Regarding the photocatalyst, it can be placed in central well and/or on the surface of the outer cylinder. While this proposed arrangement is promising, it still requires refinements in the ways that the irradiation photocatalyst and air are contacted. This is attempted in Photo-CREC Air Unit.

One has to acknowledge that photoreactor scale-up is still a challenge for photoreactor design and implementation. In the units mentioned above, it is required that a higher volume of air be treated together with larger electrical power or sun energy. This may open opportunities for special geometries and unit configurations. In spite of these challenges, it is expected that the application of reaction engineering principles demonstrated at the laboratory scale will successfully assist in the scaling-up of photocatalytic reactors for air treatment.

2.5 Irradiation Source for Photocatalytic Air Treatment

The irradiation source in photocatalytic processes has a drastic effect on the photocatalytic oxidation reaction. Thus, the performance of the photoreaction depends dramatically on the energy per unit area provided. During the photocatalytic process, the semiconductor sites are excited with photon energies higher than the photocatalyst band gap energy. For example, the photooxidation reaction using anatase occurs in the presence of photons with a wavelength equal or less than 385 nm. Thus, photons with a wavelength of near ultraviolet radiation (UV) are required. The wavelength range of UV

is 10-400 nm and is divided into UVA, UVB and UVC where the wavelength ranges are 315-400, 280-315 and 200-280 nm, respectively. The radiation between 10 and 200 nm is absorbed by air, therefore, it is called Vacuum UV (Mo et al., 2009). Generally, artificial UV sources are made with mercury. Mercury lamps can be classified into three types: the low pressure mercury lamp, medium pressure mercury lamps and advanced medium pressure mercury lamp (Bolton, Safarzadeh-Amiri, & Cater, 1995). Table 3 shows the principal properties of the mercury lamps.

Table 3. Artificial UV Mercury Lamp Properties. Adapted from Bolton et al. (1995)

	<i>Low Pressure Mercury Lamp</i>	<i>Medium Pressure Mercury Lamp</i>	<i>Advanced Medium Pressure Mercury Lamp</i>
Time (h)	>5000	>2000	>3000
Output range	80% in a narrow range (254 nm)	Broad (below 250 nm)	Strong (below 250 nm)
Energy Density	Low (~1 W/cm)	Moderate (~125 W/cm)	High (~250 W/cm)
Electrical to photon energy	High (~30%)	Moderate (~15% for 200-300 nm)	High (~30% for 200-300 nm)

2.6 Photo-CREC-Air Reactors

Since 1999, Photo-CREC Air Reactors have been designed for air cleaning processes (Ibrahim & de Lasa, 1999). Photo-CREC Air Reactors advantages are: minimum pressure drop, good contact between the photocatalyst, the air stream to be treated and the UV radiation. The photocatalyst is firmly immobilized on a mesh support.

There have been additional modifications to improve the photocatalytic performance of the reactor such as increasing the efficiency of the UV energy provided (Ibrahim, 2001). These proposed modifications were achieved and tested by (Ibrahim & de Lasa, 2002). The modified Photo-CREC Air Reactor was operated in a closed-loop system, with Zn-

plated pipes. The radiation sources were 8-Pen-Ray 1-watt lamps located in the outer section, with a power output of $1213 \mu\text{Wcm}^{-1}$ at 20 mA (AC) and a principal radiation wavelength of 365 nm. Parabolic reflectors were placed in the reaction section to improve the photon incidence efficiency. The air was pumped by a blower and introduced into a Venturi stainless steel section. The reaction section, located immediately following the Venturi throat, consisted of a TiO_2 impregnated fiberglass mesh through which the air passed. In this section, the four trapezoidal windows were made from acrylic.

Figure 6 reports a schematic diagram of the Photo-CREC Air Reactor. While experimenting with this unit, an amount of acetone, acetaldehyde or isopropanol were used as model pollutants and injected into the reactor. Concentrations of hydrocarbon species and CO_2 were monitored at strategically selected times. Efficiencies of apparent Quantum Yields larger than 100% were observed in this configuration for acetaldehyde and isopropanol photodegradation (Ibrahim & de Lasa, 2003).

These experimental results showed that photoconversion rates depend on: a) the nature of the photocatalyst, b) the agglomeration of semiconductor particles, c) the interaction between particle and mesh, d) the catalyst loading, e) the type of pollutant, f) the radiation intensity and g) the temperature.

However, a series of improvements to be implemented in the Photo-CREC Air Reactor was proposed as follows: a) Creating an online automatic sampling system in order to reduce inaccuracies in the data measurements, b) Changing the material of the windows to a higher temperature resistant material, and c) Analyzing the influence of the photocatalyst type and of the operational parameters in the quantum efficiencies. Studies in the Photo-CREC Air Reactor realized by Romero-Vargas Castrillón and de Lasa (2007) through Computational Fluid Dynamics showed that improvements could be made by changing the geometry of the reactor. A single cylindrical window instead of the four trapezoidal windows, and a perforated plate instead of wire mesh basket sidewalls were proposed. Figure 6 and Figure 7 show a scheme of the simulated reactor.

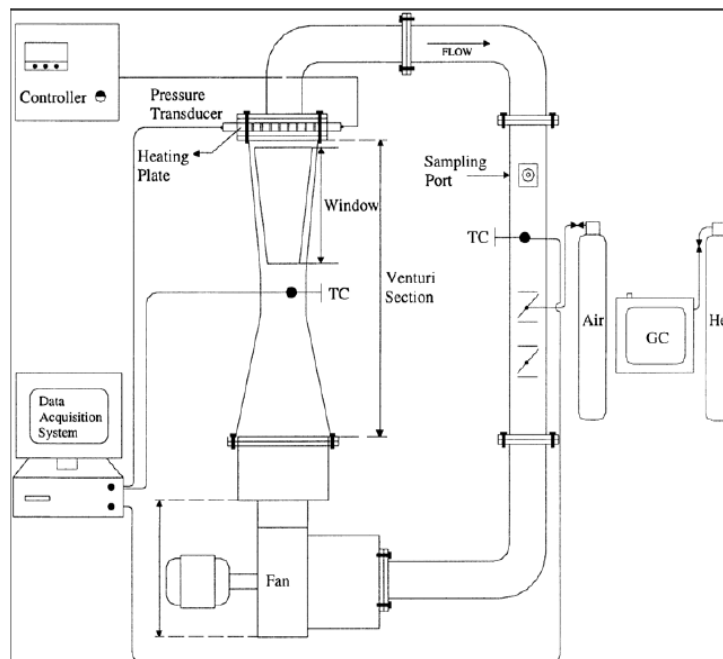


Figure 6: Schematic Diagram of the 14.7 Liter Photo-CREC Air Reactor (H. Ibrahim & de Lasa, 2004).

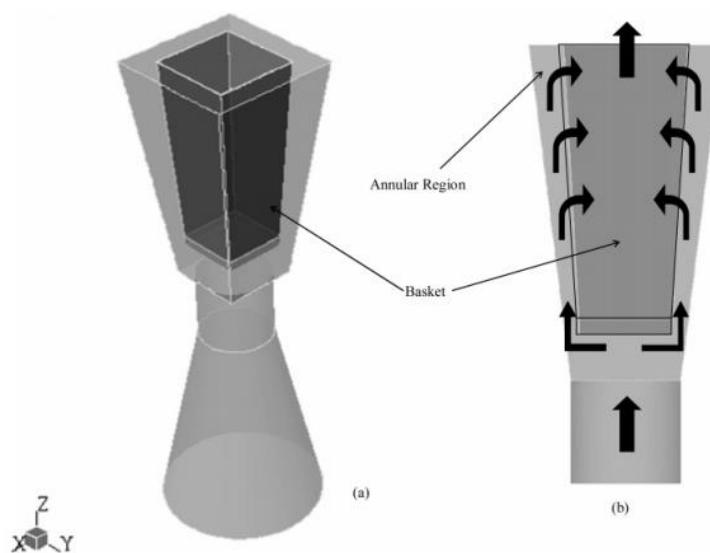


Figure 7: Schematic Diagram of the 14.7 Liter Photo-CREC Air Reactor (Romero-Vargas Castrillón & de Lasa, 2007).

The modifications proposed for the 14.7 L Photo-CREC Air Reactor, were evaluated in the work of [Garcia-Hernandez \(2012\)](#). The new design is, in fact, a scaled up version of the previous type, incorporating the modifications as proposed by [Romero-Vargas Castrillón and de Lasa \(2007\)](#). The new 55.1 liter Photo-CREC Air Reactor provides better contact between the air stream and the impregnated TiO₂ mesh, as well as better mesh irradiation. In addition, the modified Photo-CREC Unit allows measurements of scattered, absorbed and reflected radiation and as result, macroscopic radiation balances.

The entire Photo-CREC Air Unit can be viewed as a closed-loop system. Air is recirculated through the reactor with the help of an air blower. Air is pumped into a stainless steel Venturi section, and subsequently driven into the reaction section. The reaction section includes 8 UV lamps surrounding a glass cylindrical reactor. The TiO₂ impregnated mesh is situated inside the glass, supported by a bullet nose bottom. This configuration allows the air to flow from the annular region to the interior of the mesh. This design provides excellent interaction between the air, the photocatalyst and the UV irradiation ([Garcia-Hernandez et al., 2012](#)).

The design described above, was used to photodegrade isopropanol, acetone and acetaldehyde. Kinetic modeling, Quantum Yields (QYs) and Photochemical Thermodynamic Efficiency Factors (PTEF) were calculated using experimental results.

While all these research contributions regarding photoreactor configurations were significant, there are still issues requiring improvement such as a) the development of a technique that provides a more homogeneous TiO₂ coating, b) the optimization of the use of a photocatalyst and its characterization, c) the evaluation of macroscopic balances including the scattered radiation produced by the semiconductor and a radiation absorbance efficiency assessment, d) the employment and strategic value of the series-parallel reaction network used to describe the photoconversion of various model pollutants, d) the establishment of upper limits for quantum efficiencies and e) a comprehensive calculation of the enthalpy of $\bullet OH$ formation for PTEF estimations.

2.7 Immobilization Methods

A significant body of technical literature has already been focused on the synthesis of semiconductors with higher photoactivity and lower band gaps for the photodegradation of pollutants in air. The application of these nanomaterials in relevant process scales requires the TiO₂ deposition on a substrate. The coated material should also have the adequate photoactivity, homogeneity and stability.

In this respect, both the support and immobilization of TiO₂ play an important role in the photocatalyst performance. A reliable technique for TiO₂ immobilization has to be established to provide the following:

- e) Strong adherence between the TiO₂ and the support.
- f) Unmodified TiO₂ crystal structure during preparation and immobilization.
- g) Uniform coating of different support surfaces and geometries.
- h) High degree of TiO₂ layer irradiation.

A number of methods for TiO₂ coatings on different support materials for the photodegradation of pollutants are reported in the literature (Shan, Ghazi, & Rashid, 2010). These include physical and chemical vapor deposition, anodic oxidation, atomic layer coating, magnetron sputtering, pulsed laser coating, electro deposition, dip coating (Bestetti et al., 2010; Giolli et al., 2007; Kim, Kang, & Kim, 2010; Krämer, Kunz, Gräf, & Müller, 2015; Lee et al., 2013; Maleki-Ghaleh et al., 2016; Traid, Vera, Ares, & Litter, 2015; Verbruggen et al., 2014; Z. Zhao, Sun, Zhang, & Bai, 2015). Dip coating is in fact, one of the most popular methods. It does not require hazardous chemicals or high energy consumption.

However, dip coating appears to present issues with large surfaces and geometries. For instance, in the case of TiO₂ deposited on a mesh, the impregnating solution may block the mesh openings. Pressurized air may be required then, to eliminate the excess of

solution (Bestetti et al., 2010). This additional step can affect the homogeneity of the TiO₂ deposited.

Spread coating is also a popular technique due to its low cost and simplicity. It can be applied without damaging the catalyst structure (Lopez et al., 2013; Šuligoj et al., 2016). Spread coating was implemented in the past by our group for the TiO₂ immobilization with the aim of degrading VOCs. This consists of brush spreading sonicated TiO₂ slurry on a mesh followed by drying or calcination. Degussa P25 coated on a mesh using this method showed high photocatalytic degradation of toluene (Ibrahim & de Lasa, 1999), acetone (Garcia-Hernandez et al., 2012; Ibrahim & de Lasa, 2002), isopropanol (Garcia-Hernandez, 2012) and acetaldehyde (Ibrahim & de Lasa, 2003). Despite the advantages of this technique, the search for an improved method is needed. This is required to provide a better control of the titanium dioxide homogeneity, loading, stability under flow and a better degree of semiconductor utilization.

The spray technology is a well-known technique. It includes all the advantages of dip and spread spray coating. It has been widely used in nanoparticle synthesis (Iskandar, Gradon, & Okuyama, 2003; Li, Anton, Arpagaus, Belleteix, & Vandamme, 2010; Okuyama & Wuled Lenggoro, 2003). Spray coating in particular, is very convenient for all types of geometries (including metallic meshes). It is easy to scale-up. It can be applied in combination with sol-gel (Chen, Kelder, & Schoonman, 1999; Fujihara, Kumar, Jose, Ramakrishna, & Uchida, 2007; Li, Liu, Cheng, & Tong, 2003; Momeni, Golestani-Fard, Saghafian, Barati, & Khanahmadi, 2015), pyrolysis (Conde-Gallardo et al., 2005), electrostatic technique (Chen et al., 1999) or spray drying (Byrne, Eggins, Brown, McKinney, & Rouse, 1998; Han et al., 2012; Jung, Hwang, Park, & Choi, 2013). Spray coating should in principle lead to a high dispersion of TiO₂ particles with high photoactivity (Han et al., 2012). However, and in spite of this progress in coated mesh characterizations, further progress is required in the design of scaled up photocatalytic reactor units. In this work, we developed a TiO₂ Air Assisted Spray with Automatized Spinning Coating method. It is proven that this approach leads to a uniform and stable coating with little particle agglomeration and high efficiencies.

2.8 Energy Efficiencies in Photocatalytic Reactors

Energy consumption is an important parameter in photocatalysis. Energy consumption and energy utilization (energy efficiency) determine operational costs. Hence, energy efficiency in a photocatalytic reactor is a relevant parameter to be considered.

The best possible efficiency in a photocatalytic process should involve the optimum absorption of photons with minimum hole-electron charges recombination (Choi, Termin, & Hoffmann, 1994; Ong & Ho, 2016; Paz, 2010; Sakthivel et al., 2004). However, the methodology for the adequate calculation of the best efficiency is still under intense debate. Most studies still report photocatalytic efficiency in terms of organic species conversion rates. These rates can be affected by a number of factors, such as the radiation source, the reactor configuration and operating conditions (Adán, Marugán, Sánchez, Pablos, & van Grieken, 2016; Marugán et al., 2013). Therefore, this approach is considered not accurate enough to describe the photocatalytic efficiency of a reactor or a photocatalyst (Kisch & Bahnemann, 2015).

With this in mind, energy efficiency has to be established using relevant indicators such as QYs. The Quantum Yield (QY) is a well-known parameter used to describe photon utilization based on the target molecule conversion. It was initially proposed for homogeneous systems considering photoconverted molecules over absorbed photons (Serpone, 1997). The application of this definition for heterogeneous systems can be challenging since one has to base the QY s on the absorbed photons (Arancibia-Bulnes et al., 2009). With this aim in mind, authors have calculated QY s accounting for photon absorption in air treatment photoreactors using: a) numerical solutions of the radiative transfer equation and b) experimental measurements of various radiative fluxes (Ballari et al., 2015; Garcia-Hernandez et al., 2012; Muñoz-Batista et al., 2015; Palmisano, Loddo, et al., 2015; Zazueta, Destailats, & Li Puma, 2013).

While the QY can provide a first basis for photocatalytic efficiency, it has to include stoichiometric considerations (Muñoz-Batista et al., 2015). On this basis, de Lasa et al. (de Lasa et al., 2005a), proposed a QY involving hydroxyl radicals consumed over absorbed photons. This QY accounts for the stoichiometric requirements of organic

molecules to be converted at every stage of the photocatalytic reaction network. Table 4 reports a summary of the definitions of QY existing in the literature.

Table 4. Summary of Quantum Parameters Reported in the Literature. Adapted from Ibrahim (2001).

Definition	Reference
<p>Primary Quantum Yield (Primary QY) number of pollutant molecules degraded from a primary process number of photons absorbed</p>	<i>Cassano et.al. (1995)</i>
<p>Overall Quantum Yield (Overall QY) number of pollutant molecules degraded from primary and secondary processes number of photons absorbed</p>	<i>Cassano et.al. (1995)</i>
<p>Quantum Yield (Apparent QY) number of pollutant molecules degraded number of photons absorbed</p>	<i>Valladares and Bolton (1993)</i>
<p>Apparent Quantum Yield or Global Quantum Yield (QE) number of pollutant molecules degraded from a primary process number of photons entering the reactor</p>	<i>Fox and Dulay (1993)</i>
<p>Minimum Apparent Quantum Yield (QY app, min) $\frac{\text{number of pollutant molecules degraded}}{\text{number of photons reaching the photocatalyst with } \lambda < 388 \text{ nm}}$</p>	<i>Garcia-Hernandez et.al. (2010)</i>
<p>Minimum Apparent Quantum Yield (QYapp, min) $\frac{\text{number of } ^\bullet\text{OH consumed}}{\text{number of photons reaching the photocatalyst with } \lambda < 388 \text{ nm}}$</p>	<i>Garcia-Hernandez et.al. (2012)</i>

Furthermore, the joint use of the Apparent Quantum Yield (based on incident photons) and the Quantum Yield (based on absorbed photons) can provide an adequate assessment of the photoreactor design and photocatalyst activity (Muñoz-Batista et al., 2015).

In this respect, it is important to express the apparent Quantum Yield as a product of two variables as follows: 1) An absorption factor (photoreactor configuration dependent parameter) and b) A Quantum Yield (photocatalyst dependent parameter). One can, on

this basis conclude, that performing radiation measurements and macroscopic radiation balances is essential for adequate photon efficiency calculations (Salvadores, Minen, Carballada, Alfano, & Ballari).

In order to accurately evaluate energy efficiency in a photocatalytic reactor, one has to develop thermodynamic energy balances. To address this, Serrano et al. (Serrano & de Lasa, 1997) proposed the Photochemical Thermodynamic Efficiency Factor (*PTEF*) for the degradation of organic pollutants in water. The *PTEF* was thus, defined as the energy used by the hydroxyl radicals for organic molecule oxidation over the energy absorbed by the photocatalyst. The *PTEF* was later extended to photocatalytic systems in air by Garcia-Hernandez et al. (Garcia-Hernandez et al., 2012).

In spite of all this progress, there are still issues to be clarified: Will the photocatalyst formulation, the photoreactor design or both require to be improved? The challenges in the application of photocatalysis for air treatment can only be addressed using comprehensive methodologies such as a rigorous photonic efficiency evaluation. Adopting these methodologies will lead to the engineering of superior performing photoreactors for the conversion of organic air pollutants.

2.9 Photoreaction Kinetics and Kinetic Models

2.9.1 Langmuir-Hinshelwood Model

Photoreaction rates, adsorption constants, and reaction kinetic constants are key kinetic parameters to be established in order to evaluate the photocatalytic performance. One should notice that photocatalytic rates are influenced by: a) temperature, b) humidity, c) wavelength, d) radiation intensity, e) oxygen concentration, f) contaminant concentration, g) superficial gas velocity, h) residence time and i) photocatalyst loading. Changes in these parameters can be used to improve the photocatalytic rates, photocatalytic efficiency and as a result, affect the scale-up of the process (Mo et al., 2009).

Regarding reaction rate models, it has been established that pollutants are adsorbed at equilibrium on semiconductor surfaces. Thus, Langmuir-Hinshelwood (L-H) models are expected to apply as observed for different pollutants photoconversion in air (Garcia

[Hernandez et al., 2010](#); [Obee, 1996](#); [Peral & Ollis, 1992](#)). As a result, the Langmuir-Hinshelwood (L-H) model is recommended in order to establish the effect of concentrations of various model pollutants on the photocatalytic rate.

The photocatalytic oxidation reaction is a typical bimolecular reaction between surface oxygen and the reducible reactants ([Serpone & Pelizzetti, 1989](#)). There have been significant contributions regarding the development of kinetic models in photocatalysis. In this respect, ([Salaices et al., 2004](#)) proposed the parallel-series reaction model. This model was used to describe the photodegradation of phenol in liquid media. This model is based on calculating the observable chemical species in the water phase. The parallel-series mechanism can be linked to the distribution of semiconductor sites with varying oxidation strengths (different local concentrations of $\cdot OH$ groups). This leads to a diversity of steps, each of them contributing to oxidation to a different extent (e.g. one oxidation step involves a single $\cdot OH$ group or complete mineralization includes all the $\cdot OH$ required for CO_2 formation). This model also assumes that all identifiable species are adsorbed on the catalyst surface except for CO_2 . Furthermore, it is also hypothesized that all the adsorption steps are in quasi-equilibrium with the photoconversion rates being controlled by intrinsic kinetics. Figure 8 reports a schematic description of the parallel-in series model during pollutant photodegradation representing the several types of photoconversion steps.

Acetone and acetaldehyde are the most representative VOC pollutants proposed, as model pollutants in the literature for photocatalyst and photoreactor testing. These species also represent two of the six classes of VOCs (aromatic, aldehyde, alkane, ketone, alcohol and chlorocarbon) and are present as intermediate species in numerous oxidation photocatalytic reactions of organics (e.g. benzene, phenol, toluene among others) ([Debono et al., 2013](#); [Debono et al., 2011](#); [Farhanian & Haghghat, 2014](#)). The understanding of the kinetic photodegradation of these compounds is extremely relevant in order to establish scale-up parameters and quantum efficiencies.

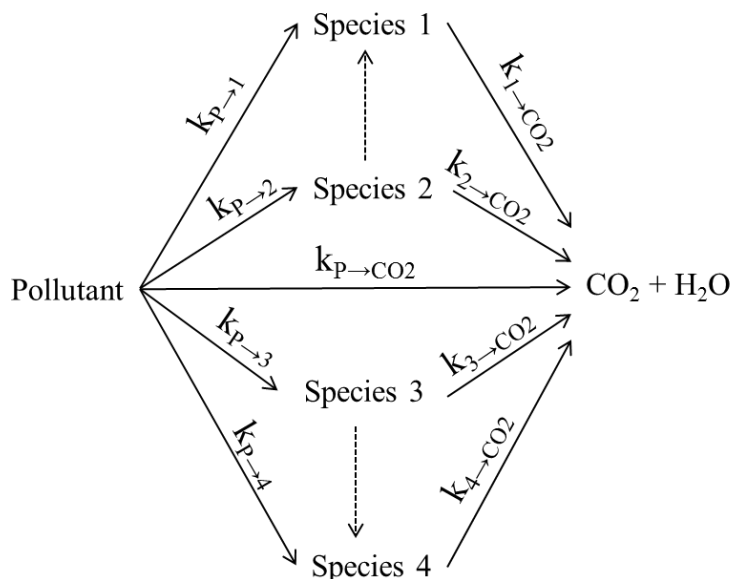


Figure 8: Generic Schematic Description of the Parallel-Series Model in the Photodegradation of the Pollutants and Various Intermediate Species. k_i represents the kinetic constant of the photocatalytic reaction in each step.

Many studies have reported kinetic and adsorption constants for the photodegradation of acetone and acetaldehyde. Tables 5 and 6 report several kinetic studies for the photodegradation of acetone and acetaldehyde using a Langmuir-Hinshelwood model.

Table 5. Summary of Kinetic Studies for Acetaldehyde Reported in the Literature.

Reactor	Size	TiO ₂	Irradiation	Intermediate compounds	Included in the model	Ind. K	Ref.
Monolith Reactor	3 x 6 in cylinder	Degussa P25	Two 10 W UV lamps 200-300 nm	Formaldehyde, Acetic Acid, Formic Acid	Yes	No	(Sauer & Ollis, 1996)
Flat Plate	5 x 10 cm plate	Degussa P25	UV 2.1 W/cm ²	No	-	No	(Sopyan, 2007)
Concentric Cylinder	55.08 l	Degussa P25	Eight 15 W UV lamps 325-385 nm	No	No	No	(Garcia-Hernandez et al., 2012)
Concentric Cylinder	14.7 l	Degussa P25	Eight 1 W UV lamps 325-385 nm	Possible acetic acid or formaldehyde	No	No	(Ibrahim & de Lasa, 2004)

Some studies (Ibrahim & de Lasa, 2004; Sauer & Ollis, 1996) agreed that acetaldehyde requires the inclusion of intermediate compounds for an adequate kinetic model. In the case of acetone, most studies agreed that the kinetic model for acetone does not need the addition of an intermediate compound. However, Chang et al. (2003) report that as the initial concentration of acetone becomes higher, the presence of intermediate species becomes more important.

Table 6. Summary of Kinetic Studies for Acetone Reported in the Literature.

Reactor	Size	TiO ₂	Irradiation	Intermediate compounds	Included in the model	Ind. K	Ref.
Monolith Reactor	3 by 6 in cylinder	Degussa P25	Two 10 W UV lamps 200-300 nm	No	-	Yes	(Sauer & Ollis, 1994)
Grid on Infrared Spec.	3 by 1 cm grid	Degussa P25	500 W UV lamps	No	-	Yes	(El-Maazawi, Finken, Nair, & Grassian, 2000)
Cylindrical reactor	20 l	Degussa P25	One 100 W UV lamps (200-300 nm)	No	-		(Peral & Ollis, 1992)
Bed flow	6 by 2.5 mm bed	Degussa P25	One 4 W UV	No	-	Yes	(Raupp & Junio, 1993)
Batch Reactor	15 x 18-5 x 300 mm	Degussa P25	One 10 W UV (365 nm)	At high concentrations	Yes	No	(Chang et al., 2003)
Batch Reactor	18 L	Microfibers TiO ₂	4 LED lamps (365 nm)	Formaldehyde	No	No	(Le Behec, Kinadjian, Ollis, Backov, & Lacombe, 2015)
Batch Reactor		Synthesized TiO ₂	One 500 W UVA (300-580 nm)	No	-	No	(Bettoni et al., 2013)
Petri Plate	10 cm diameter	N Doped TiO ₂	Vic Chemiluminescence (600- 3000 nm)	Acetaldehyde, Formaldehyde and Formic Acid	No	No	(Ballari et al., 2015)
Concentric Cylinder	55.08 l	Degussa P25	Eight 15 W UV lamps 325-385 nm	No	-	No	(Garcia-Hernandez et al., 2012)
Concentric Cylinder	14.7 l	Degussa P25	Eight 1 W UV lamps 325-385 nm	No	-	No	(Ibrahim & de Lasa, 2004)
Packed Bed	593 ml	Synthesized TiO ₂	Four 4 W florescent (365-370 nm)	No	-	Yes	(Coronado, Zorn, Tejedor-Tejedor, & Anderson, 2003)

Few studies estimate the adsorption constant “Ind. K” in independent equilibrium experiments (Coronado et al., 2003; El-Maazawi et al., 2000; Raupp & Junio, 1993; Sauer & Ollis, 1994). The calculation of the Langmuir adsorption parameters independently from the kinetics is favourable for the elimination of high parameter cross-correlation and therefore less parameter uncertainty (Moreira, Serrano, Ortiz, & de Lasa, 2012).

Most of the research in kinetic studies for acetone and acetaldehyde has been performed in bench scale reactors. On the other hand, the studies in the 55.1 liter Photo-CREC-Air Reactor were developed in a scaled up unit and represent in this respect a step forward for photocatalytic oxidation implementation. Even though the kinetic studies performed in this unit were satisfactory, adequate kinetic modeling in the scaled up 55.1 liter Photo-CREC-Air Reactor requires the following: a) the calculation of independent adsorption Langmuir parameters and b) the Langmuir-Hinshelwood equations based on a series-parallel model for the photodegradation of acetone/acetaldehyde.

2.10 Future perspectives

VOCs are predominant pollutants in air. While researchers have been concerned about people's exposure to indoor and outdoor environments of poor air quality, photocatalysis, appears to offer an effective approach to degrade VOC pollutants. Research in photocatalysis has focused mainly on the synthesis of new photocatalysts, radiation sources, reactor design and kinetic analysis.

However, most of these studies for VOC conversion were developed in small scale bench reactors. In these units, the photonic efficiency may be largely negatively affected by the reactor size and the ability to absorb photons. Therefore, studies in photon utilization and energy efficiencies are essential for future development of photocatalysis and scale up of photoreactors for air treatment.

In all these respects, the Photo-CREC Air Reactor configuration is a promising answer to scale-up issues, given its highly efficient mixing, catalyst-fluid contact and efficient

photon and TiO₂ interaction. The Photo-CREC-Air Reactor was designed in order to accomplish the following objectives:

- ✓ The design of a pilot plant scale photoreactor with high interaction between the photocatalyst, the radiation and the gas phase, with these factors being critical for the scale-up of these units.
- ✓ The assessment of TiO₂ immobilization methods for the photocatalytic degradation of pollutants.
- ✓ The evaluation of Quantum Yields and Photochemical Thermodynamic Efficiencies in a pilot plant scale reactor. In this respect, studies considering macroscopic balances and quantum efficiencies are of critical importance.
- ✓ The performance of a kinetic analysis of the photodegradation of model pollutants.

Previous research by our group has accomplished the following objectives:

- ✓ The improvement of the reactor configuration design of the Photo-CREC-Air Reactor in order to obtain high photocatalytic activity ([Garcia-Hernandez et al., 2010](#); [Ibrahim & de Lasa, 1999, 2002, 2003](#); [Romero-Vargas Castrillón & de Lasa, 2007](#)).
- ✓ The operation of the Photo-CREC-Air Reactor with high photocatalytic activity for acetone and acetaldehyde ([Garcia-Hernandez et al., 2012](#)).
- ✓ The assessment of photonic efficiencies using parameters such as: a) Apparent Quantum Yield ([Garcia Hernandez et al., 2010](#)), b) PTEF and c) Quantum Yields based on irradiated and transmitted photons ([Garcia-Hernandez, 2012](#)).
- ✓ The evaluation of a kinetic analysis using a simple kinetic model for the complete mineralization of pollutants to CO₂. Adsorption and kinetic constants were estimated using the photocatalytic degradation data.

It is our view, that new advances with the Photo-CREC Air Reactor will require enhanced mesh designs, based on a better understanding of photocatalyst-mesh interaction and on the photon fate using macroscopic radiation balances:

As a result of this, the following scope is proposed for this project:

- ✓ The immobilization of the photocatalyst on the support in a scaled up photoreactor. The photocatalyst has to be stable and strongly anchored to the used mesh or surface. It is necessary to have a photocatalyst that would operate in a reliable and stable manner.
- ✓ The effect of the immobilization method and photocatalyst film thickness on the photocatalytic activity and photonic efficiency. The photocatalyst activity is affected by the irradiated area. The immobilization method affects the particle agglomeration and therefore, the way in which the photons are absorbed on the photocatalyst.
- ✓ The comprehensive evaluation of Quantum Yields and PTEFs including intermediate species and absorbed radiation. The calculation of absorbed radiation requires that one includes macroscopic radiation balances that involve the incident, reflected and transmitted radiation.
- ✓ The establishment of Quantum Yield and PTEF limits in the Photo-CREC-Air reactor.
- ✓ The photocatalysis mechanism has to be well understood, and this is significant to accomplish the mineralization of VOCs as well as photoconversion of all intermediates species.
- ✓ The evaluation of a kinetic analysis based on a series-parallel model that includes all intermediate species and broader ranges of initial concentration.

To address these key matters, we consider here the photodegradation of acetone and acetaldehyde in a 55.1 L scaled-up Photo-CREC-Air Reactor. Two techniques are

considered: Spread Coating (SCM) and Air Assisted Spray (AAS) in conjunction with an Automatized Spinning Coating (TiO₂-AAS-ASC). The optimum thickness for full photon penetration of the TiO₂ impregnated mesh is studied (Lugo-Vega, Serrano-Rosales, & de Lasa, 2016).

Furthermore, a rigorous methodology must be established for the calculation of absorbed photons, OH^\bullet radical formation enthalpy and rates of OH^\bullet radical consumption. It should also be shown that apparent Quantum Yields (QY_{app}) depend on the combined effect of QYs for the photocatalyst and the photon absorption in the photoreactor. It also has to be proven that the series-parallel model is adequate for the photodegradation of VOC.

Chapter 3

3 Scope of Research

This chapter describes the objectives of this PhD Dissertation. This chapter includes: a) the general objectives of the project considered from a broad perspective, b) the particular objectives of the project and c) the objectives of each chapter as presented in this PhD dissertation.

3.1 General Objectives

The general objective of this PhD dissertation includes:

1. To study the effect of the irradiation field, attachment of photocatalyst onto the mesh and reaction scheme on the efficiency of a scaled up reactor Photo-CREC-Air to degrade acetone and acetaldehyde. Also, to extend the application of the proposed approach to scaled up units for air purification.

3.2 Particular Objectives

The present PhD dissertation was planned to achieve the experimental and theoretical objectives, which include:

1. To establish a new impregnation method for photocatalyst immobilization on a steel mesh. This new method shall allow both reproducible and stable loadings of photocatalyst.
2. To develop experiments in the Photo-CREC Air Reactor, degrading organic model pollutants such as acetone and acetaldehyde. This will be done with a special focus on the effect of model pollutant concentrations, as well as the effect of the immobilization method and the nature of pollutants on photoconversion kinetics. There will be a special emphasis, in the runs to be developed, on changes of immobilized photocatalyst loadings and their influence on the photocatalytic reaction rate.

3. To establish macroscopic energy balances including all the contributing terms such as incident photons, transferred photons and reflected radiation using a CREC periscopic device. These results will be compared with theoretically based Monte Carlo simulations accounting for the probabilistic evolution of the photons in the Photo-CREC Units.
4. To calculate energy efficiencies and PTEF factors and to link these parameters with the expected photoreaction and the photon utilization mechanism.
5. To propose criteria for the scale-up of the Photo-CREC Air Reactor, making recommendations to improve photocatalytic reactor performance.
6. To establish the efficiency limits of the PTEFs and QYs for acetone and acetaldehyde photodegradation. This would provide important information on the reactivity of the molecules and the use of hydroxyl radicals for the photodegradation.
7. To further develop reaction networks and kinetic models that will be adequate and applicable in describing photoconversion rates with different pollutant concentrations and types, as well as various photocatalyst loadings and levels of irradiation.

Figure 9 describes the previous mentioned objectives in a schematic format. The diagram shows how the experimental and theoretical research strategy followed.

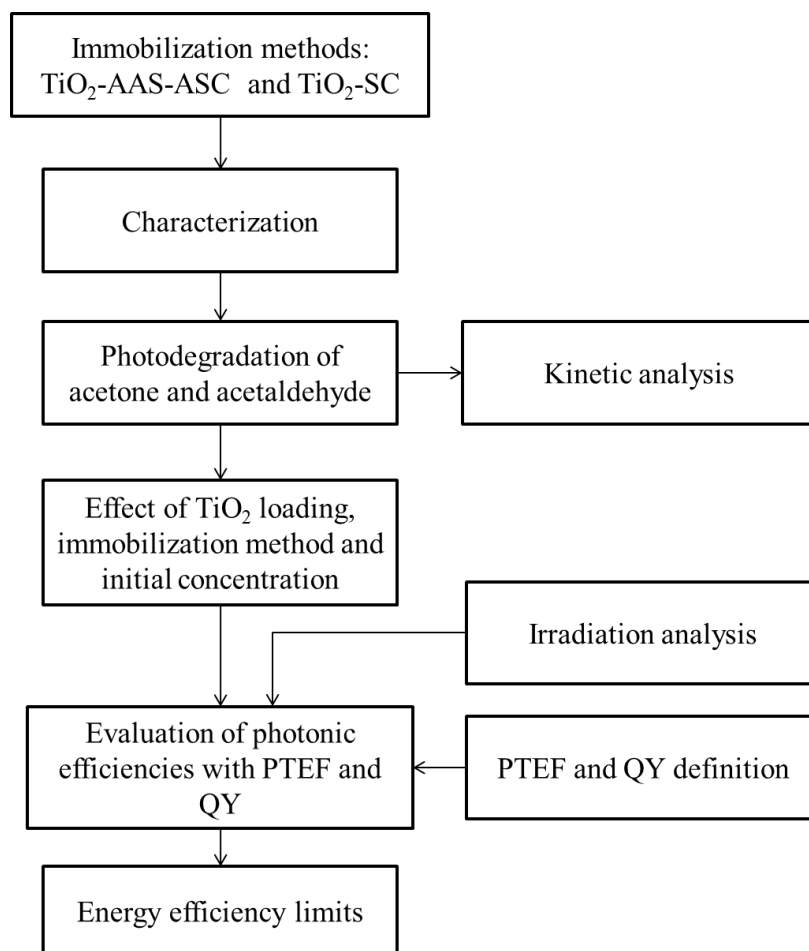


Figure 9: Schematic Description of the Particular Objectives Expected to be Achieved in this PhD Dissertation.

The topics presented in this diagram are divided in different sections as follows: 1) photocatalyst immobilization methods; 2) mesh characterization using surface science techniques; 3a) photodegradation of model pollutants: acetone and acetaldehyde and its 3b) kinetic analysis; 4) effect of the TiO₂ loading, immobilization method and initial concentration on the photodegradation activity; 5a) irradiation evaluation with macroscopic balances and, 5b) establishment of energy efficiency parameters (QY and PTEF) for, 5c) calculation of photonic efficiencies; and 6) estimation of energy efficiency limits.

This research strategy and its development are described in the various chapters of this PhD dissertation and further explained in the upcoming section.

3.2.1 *Mesh Characterization - Chapter 5*

The particular objectives of this section are:

1. The development of a TiO₂ Air Assisted Spray with Automatized Spinning Coating Method (TiO₂-AAS-ASC) and its comparison with a previous semiconductor Spread Method (TiO₂-SC).
2. The characterization of the methods TiO₂-SC and TiO₂-AAS-ASC in terms of homogeneity.
3. The evaluation of the film thickness and particle state for TiO₂-SC and TiO₂-AAS-ASC method.
4. The assessment of the stability of the immobilized TiO₂ when using the TiO₂-SC and the TiO₂-AAS-ASC Methods.

3.2.2 *Irradiation Evaluation and Establishment of Energy Efficiency Parameters – Chapter 6*

The particular objectives of this section are:

1. The establishment of the Quantum Yield definition based on the absorbed photons and the rate of hydroxyl radical consumed including both model pollutants and intermediate species.
2. The evaluation of the irradiation field in the Photo-CREC-Air Reactor.
3. The calculation of absorbed photons using on macroscopic balances and involving incident, transmitted and reflected photons.
4. The establishment of the Photochemical Thermodynamic Efficiency Factor (PTEF) including the calculation of the •OH radical formation.
5. The definition of apparent QYs and PTEFs as products of two variables: 1) An absorption factor (photoreactor configuration dependent parameter) and b) A Quantum Yield (photocatalyst dependent parameter).

3.2.3 *Effect of TiO₂ Loading and Photon Utilization while using the TiO₂-SC and TiO₂-AAS-ASC Meshes – Chapter 7*

The particular objectives of this section are:

1. The development of photodegradation experimental runs in the Photo-CREC-Air Reactor using acetone to evaluate the photocatalytic activity of the supported TiO₂ using the immobilization methods TiO₂-SC and TiO₂-AAS-ASC.
2. The study of the effect of the photocatalyst loading and of the initial acetone concentration on the photoreaction rate, using the TiO₂-SC and the TiO₂-AAS-ASC.
3. The calculation of Quantum Yields when using the TiO₂-SC and TiO₂-AAS-ASC methods.
4. The establishment of photon utilization when using TiO₂-SC and TiO₂-AAS-ASC meshes as a function of the particle agglomeration.

3.2.4 *Energy efficiency Limits –Chapter 8*

The particular objectives of this section are:

1. The calculations of the QYs and PTEFs for acetaldehyde and acetone photodegradation in the Photo-CREC-Air Reactor and using TiO₂-AAS-ASC initial concentrations in the 25-320 μmole/l range.
2. The establishment of the practical limits of QYs and PTEFs. The association of the limits with the nature of pollutants and photon utilization.

3.2.5 *Kinetic Analysis – Chapter 9*

The particular objectives of this section are:

1. The estimation of Langmuir adsorption parameters for acetone, acetaldehyde and intermediate species using equilibrium adsorption experiments in “dark” conditions.

2. The consideration of a series-parallel model for the photodegradation of acetone and acetaldehyde, using Langmuir-Hinshelwood kinetics.
3. The evaluation of kinetic parameters using various statistical indicators for both acetone and acetaldehyde, employing the TiO₂-AAS-ASC method with initial concentrations in the 25-320 μmole/l range.

Chapter 4

4 Experimental methods

This PhD dissertation addresses the photocatalytic degradation of organic pollutants in the gas phase. Different aspects of photocatalyst immobilization methods, kinetic analysis, irradiation evaluation and quantum efficiencies are considered. The scaled-up Photo-CREC-Air Reactor is employed as main experimental tool.

In order to do this, both equipment and experimental techniques were required to be established to obtain relevant results. In this respect, this chapter addresses: a) TiO₂ photocatalyst immobilization, b) mesh characterization in terms of homogeneity and morphology, c) Photo-CREC-Air Reactor operation and design, d) irradiation assessment, e) acetone and acetaldehyde photodegradation and f) adsorption isotherm evaluation.

4.1 TiO₂ Photocatalyst Immobilization

The TiO₂ was immobilized on a stainless steel 304 woven wire mesh supplied by Ferrier Wire (40x40 mesh count, 36% open area, 0.01 in wire diameter). With this aim, two methods were implemented: a) Spread coating (TiO₂-SC) and b) Air assisted spray with automatized spinning (TiO₂-AAS-ASC). The selection of this mesh was carefully effected to balance the open areas and the wire covered areas. With this end in view, a mesh with a 64% irradiated area and a 36% open area was selected. This approach provided: a) minimum opening blockages with TiO₂ particles following impregnation, b) a high air flow in the mesh openings with a limited pressure drop, c) a high degree of irradiation of the mesh surface.

The TiO₂-SC method involved the following steps: a) A water slurry containing 8wt% nonporous 35-36 m²/g, 21 nm mean particle diameter Aeroxide TiO₂ P25 was prepared; b) The particle slurry was applied with a brush on the 220 g stainless steel mesh. Following a time of approximately 10 minutes, the mesh was blown with compressed air from the interior of the cylinder to eliminate the excess of solution clogging the wire openings. The coated mesh was dried at room temperature for 24 hours.

Concerning the TiO_2 -AAS-ASC, the preparation procedures can be summarized as follows: a) A 150 Badger nozzle gun was positioned at 30 cm from the stainless steel mesh surface, b) The drum holding the stainless steel mesh was rotated at 12 RPM, c) The air pressure and TiO_2 concentration were set at 20 psia and 16wt%, respectively, d) The prepared TiO_2 slurry solution was sonicated for 20 minutes and then kept at continuous magnetic stirring in order to prevent TiO_2 settlement in the glass vial. e) The flow of the TiO_2 slurry spray was set to 15.7 mL/min. Appendix B shows the relation between air pressure and TiO_2 slurry volumetric flow. Figure 10 reports a schematic description of the AAS-ASC system.

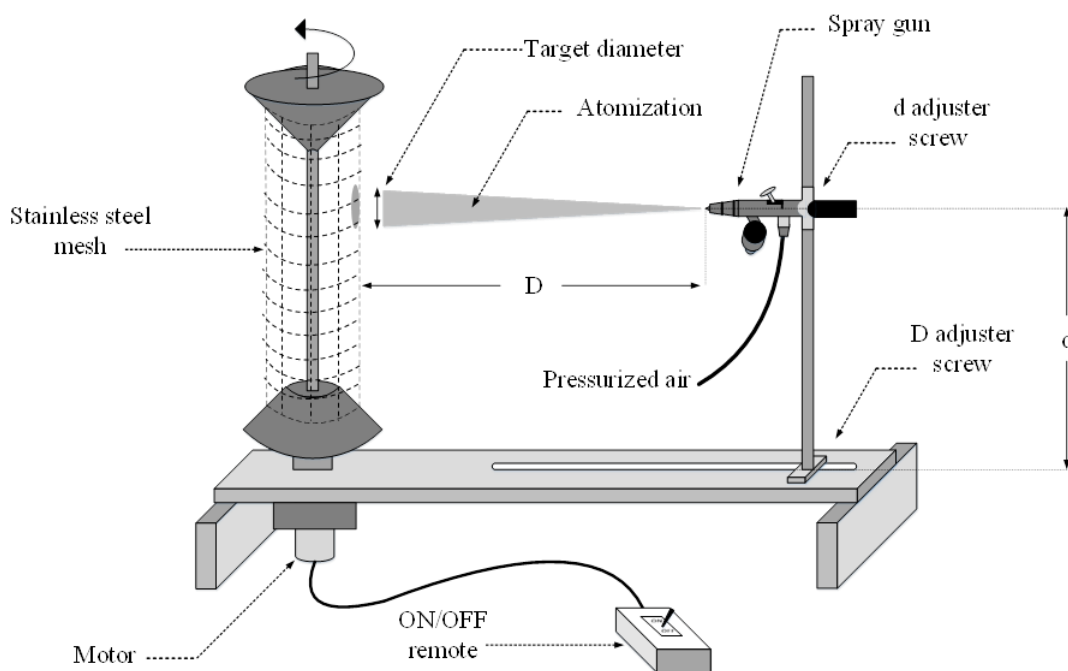


Figure 10: Schematic Diagram of the Automated Spray Coating (ASC) System. In the ASC apparatus, the spray gun can be moved both vertically and horizontally. The step size for vertical movement of the spray gun is 2 cm. This is the expected size of the target diameter.

It was observed that changes of the rotating speed, distance of the nozzle to the target, air pressure and TiO_2 slurry concentration were all factors influencing TiO_2 loadings

and TiO₂ agglomeration. Furthermore, the finally selected AAS-ASC coating conditions were chosen based on the best TiO₂ slurry flow leading to the most desirable droplet impact force, controlled droplet sizes and TiO₂ homogeneity. It was observed that a 16wt% atomized TiO₂ slurry with 1.31 mL slurry per drum revolution were the best conditions.

On this basis, the expected TiO₂ mass sprayed on the mesh was in this case, 5.8 gr. However, the actual amount of TiO₂ deposited on the mesh as established via gravimetry, was 2.2 gr on a 1220 cm² stainless steel wire mesh surface. This shows that the AAS-ASC displays an impregnation efficiency of 38%, with the resulting coating being both homogenous and free of agglomerates.

Different TiO₂ loadings were implemented to assess acetone photodegradation activity as follows: 1wt% to 3wt% TiO₂ for TiO₂-SC and 0.8wt% to 2wt% for TiO₂-AAS-ASC. Furthermore, acetaldehyde photodegradation was performed with the optimum TiO₂ immobilized mesh at 3wt% TiO₂ for TiO₂-SC and at 1% for TiO₂-AAS-ASC.

4.2 Mesh Characterization

The TiO₂ loading homogeneity was characterized by a local gravimetric method for both the TiO₂-SC and TiO₂-AAS-ASC. This encompassed the following steps: a) A TiO₂ immobilized mesh was divided into segments of 1 in² square area; b) The TiO₂ was removed from each segment using an ultrasonic bath for 2-3 hours; c) The local loading was calculated using a weight difference. Furthermore, the morphology and the thickness of the TiO₂ film were characterized by a Hitachi S-4500 Field Emission Scanning Electron Microscope (SEM) with a Quartz PCI XOne SSD X-ray Analyzer. Finally, the elemental analysis on the TiO₂ coated mesh was performed with Energy-Dispersive X-Ray Spectroscopy (EDX).

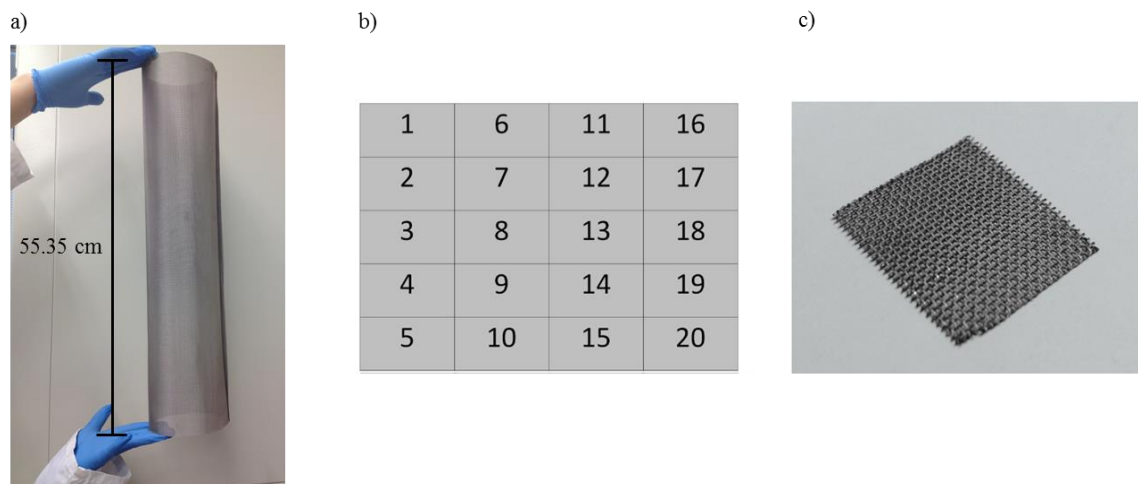


Figure 11: a) Photo of the Entire 55.4 cm x 34.7 cm TiO₂ Coated Stainless Steel Mesh. b) Schematic Representation of the 20 Identified Area Sections of the TiO₂ Impregnated Mesh Sample. c) Photo of the 1 in² Impregnated Mesh Considered for Further Analyses.

4.3 Photocatalytic Reactor Setup

The Photo-CREC-Air Reactor is a 55.1 L total volume unit operated in the CREC laboratories ([Garcia-Hernandez et al., 2012](#)). This unit was employed in the present study for the photodegradation of air pollutants. The present configuration is the result of significant design improvements as established using Computational Fluid Dynamics (CFD) ([Ibrahim & de Lasa, 1999](#); [Romero-Vargas Castrillón & de Lasa, 2007](#)). The Photo-CREC-Air Reactor design provides an effective interaction between a gas stream and the irradiated TiO₂ immobilized on the mesh. In addition, the modified Photo-CREC-Air Reactor permits macroscopic energy balances allowing the measurements of incident, transmitted and reflected radiation.

The entire Photo-CREC-Air can be viewed as a closed loop system. Figure 12 reports the main sections of the Photo-CREC-Air Reactor. In this unit, air is recirculated through the reactor with the help of a GASP gas blower. Air is pumped into a stainless steel Venturi, and subsequently driven into the reaction section. Before the air is sent back to the blower, it is cooled down using water at 5-10 °C. This allows the reactor operation to be

at close to isothermal conditions ($\approx 44^\circ\text{C}$). The reaction section includes eight 15 W nominal power UV lamps (EiKO Global, LLC) surrounding a quartz glass cylindrical tube (Figure 13a). The radiation wavelength supplied by the UV lamps ranges from 325 to 380 nm (Appendix C). The total mesh area is 1906 cm^2 where 1628 cm^2 is irradiated. The stainless steel mesh has open areas which equal to 36% of the total. Thus, 1042 cm^2 of the TiO_2 immobilized mesh is irradiated in the Photo-CREC-Air Unit. The TiO_2 coated mesh is located inside a quartz glass tube, supported by a bullet nose bottom. This design allows an even gas flow along the annular region and across to the interior of the mesh (Figure 13b).

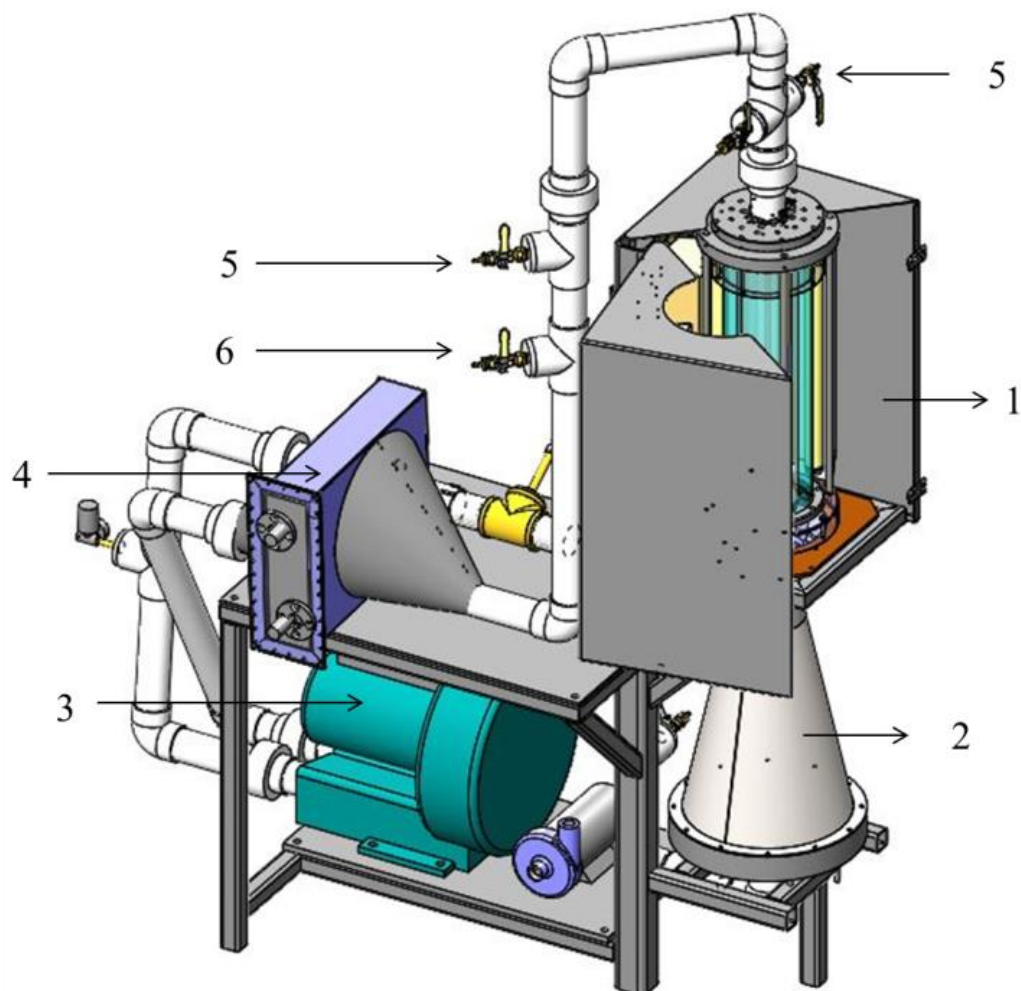


Figure 12: Schematic Diagram of the Photo-CREC Degradation System: (1) Reaction section, (2) Venturi section, (3) Blower, (4) Cooler, (5) Automatic sampling ports and (6) Injection port.

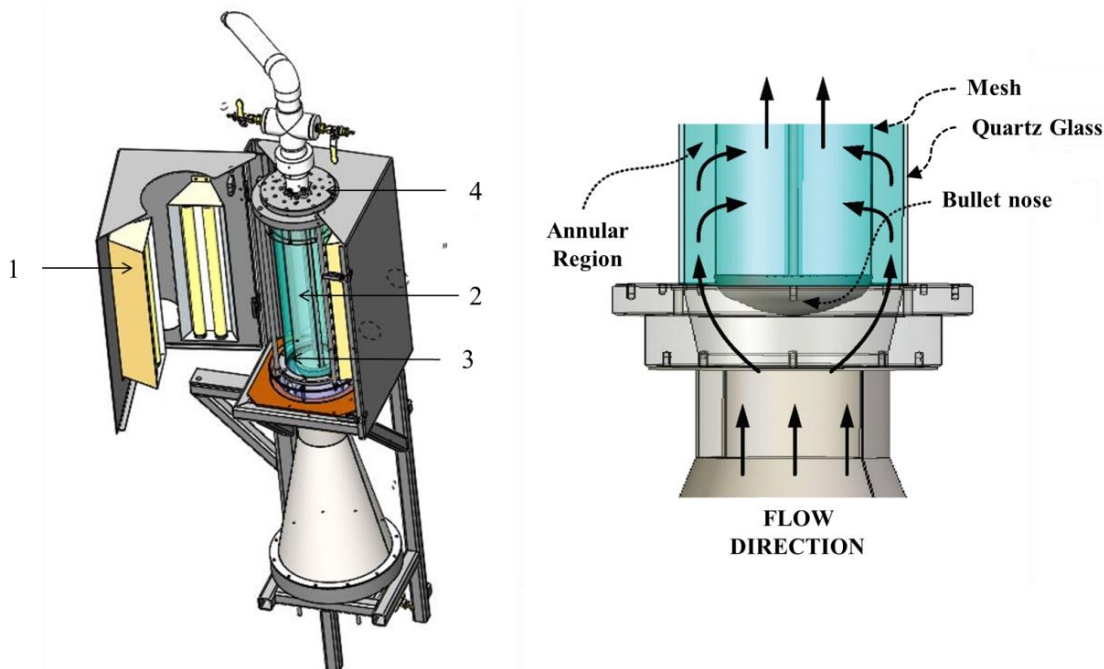


Figure 13: (a) Schematic Diagram of the Reaction Section: (1) Surrounding UV lamps, (2) Coated stainless steel mesh, (3) Quartz glass and (4) Perforated plate. (b) Schematic Diagram of the Cross-Flow Air Circulation through the TiO₂ Coated Mesh in the Photo-CREC-Air Reactor.

4.4 Irradiation Measurements

The radiation in the Photo-CREC-Air Reactor is measured using an optical probe. This optical probe is inserted through a perforated plate located on top of the Photo-CREC-Air Reactor. The optical probe itself involves a short 1cm horizontal entry section, a specular surface oriented at 45 degrees and a 2 m vertical fiber optic connected to a Stellarnet EPP3000 Spectrometer. This spectrometer measures radiation in the 200 to 1100 nm wavelength range. Figure 14b shows a schematic representation of the periscopic device. The optical fiber cable is housed in an aluminum pipe. Since the measurements are perpendicular to the cable, the optical fiber is contained in a polished aluminum body that allows measurements at 90 degrees. A calibration of this device was effected at different wavelengths, distances from the radiation source and irradiation intensities using the optical probe without the aluminum housing (Appendix D).

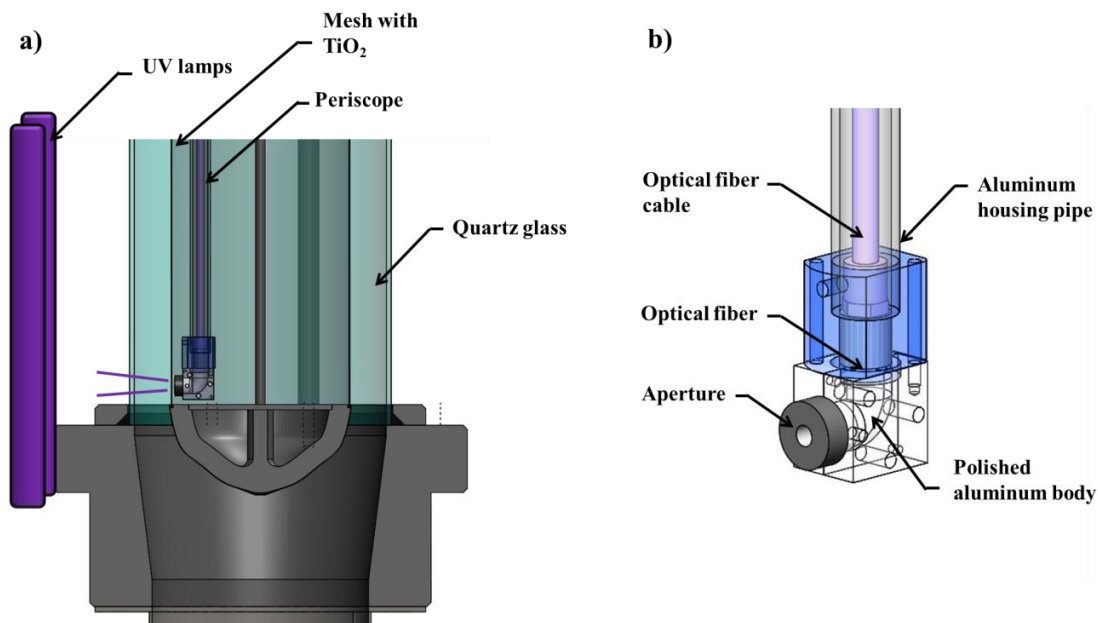


Figure 14: a) Orientation of the Periscopic Device in the Photo-CREC-Air Reactor.
b) Schematic Description of the Periscopic Device Components.

Another important feature of the Photo-CREC-Air unit is a perforated plate located at the top reactor section. This perforated plate allows the insertion of an optical probe. Figure 15a describes the perforated plate top view and the eight near-UV lamps location inside the four unit reflectors. Figure 15b illustrates a photon trajectory in the reactor. Photons irradiated by the near-UV lamps traverse the quartz glass, reaching the TiO₂ coated mesh (P_{irr}). At that instant, the photons contributing to P_{irr} can follow three possible paths: a) Photons can be absorbed by the semiconductor (P_{abs}), b) Photons can be reflected by the photocatalyst (P_{ref}) or c) Photons can move across the mesh (P_{trans}). The optical probe can be placed at different axial, circumferential and radial positions. This can be done in order to measure the incident, transmitted and reflected radiations and their distribution in the z axial and the θ angular coordinates.

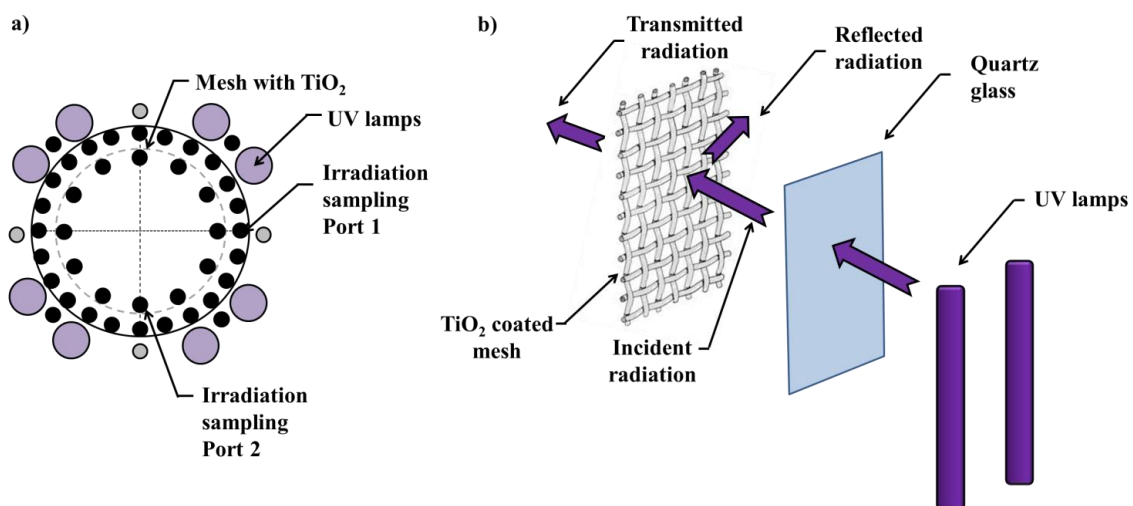


Figure 15: a) Schematic Representation of the Irradiation Sample Ports and their Locations (Port 1 and Port 2). Location of the near UV lamps is also provided, b) Description of the Photon Trajectory for Near-UV Lamps, Traversing the Quartz Glass and Reaching the Mesh. Photons can be absorbed, reflected or transmitted.

Figure 16b describes the three measurement positions using the two sets of radial port positions available (refer to Figure 15a):

a) *Port 1*. It is located between the quartz glass and the mesh. Port 1 allows measuring both the photons reaching the surface of the TiO₂ coated mesh (periscopic device facing the lamps) and the photons reflected by the mesh (periscopic device facing the mesh).

b) *Port 2*. It is located behind the mesh to measure the radiation transmitted through the mesh (periscopic device facing the mesh).

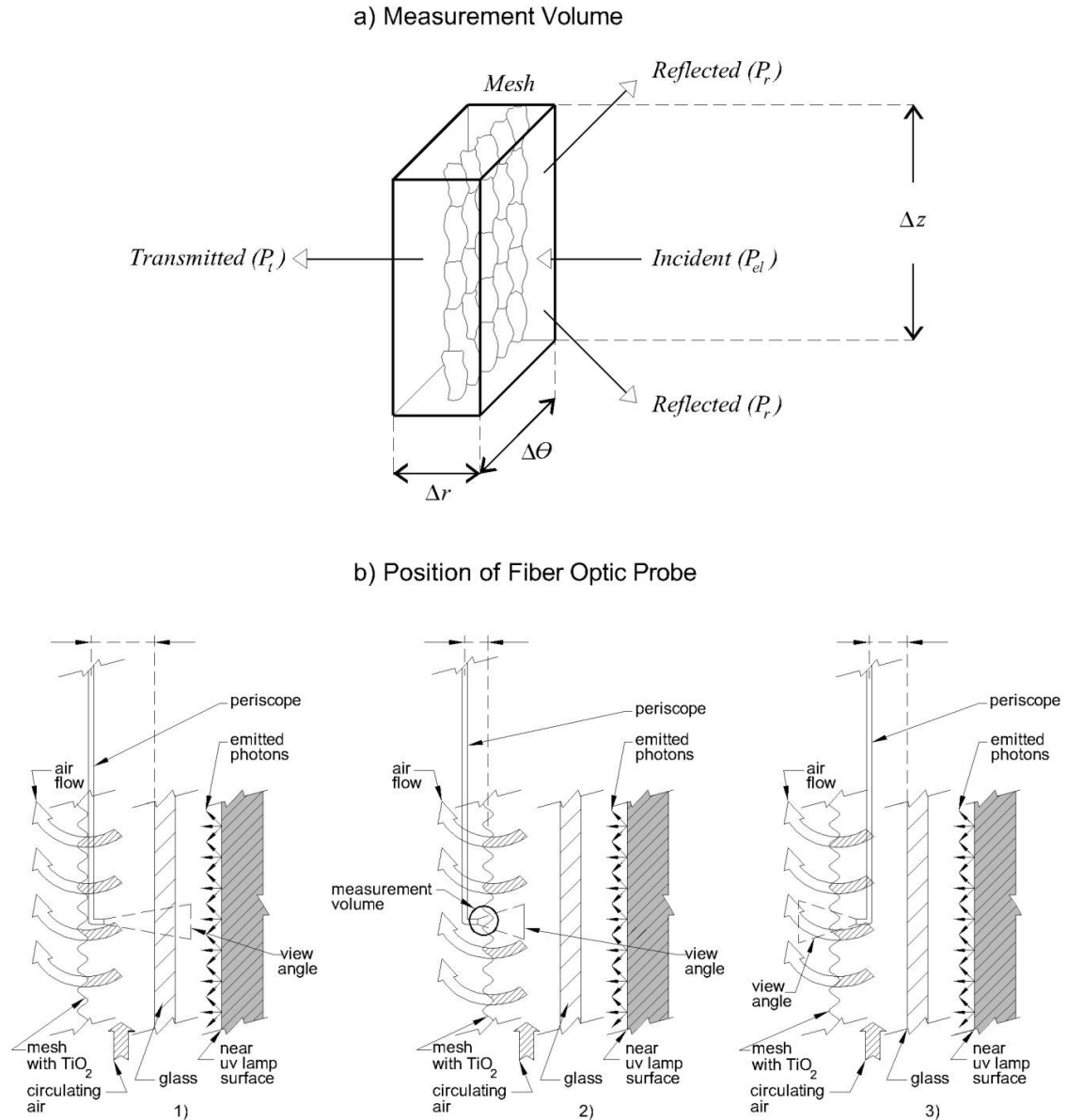


Figure 16: (a) Schematic Diagram of the Selected Control Volume for Macroscopic Local Radiation Balances. (b) Schematic Diagram of the Optical Probe Locations in the Photo-CREC-Air Reactor for Radiation Measurements as: (1) *Incident Radiation (P_{irr})*: The optical probe is placed in between the coated mesh and the quartz glass facing the UV-lamps, (2) *Transmitted Radiation (P_{trans})*: The optical probe is placed behind the coated mesh, (3) *Reflected Radiation (P_{ref})*: The optical probe placed in between the mesh and the quartz glass facing the coated mesh.

Regarding the incident reflected and transmitted photon rates (P_{irr} , P_{trans} and P_{Ref}), they were calculated using the following eq. involving z , θ and λ coordinates:

$$P = \frac{\int_{\lambda_{min}}^{\lambda_{max}} \int_0^{\infty} \int_0^{2\pi} q(\theta, z, \lambda) r d\theta dz d\lambda}{E_{av}} \quad (4.1)$$

where $q(\theta, z, \lambda)$ represents the radiation measured in $W/cm^2 \cdot nm$; λ stands for the radiation wavelength; θ and r represent the angular and radial positions respectively and E_{av} denotes the average photon energy.

On the basis of these measurements, local macroscopic radiation balances were implemented as shown in Figure 16a and using the following:

$$P_{abs} = P_{irr} - P_{trans} - P_{ref} \quad (4.2)$$

where P_a represents the photons absorbed by the immobilized photocatalyst.

4.5 Acetone Photocatalytic Degradation

The performance of the Photo-CREC-Air Unit with both TiO_2 -SC and TiO_2 -AAS-ASC meshes was established in the present study, utilizing the photocatalytic degradation of acetone and acetaldehyde. Initial concentrations of acetone and acetaldehyde varying from 25 $\mu mole/L$ to 320 $\mu mole/L$ were considered. In terms of analytical equipment, a Shimadzu 2014 Gas Chromatograph followed by a methanizer and a flame ionization detector (FID) were used to monitor CO_2 , acetone and intermediate species. These chemical species were separated using a Porapak Q column. Retention times for CO_2 , formaldehyde, methanol, acetaldehyde, formic acid and acetone were 2.2, 3.7, 4.7, 5, 5.6 and 8.2 minutes, respectively using a 55°C/min temperature ramp until 185°C was reached. Once this thermal level was achieved, the GC furnace was kept at this temperature for 8 min. The GC analytical program used with the selected parameters and typical GC chromatograms are reported in Appendix E.

Photodegradation experimental runs were performed using the following steps: (a) A 0.100-1 mL of organic model compound at 4°C was injected into the Photo-CREC-Air Unit via the liquid injection port. (The syringe and the volatile liquid container were kept cold on ice to avoid evaporation during injection). (b) The injected liquid samples were vaporized instantaneously and were allowed to mix for 30 min. This time, designated as the dark period (UV lamps are turned off) is the required time to allow all processes including adsorption to reach equilibrium. (c) Following this, the UV lamps were turned on. Irradiation typically took place for about 60-500 min. Gas samples were taken as frequently as required to properly describe the concentration changes. This ranged from every 15 min to 56 min, using an automatized gas sampler connected to the gas chromatograph. (d) Once all organic species depleted and converted into CO₂, runs were considered to be completed. In between runs, the impregnated TiO₂ was flushed with clean air free of organic species, under UV irradiation during 10 to 20 minutes to convert any remaining adsorbed hydrocarbons.

Regarding concentrations of the various chemical species at different irradiation times, they were recorded for further data analysis and kinetic modeling. Leak tests in the reactor are showed in Appendix F.

4.6 Adsorption Isotherm

The Langmuir equation provides a good description of the organic species adsorbed on the TiO₂ coated mesh at equilibrium ([Garcia-Hernandez et al., 2012](#)). On this basis, adsorption isotherms were developed for both TiO₂-SC and TiO₂-AAS-ASC meshes. The experimental procedure was as follows: a) A set 0.1 to 1mL of acetone volume was injected into the Photo-CREC-Air Reactor with the near UV lamps turned "off". b) Air samples were taken periodically (every 18min) until the gas phase acetone concentration reached a stable level. This condition was considered adsorption at equilibrium at 44 °C, atmospheric pressure. c) This procedure was repeated several times at various initial acetone concentrations in the 13-50 µmole/L range.

4.7 Conclusions

This chapter reports a new method for TiO_2 immobilization on a stainless steel mesh. The proposed method takes advantage of operating variables to obtain a homogeneous TiO_2 coating with small agglomerate particles. This chapter also highlights the special features of the Photo-CREC-Air Reactor and its special design to maximize the interaction between the gas phase, the solid phase and the radiation. Furthermore, a rigorous method for the accounting of incident, transmitted and reflected photons is considered. This allows the development of macroscopic energy balances and the assessment of the absorbed radiation. This is the case, given absorbed radiation plays a central role on the evaluation of photocatalyst and photoreactor energy efficiencies.

Chapter 5

5 Results and Discussion: Characterization of TiO₂-SC and TiO₂-AAS-ASC

This chapter reports the critical importance of the particle state in TiO₂ immobilized photocatalysis. To address this, TiO₂ coatings are prepared using two methods: an Air Assisted Spray with an Automatized Spinning Coating (TiO₂-AAS-ASC) and a Spread Coating (TiO₂-SC). The state of the TiO₂ particles is investigated using SEM and local gravimetry. It is proven that the TiO₂-AAS-ASC displays homogeneity, limited particle agglomeration, close to optimum thickness and stability under flow.

5.1 Gravimetric method

The local loading of the TiO₂-SC and TiO₂-AAS-ASC meshes was measured with the method described in the section 4.2. Figure 17 reports the local TiO₂ loading distribution for a 2.2wt%: a) TiO₂-SC mesh loading and (b) TiO₂-AAS-ASC mesh loading. One can notice that the local loadings of TiO₂-SC (Figure 17a) display a standard deviation of 0.62wt%. In contrast, one should observe that the TiO₂-AAS-ASC (Figure 17b) shows a much reduced 0.12wt% standard deviation. This demonstrates the more uniform coating achieved with the TiO₂-AAS-ASC mesh versus the TiO₂-SC.

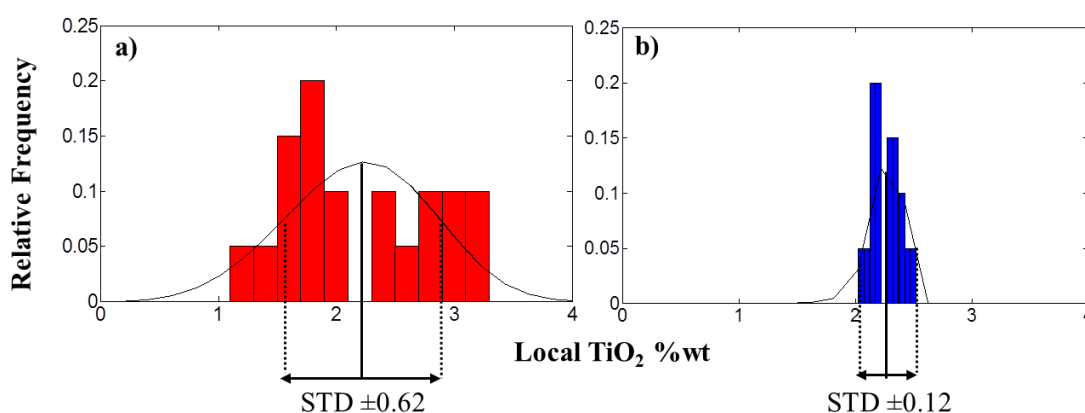


Figure 17: TiO₂ Local Weight Loading Distribution on the Mesh Prepared using a) the TiO₂-SC method and b) the TiO₂-AAS-ASC method.

5.2 Energy Dispersive X-Ray Spectroscopy (EDX)

Energy Dispersive X-Ray Spectroscopy was used to determine the elemental analysis on the surface of the film (1 micron depth). Table 7 reports the Energy Dispersive X-Ray Spectroscopy (EDX) analysis for randomly selected areas on the TiO₂-SC and TiO₂-AAS-ASC meshes. The data of this table further supports the findings that better coatings are obtained with the TiO₂-AAS-ASC mesh rather than with the TiO₂-SC mesh.

Table 7. EDX Analysis of Different Area Sections of the TiO₂ Coated Stainless Steel Meshes Using TiO₂-SC and TiO₂-AAS-ASC Methods.

		C	O	Ti	Cr	Fe
TiO₂-SC	Area 1	3.5	56.6	39.3		0.6
	Area 2	8.2	15.8	8.9	12.9	48.8
	Area 3	3.1	55.7	41.1		
TiO₂-AAS-ASC	Area 1	2.4	36.3	59.9	0.3	1.2
	Area 2	3.5	43.8	48.1	1.0	3.6
	Area 3	4.5	51.9	41.9	0.3	1.2

One can also see in Table 7, that if the Ti element is used as the tracing element for TiO₂, then the 1, 2 and 3 areas, yielding Ti on the TiO₂-SC mesh, vary in the 8.9-41.1% wide range. On the other hand, when using the TiO₂-AAS-ASC mesh, the Ti element as measured by SEM-EDX was observed to be changing both in a higher and narrower 40-60% range. The observed Cr, C and Fe elements can be used to trace cracks in the TiO₂ films. For instance, in the case of TiO₂-SC, high Fe, Cr and C variations (0.6-48% Fe, 0-12% Cr and 3.1-8.2% C) show significant film thickness changes. On the other hand, close to constant values for TiO₂-AAS-ASC (1.2-3.6% Fe, 0.3-1% Cr, 2.4-4.5% C)

demonstrate a rather uniform film thickness. In other words, SEM-EDX can be used to confirm the better properties of the TiO₂-AAS-ASC mesh coating.

5.3 Scanning Electron Microscopy (SEM)

In order to further support the results of the TiO₂-AAS-ASC better-quality coating, SEM micrographs were taken from both 3wt% TiO₂-SC and 1wt% TiO₂-AAS-ASC samples. Figures 18a and 18b report the SEM micrographs for the TiO₂-SC and the TiO₂-AAS-ASC impregnated meshes, respectively. One can notice that in Figure 18a, the TiO₂-SC coating presents light gray areas showing uncoated stainless steel (island on the mesh) and areas in dark gray showing the TiO₂ coating. In this case, one can also observe that TiO₂ accumulates mainly in the wire joints leaving uncovered islands in other mesh surfaces. Thus, the TiO₂-SC mesh leads to distinctive coated and uncoated regions. On the other hand, for TiO₂-AAS-ASC, Figure 18b shows an essentially fully coated mesh surface with a uniform TiO₂ layer over the entire surface. This is a mesh surface free of shiny uncovered areas. In spite of this, it was also noticed that increasing the TiO₂ loading led to films more prone to the formation of cracks for TiO₂-AAS-ASC.

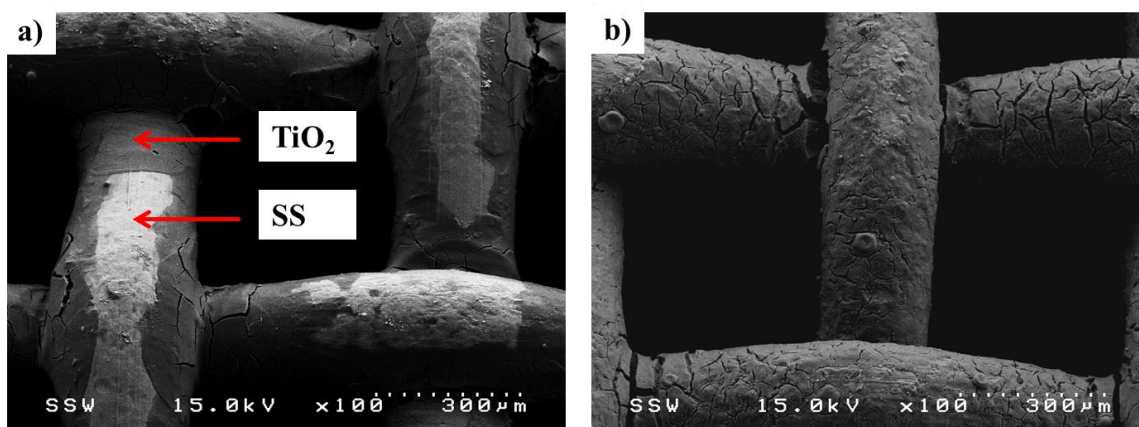


Figure 18: SEM Micrographs of Stainless Steel Mesh Coated with a) 3wt% TiO₂ using the TiO₂-SC and b) 1% TiO₂ using the TiO₂-AAS-ASC.

Figure 19 reports SEM micrographs showing the TiO₂-SC and TiO₂-AAS-ASC coating thicknesses. Figure 19a gives a TiO₂-SC thickness of 22.9 µm while Figure 19b provides

a TiO₂-AAS-ASC thickness in the 6-10 μm range. These results provide evidence of the much thinner thickness provided by the TiO₂-AAS-ASC.

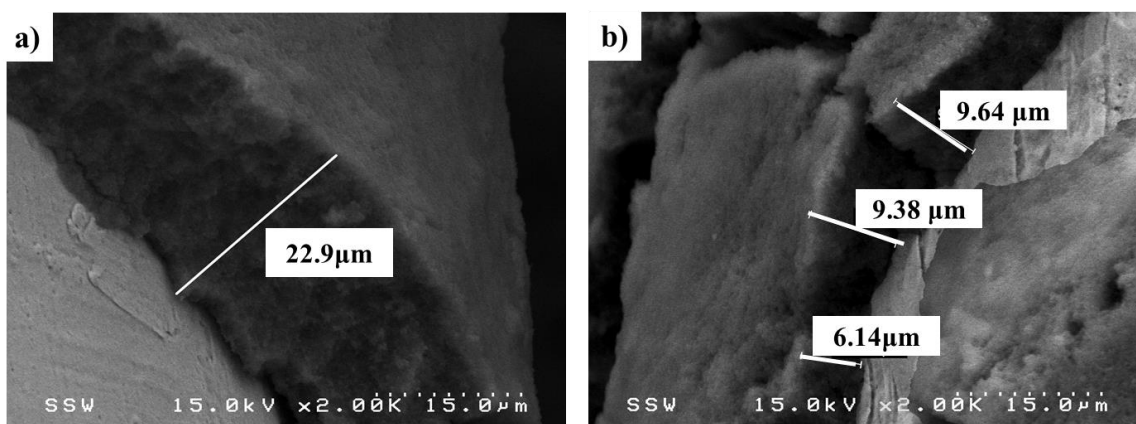


Figure 19: SEM Micrographs of Measured 1%wt TiO₂ Coating Thicknesses Using a) TiO₂-SC and b) TiO₂-AAS-ASC.

Figure 20 reports the dependency of the TiO₂ loading on the film thickness measured using SEM (Figure 19) on both TiO₂-SC and TiO₂-AAS-ASC meshes. Average film thickness (measured on different locations of the mesh for each loading) increases linearly with the TiO₂ loading for both methods.

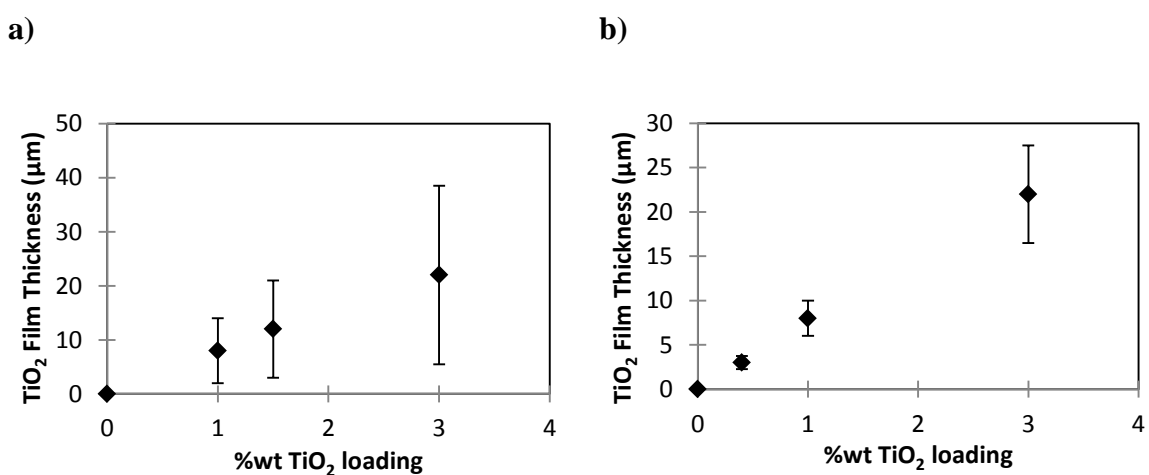


Figure 20: Effect of the TiO₂ loading on the film thickness for a) TiO₂-SC and b) TiO₂-AAS-ASC.

TiO₂-SC shows a high standard deviation of approximately 75% of thickness while TiO₂-AAS-ASC shows a standard deviation of 25% of the thickness. These results represent the TiO₂ thickness variation in terms of loading and deposition method.

Figure 21 shows an overview of the TiO₂ particles on the TiO₂-SC and TiO₂-AAS-ASC impregnated mesh areas. One can notice that the agglomeration of particles when using the TiO₂-SC is clearly more predominant than that when utilizing the TiO₂-AAS-ASC. In addition, in the case of the TiO₂-AAS-ASC, the particles are more homogeneously distributed on the surface than when using the TiO₂-SC.

On this basis, one can attest that the differences of the particle homogeneous distribution and particle agglomeration are coating method dependent. The changes of slurry flow, motor speed and air pressure are all factors leading to a controlled deposition of the TiO₂ coating. In fact, the small droplets produced by the atomizer lead to a better dispersion of the TiO₂ particles generating as a result less agglomeration (Han et al., 2012).

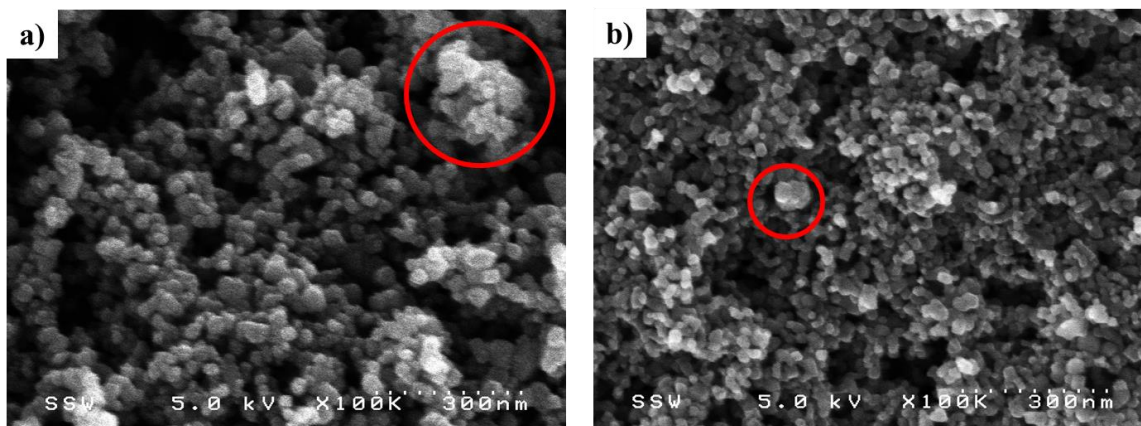


Figure 21: SEM Micrographs of the Surface of the Impregnated TiO₂: a) TiO₂-SC and b) TiO₂-AAS-ASC. Red circles show typical particle agglomerates.

The proposed AAS-ASC coating technique achieved both uniform and homogeneous coating. As well, accurate TiO₂ loadings with little particle agglomeration are obtained. These features are a result of the following steps:

- a) Step1: Selection of the adequate auxiliary air pressure used to adjust spray flow. This is a key parameter determining precursor size droplets for a given gun geometry.

- b) Step 2: Selection of the proper distance between the target and the spray gun. This influences both the force and the velocity of the precursor droplets at the point of impact.
- c) Step 3: Selection of mesh supporting drum speed. This parameter is of significance to promote uniform and controlled coating.

The successful implementation of the AAS-ASC method led to small slurry droplets (e.g. 100 microns) sticking to a rotating mesh with a resulting homogeneous distribution of TiO_2 particles.

5.4 Stability of the Immobilized TiO_2 using the TiO_2 -AAS-ASC Method

Furthermore, and in order to establish the stability of the prepared TiO_2 -AAS-ASC coated mesh, a 1906 cm^2 mesh area, was exposed to $375 \text{ m}^3/\text{h}$ of air flow during 1000 hours. Figure 22 reports the loading stability of the immobilized photocatalyst prepared using the TiO_2 -AAS-ASC method. One can notice that total TiO_2 losses are lower than 10wt% after 1000 hours of operation. One can also observe that these particle losses occur mainly during the first 100 hours. After this initial period, the TiO_2 weight remains essentially unchanged within 2%.

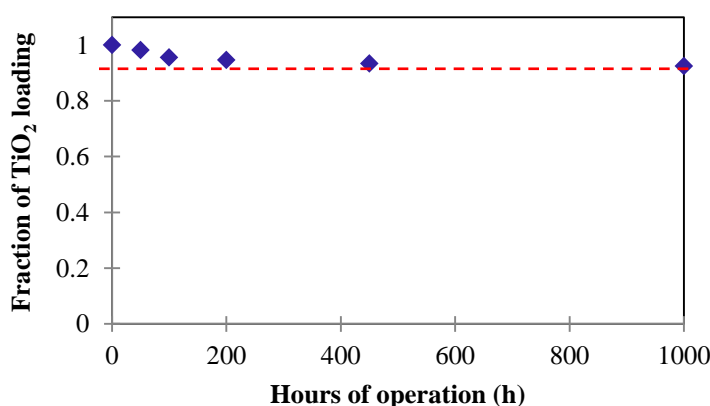


Figure 22: Changes of TiO_2 Loading with a TiO_2 -AAS-ASC Mesh during 1000 Hours of Operation.

In this case, it was observed that when using the gravimetric method, less than 10wt% of the TiO₂ loaded was lost. Therefore, one can conclude that the TiO₂ particle adhesion forces to the stainless steel mesh in the TiO₂-AAS-ASC are significant and are in excess to the forces promoted by the fluid flow in the Photo-CREC-Air unit.

The TiO₂ is attached to the support by absorption of the semiconductor particles on the stainless steel as a result of the impact and shear forces. The attractive forces between the support and the TiO₂ particles are mainly Van der Waals, electrostatic and hydrogen bonding (Dahmash & Mohammed, 2016). This results in a non-expensive method that produces a homogeneous and stable coating.

5.5 Conclusions

- a) Photocatalyst immobilization on a stainless steel mesh for a scaled up Photo-CREC-Air Reactor requires special coating methods. This is needed to achieve stable and highly performing TiO₂ meshes.
- b) A gravimetric method and SEM-EDX techniques were implemented in order to characterize the homogeneity and morphology of the TiO₂ films supported by TiO₂-SC and TiO₂-AAS-ASC.
- c) Air assisted spray in conjunction with an automatized spinning coating method (TiO₂-AAS-ASC) shows to provide a uniform and stable TiO₂ particle coating with little agglomeration.
- d) These results are of high importance to determine the reliability of the photodegradation results.

Chapter 6

6 Results and Discussion: Energy efficiency evaluation

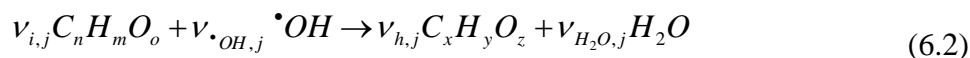
The establishment of the QY and PTEF efficiency parameters is a relevant issue for photocatalyst evaluation and reactor design. In this chapter, a detailed description of the QY and PTEF definitions is reported. Once, the definitions of QY and PTEF are established, they are used to evaluate photocatalytic efficiency in the PhD dissertation chapters that follow.

6.1 Quantum Yield

The Quantum Yield expresses photonic efficiencies in a photocatalytic reactor. A suitable definition for the QY is the ratio of $\bullet OH$ radicals consumed over the photons absorbed on the immobilized TiO_2 with a wavelength smaller than 388nm ([Garcia-Hernandez et al., 2010](#)), such as:

$$QY = \frac{\text{rate of } \bullet OH \text{ consumed}}{\text{rate of photons absorbed by the photocatalyst with } \lambda \leq 388nm} \quad (6.1)$$

The rate of $\bullet OH$ radicals consumed as in Eq. 6.1, can be calculated using an “indirect method” based on the stoichiometric requirements for the oxidation of the observable chemical species ([Garcia-Hernandez et al., 2012](#)). Following this, the “i” lower oxidation state species ($C_nH_mO_o$) can be converted with the help of $\bullet OH$ radicals to “h” higher oxidation state species ($C_xH_yO_z$) as follows:



where $\nu_{i,j}$ and $\nu_{h,j}$ represent the stoichiometric coefficients for $C_nH_mO_o$ and $C_xH_yO_z$, respectively. One should note that all species involved in the “j” step have to comply with carbon, hydrogen and oxygen element balances as shown in equations 6.3a, 6.3b and 6.3c:

$$v_{i,j}n - v_{h,j}x = 0 \quad (\text{Elemental carbon balance}) \quad (6.3a)$$

$$v_{i,j}m + v_{\bullet OH,j} - v_{h,j}y - 2v_{H_2O,j} = 0 \quad (\text{Elemental hydrogen balance}) \quad (6.3b)$$

$$v_{i,j}o + v_{\bullet OH,j} - v_{h,j}z - v_{H_2O,j} = 0 \quad (\text{Elemental oxygen balance}) \quad (6.3c)$$

Therefore,

$$r_{\bullet OH,T} = \sum r_{\bullet OH,j} = \sum \frac{v_{\bullet OH,j}}{v_{i,j}} r_{i,j} \quad (6.4)$$

where $r_{\bullet OH,j}$ is the rate of $\bullet OH$ radical consumption in step “j” of the network, $r_{i,j}$ is the reaction rate of the compound “i” in step “j”, and $v_{i,j}$ is the stoichiometric coefficient for chemical species “i” in step “j”.

Using this approach, the total $\bullet OH$ consumption rate of Eq. 6.4, can be calculated as a summation of observable individual species rates times the ratio of corresponding stoichiometric coefficients.

As a result, the QY as in Eq. 6.1 can be expressed as:

$$QY = \frac{-A_{irr} \sum_1^j r_{\bullet OH,j}}{P_{abs}} = \frac{A_{irr} \sum_1^j \frac{v_{\bullet OH,j}}{v_{i,j}} r_{i,j}}{P_{abs}} \quad (6.5)$$

where

$r_{\bullet OH,j}$ = the rate of $\bullet OH$ radical consumption in step “j” (mole/cm²_{irr}·s)

$r_{i,j}$ = the rate of “i” pollutant molecules degraded in the step “j” of the photoconversion (mole/cm²_{irr}·s)

$\nu_{i,j}$ = the stoichiometric coefficient involved in the photoconversion of the species “i” in step “j”

P_{abs} = the rate of photons absorbed by the photocatalyst with $\lambda \leq 388$ nm (mole of photons/s)

A_{irr} = the total area of the irradiated photocatalyst-impregnated mesh, 1042 cm²

On this basis and taking into account the considerations of Eq. (4.1), the QY in a non-isoactinic reactor as in Eq. (6.5) becomes,

$$QY = \frac{A_{irr} \sum_1^j \frac{\nu_{\bullet OH,j}}{\nu_{i,j}} r_{i,j}}{\int_{\lambda_{min}}^{\lambda_{max}} \int_0^{\infty} \int_0^{2\pi} q_a(\theta, z, \lambda) r d\theta dz d\lambda} E_{av} \quad (6.6)$$

where q_a accounts for the absorbed radiation in $\mu\text{W}/\text{cm}^2\text{-nm}$. The denominator is calculated using macroscopic balances as described in Eq. (4.2). Integrals of the radiation in Eq. (6.6) were calculated using experimentally obtained data.

Thus, once Eq. (6.6) is established, the actual $r_{i,j}$ values measured experimentally can be used to calculate the $r_{\bullet OH,j}$ in compliance with Eq. (6.4).

One can also set an upper limit for this equation, as defined in Appendix A, with a QY_{max} being equal to 1.33 or 133%. Thus, the QY s and their deviations from the maximum 133% value reflect the extent of the utilization of absorbed photons for the production of moles of $\bullet OH$, being consumed in the various photocatalytic steps.

Furthermore, and from a practical engineering design point of view, one is interested in considering a QY_{app} or apparent Quantum Yield based on the irradiated photons as follows:

$$QY_{app} = \frac{-A_{irr} \sum_1^j r_{OH^{\bullet},j}}{P_{irr}} = \frac{A_{irr} \sum_1^j \frac{v_{OH,j}}{v_{i,j}} r_{i,j}}{P_{abs}} \frac{P_{abs}}{P_{irr}} \quad (6.7)$$

$$QY_{app} = QY\eta_{abs} \quad (6.8)$$

The use of Eq. (6.7) in the $QY \eta_{abs}$ equation has the advantage of separating the intrinsic Quantum Yield (QY) for the photocatalyst from the efficiency of photon absorption (η_{abs}). In order to take full advantage of Eq. (6.7), one has to have the ability to implement macroscopic energy balances, as proposed in the present study.

One should also notice that the $r_{i,j}$ term in Eq. (6.7) can be represented by using the absorbed irradiation and a Langmuir Hinshelwood kinetic, as proposed by Ibrahim and de Lasa ([Ibrahim & de Lasa, 2004](#)).

6.2 Reaction rates for $\bullet OH$ Radicals

Acetone Photodegradation

In order to establish the photoreaction rate for $\bullet OH$ radicals involved in acetone degradation, a reaction mechanism has to be defined. In the present study, acetaldehyde was identified as an intermediate species in acetone photoconversion. This result is in agreement with other studies ([Bianchi et al., 2014](#); [Hauchecorne & Lenaerts, 2013](#)) which consider acetaldehyde as an intermediate species. This was shown using both Fourier Transform Infrared Spectroscopy and X-Ray Photoelectron Spectroscopy.

In this respect, a series-parallel model shown in Figure 23, appears to be suitable for the photodegradation of organic compounds on immobilized TiO_2 ([Bettoni et al., 2013](#); [Ortiz-Gomez, Serrano-Rosales, Salaices, & de Lasa, 2007](#)). This reaction network is consistent with the expected local variations of photon density in the Photo-CREC-Air Unit.

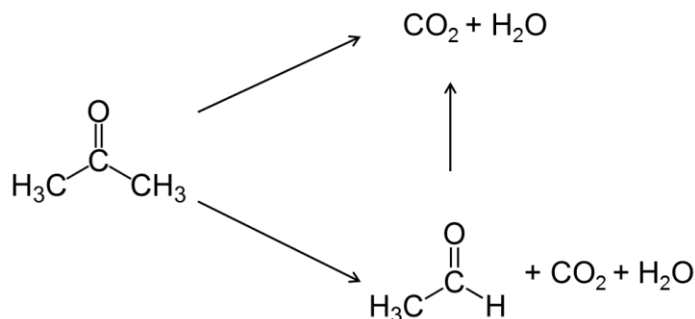
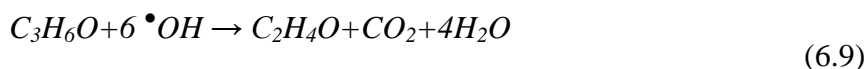
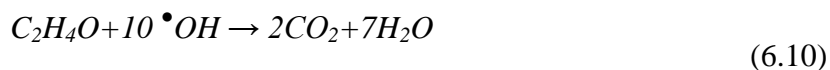


Figure 23: Schematic Representation of the Proposed Mechanism for the Photodegradation of Acetone in the Photo-CREC-Air Reactor.

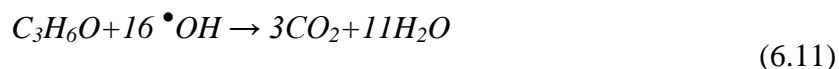
Furthermore, a $\bullet OH$ radical consumption stoichiometry for every photodegradation step can be obtained considering the following:



Acetone + Hydroxyl Radicals \rightarrow Acetaldehyde + Carbon Dioxide + Water



Acetaldehyde + Hydroxyl Radicals \rightarrow Carbon Dioxide + Water



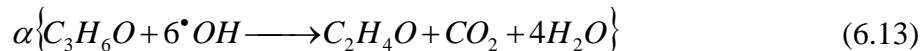
Acetone + Hydroxyl Radicals \rightarrow Carbon Dioxide + Water

One should note that the acetaldehyde concentrations are in the range of non-detectable limits at 24-50 $\mu\text{mole/L}$ initial acetone concentrations. For higher initial concentrations however, the combined concentration of acetaldehyde in the gas and solid phase can become measurable. As a result, acetaldehyde may become important for both kinetic modeling and quantum efficiency calculations. Therefore, a method for a QY evaluation for acetone photodegradation with acetaldehyde as an intermediate species is proposed stating the following,

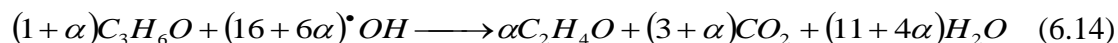
a) The complete mineralization of acetone to CO_2 :



b) The partial oxidation of acetone to acetaldehyde where α is a factor that establishes the fraction of acetone involved in the partial oxidation step is given by:



By multiplying eq. 6.13 by a α factor, and by adding the resulting equation to equation 6.12, the following is obtained:



Thus, and on this basis, the α and an $\cdot OH$ consumption rate can be related as:

$$\frac{r_{Acetone,T}}{-(1 + \alpha)} = \frac{r_{CO_2}}{(3 + \alpha)}, \quad \alpha = -\frac{(3r_{Acetone,T} + r_{CO_2})}{r_{Acetone,T} + r_{CO_2}} \quad (6.15)$$

$$r_{\cdot OH} = \frac{r_{CO_2}(16 + 6\alpha)}{(3 + \alpha)} \quad (6.16)$$

where $r_{(CO_2)}$, represents the rate of CO_2 formation, $r_{Acetone,T}$ stands for the total rate of acetone conversion and $r_{\cdot OH}$ denotes the $\cdot OH$ radicals consumed in the degradation of acetone. All of these variables are expressed in $\mu\text{mole}/\text{m}^2_{\text{irr}} \text{min}$.

The $r_{(CO_2)}$ rate can be calculated by using the measured CO_2 production. Furthermore, the $r_{Acetone,T}$ can be obtained with the $r_{Acetone,g}$ and the $(1 + K'_{acetone})$ factor. This factor accounts for the acetone adsorbed (Garcia-Hernandez et al., 2012), as shown in the following equations:

$$r_{Acetone,T} = (1 + K'_{acetone})r_{Acetone,g} \quad (6.17)$$

$$K'_{Acetone} = \frac{K^A_{Acetone} W Q_{acetone,max}}{V} \quad (6.18)$$

where W is the photocatalyst weight in g and V is the volume of the reactor in l.

Acetaldehyde Photodegradation

Regarding acetaldehyde photoconversion, in the present study, formaldehyde, methanol and formic acid were identified and quantified as intermediate species. As a result, a series-parallel model for acetaldehyde mineralization including the above mentioned intermediate species was considered for kinetic modeling as reported in Chapter 9.

Therefore, the hydroxyl radical consumption for the acetaldehyde photodegradation is the sum of each oxidation step,

$$r_{\bullet OH,T} = \sum r_{\bullet OH,j} = \sum \frac{\nu_{OH,j}}{\nu_{i,j}} r_{i,j} \quad (6.19)$$

where $r_{\bullet OH,j}$ represents the rate of total $\bullet OH$ radical consumption, $r_{\bullet OH,j}$ accounts for the rate of $\bullet OH$ radical consumption in step “j” (mole/cm²_{irr}·s), $r_{i,j}$ states the rate of “i” pollutant molecules degraded in the step “j” of the photoconversion (mole/cm²_{irr}·s), $\nu_{i,j}$ and $\nu_{OH,j}$ denote the stoichiometric coefficients involved in the photoconversion of the species “i” and “OH”, respectively, in step “j”.

6.3 Radiation Flux Balance and Photon Number

Using the above described experimental approach, radiation distributions at various axial and angular locations were calculated. Figures 24a, 24b and 24c report a colored map graph of the incident radiation, reflected radiation and transmitted radiation, respectively. The figures show the significant influence of the 8 lamps and 4 reflectors in the establishment of the radiation field. On this basis, it was observed that the incident radiation is about 10 times and 4 times higher than the reflected radiation and transmitted radiation, respectively. Furthermore, Table 8 reports the integrated photon flux values calculated on the basis of radiation measurements.

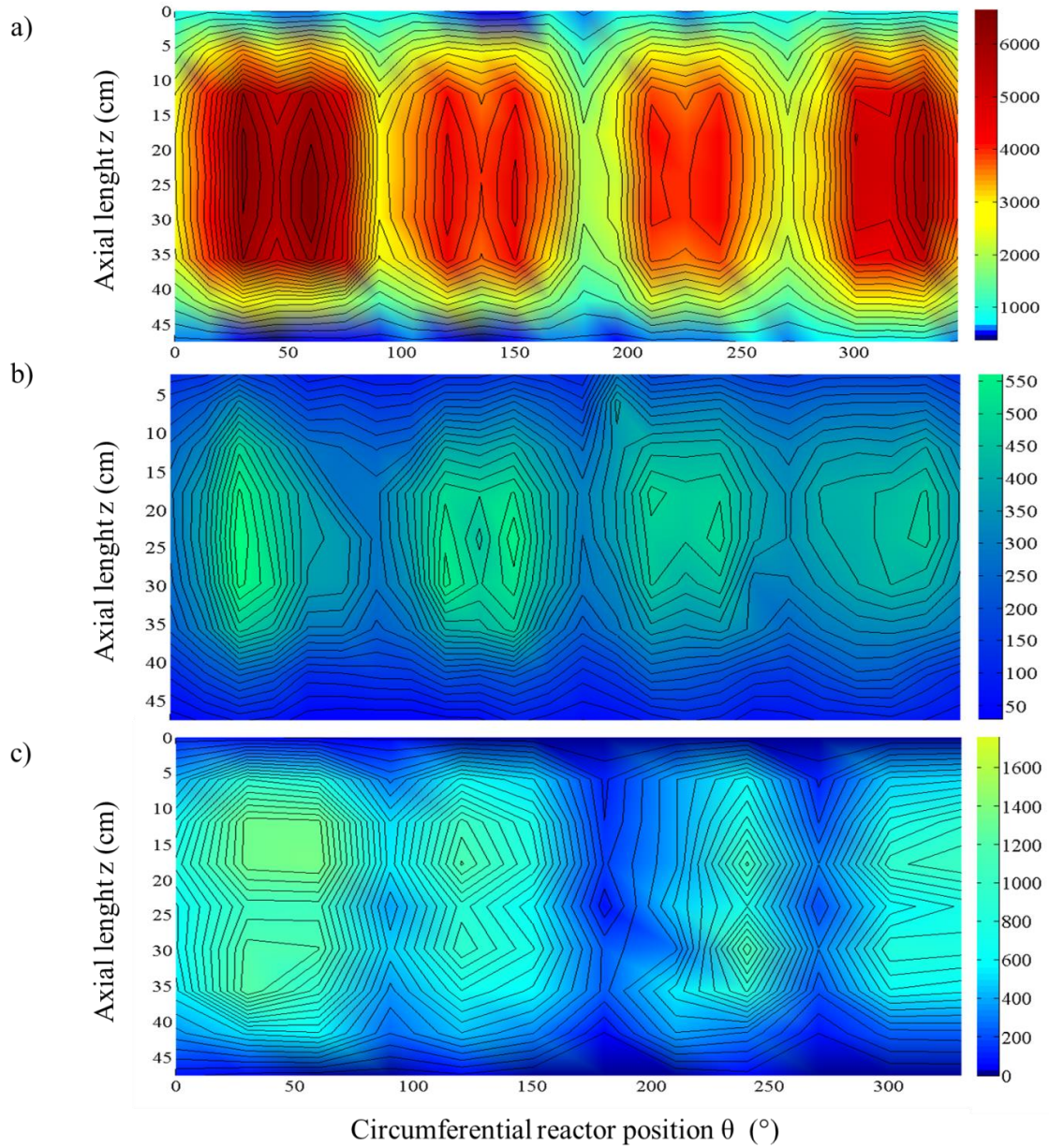


Figure 24: Color Mapping of the Radiation Field Distribution ($\mu\text{W}/\text{cm}^2$) in the Photo-CREC-Air Reactor as Measured with a Solatell Spectoradiometer. a) Describes the incident radiation reaching the mesh, b) Describes the reflected radiation from the mesh surface and c) Describes the transmitted radiation traversing the mesh.

The overall photon rate, for any of the contribution terms in Eq. (4.2) was calculated using the following equation:

$$P = \frac{Q}{E_{av}} \quad (6.20)$$

where E_{av} represents the average energy per photon (J/photon) and Q stands for the total energy provided by near-UV lamps (J/s).

Furthermore, Q was calculated via the integration of the radiation distribution as shown in Figure 24 at various θ , z and λ coordinates. Thus, eq. (6.20) can be rewritten as follows:

$$P = \frac{\int_{\lambda_{min}}^{\lambda_{max}} \int_0^{2\pi} \int_0^{\infty} q(\theta, z, \lambda) r d\theta dz d\lambda}{E_{av}} \quad (6.21)$$

Table 8. Calculated Photon Flux and Irradiation for Three Locations (1%wt TiO₂-AAS-ASC): a) On the surface of the mesh (r =5.9 cm), b) Transmitted through the mesh (r= 5.25 cm) and c) Reflected by the mesh (7.7 cm).

	Integrated Measured Irradiation, Q/r (μW/cm)	Photon Flux, P (photon/s)
Reaching the surface (Q_{Irr} or P_{irr})	1.75E+05 ± 1.23+04	1.22E+19 ± 8.54+17
Transmitted though the mesh (Q_{trans} or P_{trans})	2.98E+04 ± 2.09+03	1.39E+18 ± 9.73+16
Reflected by the mesh (Q_{ref} or P_{ref})	2.72E+04 ± 1.90+03	9.96E+17 ± 6.97+16

Thus, the absorbed photons can be calculated using Eq. (4.2) as follows:

$$P_{abs} = P_{irr} - P_{trans} - P_{ref} = 9.85 \times 10^{18} \pm 8.6 \times 10^{17} \frac{\text{photon}}{s} \quad (6.22)$$

On the basis of the above, one can establish a η_{abs} factor for the Photo-CREC-Air Reactor of:

$$\eta_{abs} = \frac{P_{abs}}{P_{irr}} = 0.80 \text{ or } 80\% \quad (6.23)$$

Based on the evaluated η_{abs} , one can state that in the present Photo-CREC-Air Reactor design, this unit displays an encouraging efficiency of 80% of absorbed photons per irradiated photons reaching the photocatalyst surface.

6.4 Monte-Carlo Evaluation of the Irradiation Field

The experimental radiation data was modeled using a 3D Monte Carlo Ray Tracing method (MCRT). This method considers: i) air to be a radiation transparent media, ii) reactor walls are considered grey surfaces while reflectors do specularly reflect radiation, and iii) the supported photocatalyst allows diffuse radiation and reflection on the vertical and horizontal cylindrical wire forming the mesh.

In order to incorporate these considerations, the Monte Carlo method uses a multi-scale approach, namely i) the photoreactor scale, ii) the mesh support scale and ii) the photocatalyst layer scale. This model was successfully applied already to slurry reactor radiation fields (Valadés-Pelayo, Guayaquil Sosa, Serrano, & de Lasa, 2015a, 2015b; Valadés-Pelayo, Moreira del Rio, Solano-Flores, Serrano, & de Lasa, 2014; Valades-Pelayo, Moreira, Serrano, & de Lasa, 2014).

Calculations start by selecting the location of emission from the lamp surface. The direction of the emission is sampled from a Lambertian distribution, given that the UV-lamp directional emission profile is known to be diffuse. Reflection through the photoreactor reflectors is accounted for by considering specularly reflecting planes.

Based on the fact that reactor geometry is periodic, only one-eighth of the reactor is rigorously modeled and periodic (100% specularly reflecting) boundary conditions are imposed at each end.

At the photoreactor scale, reactor walls are modeled as being absorbing, specular and reflecting surfaces while the photocatalyst mesh support is considered as a cylindrical surface. When a photon interacts with the mesh surface, the properties of the resultant photon are established based on the support mesh scale model, with the following being considered: i) transmission through the mesh holes, ii) absorption by the mesh surface or iii) diffuse reflection. At the mesh support, the mesh geometry is assumed to be comprised of vertically and horizontally aligned, diffuse reflecting cylinders. Within this calculation, the photon position is randomly adjusted and photon-mesh interaction is selected based on whether the photon goes through the mesh or not. This allows one to realistically model the probability of a photon going through the mesh at different incidence angles. Moreover, given that multiple photon-mesh interactions are possible, transmission through the mesh and reflection can be tuned based on the mesh geometric parameters. Finally, should the photons transmit through the photocatalyst-air interphase; the photocatalyst layer scale model is then accounted.

One should notice that the model employed at the photocatalyst layer scale, is a partial analytical model obtained by simplifying the radiative transfer equation (Appendix H). This simplification assumes that the irradiance field can be adequately described by considering that radiation can only travel in two directions. This model derivation uses a boundary condition determined by the above described Monte Carlo method, namely the absorbed radiation at each location per unit surface area of photocatalyst layer, presented in Fig. 25 (Absorbed).

Figure 25 reports the model results and experimental data obtained from the Photo-CREC-Air compared to the incident, reflected and transmitted radiation. The data obtained with the model predicts the experimental data well with an average error for the incident, transmitted and reflected radiation of 1%, 15% and 20% respectively. This error might be the result of experimental error and assumptions of the model.

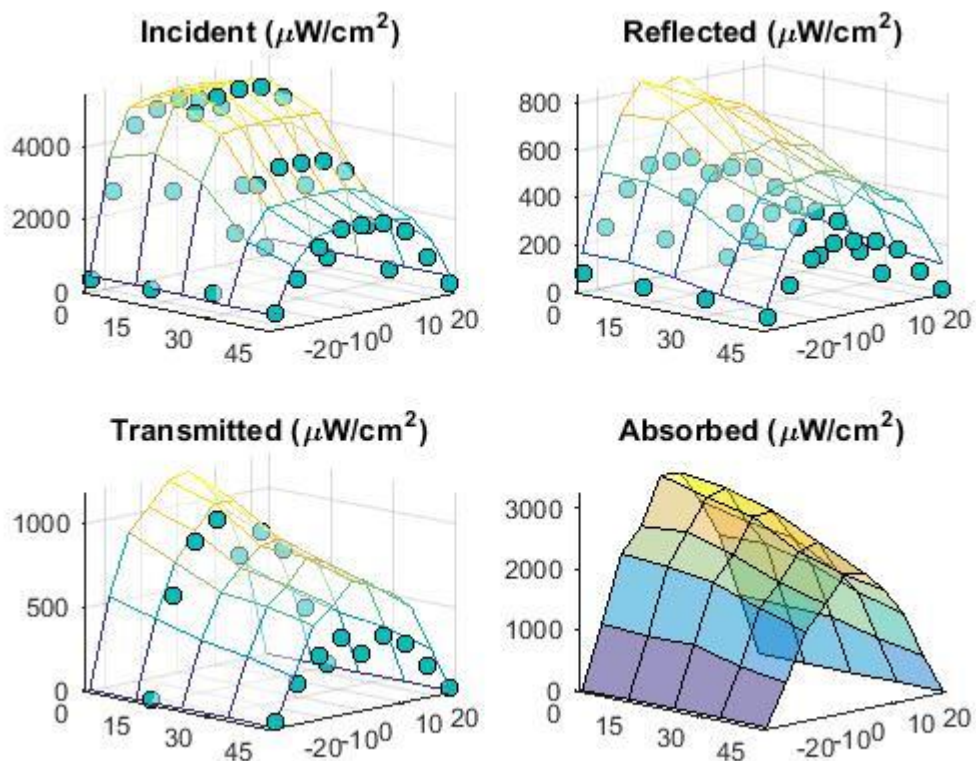


Figure 25: Experimental (green dots) and Modeled Irradiation (lines) for Incident, Transmitted, Reflected and Absorbed Radiation obtained with the MC model.

Table 9 reports the parameters considered for reactor surfaces according to the Markov Chain Monte Carlo structure, described above.

Table 9. Parameters considered for MCRT

Probability of absorption on reflector walls	10%
Probability of absorption on reflective surface	75%
Probability of quartz glass absorption	2%
Absorbance of the supported catalyst	100%
Absorbance of the support	100%
Film thickness (microns)	190
UV Lamps efficiency	14%

6.5 Photochemical Thermodynamic Efficiency Factor

While the QY definition is valuable, it does not reflect the extent of energy utilization in photocatalysis. In this respect, the semiconductor surface can be viewed as a system.

Thus, an overall energy balance can be considered as:

$$Q_{abs} - Q_{loss} - Q_{used} = \frac{dQ}{dt} \quad (6.24)$$

where Q_{abs} denotes the absorbed energy on the photocatalyst supplied by the photons with energy higher than 388 nm (J/min); Q_{loss} accounts for the energy released as heat (J/min); Q_{used} stands for the energy of formation of $\bullet OH$ radicals used for mineralization of the VOCs; and dQ/dt denotes the accumulation of energy in the system. Figure 26 describes such an energy balance.

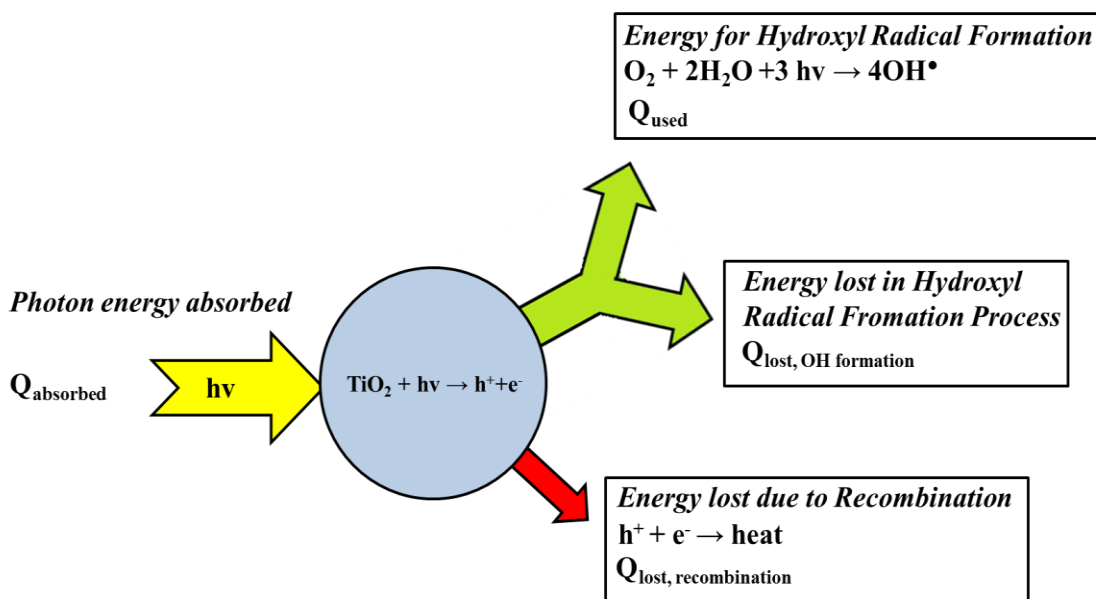


Figure 26. Schematics of the Energy Balance on the Photocatalyst Surface.

The accumulation term in Eq. (6.24) can be considered as negligible once the photocatalytic reactor reaches the steady state temperature. Therefore, Eq. (6.24) can be simplified as:

$$\frac{Q_{lost,recombination}}{Q_{absorbed}} + \frac{Q_{lost,OH\ formation}}{Q_{absorbed}} + \frac{Q_{used}}{Q_{absorbed}} = 1 \quad (6.25)$$

One should notice that when $Q_{lost,recombination}/Q_{absorbed} \rightarrow 0$, the term $Q_{used}/Q_{absorbed} + Q_{lost,OH,formation}/Q_{abs}$, reaches the value of one. It is in this situation that one would like to operate a photocatalytic reactor:

$$\frac{Q_{lost,OH\ formation}}{Q_{absorbed}} + \frac{Q_{used}}{Q_{absorbed}} = 1 \quad (6.26)$$

Under these conditions, the energy efficiency in a photocatalytic reactor will be intrinsically determined by the $Q_{used}/Q_{absorbed}$ ratio, with $Q_{lost,OH,formation}/Q_{absorbed}$ representing the energy fraction always dissipated as heat in the hydroxyl radical formation process.

This $Q_{used}/Q_{absorbed}$ efficiency factor term was designated as the *PTEF* or Photochemical Thermodynamic Efficiency Factor by Serrano and de Lasa (Serrano & de Lasa, 1997). More specifically, the *PTEF* is the enthalpy invested in the formation of consumed $\bullet OH$ radicals over the enthalpy content of the absorbed photons as follows:

$$PTEF = \frac{Q_{used}}{Q_{absorbed}} = \frac{-r_{\bullet OH} \Delta H_{\bullet OH} A_{irr}}{Q_{absorbed}} \quad (6.27)$$

where $r_{\bullet OH,T}$ accounts for the reaction rate of hydroxyl radical consumption (mole/min-cm²), A_{irr} denotes the irradiated area (cm²) and $\Delta H_{\bullet OH}$ stands for the enthalpy of hydroxyl radical formation (J/mole).

The *PTEF* can be alternatively expressed as:

$$PTEF = QY\eta_{\bullet OH} \quad (6.28)$$

where $\eta_{\bullet OH}$ is the fraction of photon energy used in forming a $\bullet OH$ radical, given by:

$$\eta_{\bullet OH} = \frac{\Delta H_{OH\bullet}}{E_{av}} \quad (6.29)$$

where E_{av} accounts for the average energy per photon in J/mol-photon.

However, critical to this definition is the careful establishment of the enthalpy of $\bullet OH$ radical formation. To accomplish this, one can consider the following equations:



where S refers to an adsorption site. These three steps can be represented in an enthalpy-state diagram as reported in Figure 27. In this diagram, one can account for the enthalpy content at the initial *Chemical State 1* considering both oxygen and water in the gas phase.

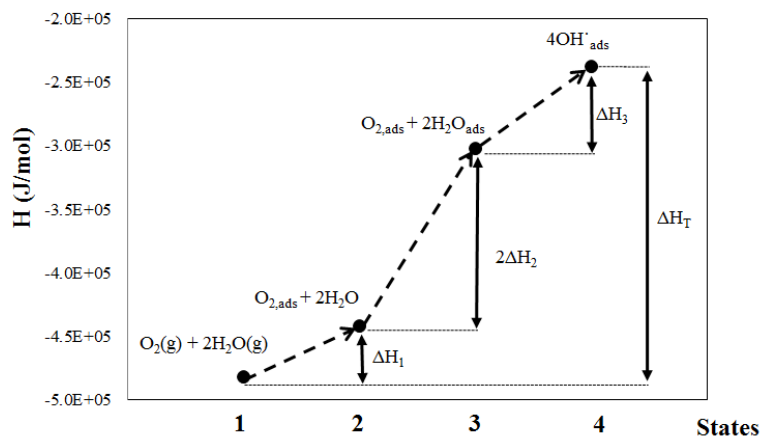
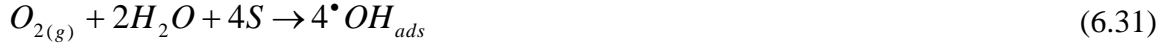


Figure 27. Schematic Description of Enthalpy States with Assumed Hypothetical Intermediate States (Hypothetical path). *Chemical State 1*: Formation of $O_2(g)+H_2O(g)$, *Chemical State 2*: Adsorption of O_2 . *Chemical State 3*: Adsorption of Water. *Chemical State 4*: Formation of Adsorbed Hydroxyl Radicals.

One could add these three steps, with this yielding the following:



Furthermore, the addition of the enthalpies corresponding to the individual equations (6.30a), (6.30b) and (6.30c) as described in Appendix G, yields the following:

$$\Delta H_T = 4\Delta H_{f,OH_{ads}}^\circ - \Delta H_{f,O_2(g)}^\circ - 2\Delta H_{f,H_2O(g)}^\circ \quad (6.32)$$

Moreover, expressing Eq. (6.32) on the basis of moles of $\bullet OH$ formed, yields the following:

$$\Delta H_{OH^\bullet} = \frac{\Delta H_T}{4} = \Delta H_{f,OH_{ads}}^\circ - \frac{1}{4}\Delta H_{f,O_2(g)}^\circ - \frac{1}{2}\Delta H_{f,H_2O(g)}^\circ \quad (6.33)$$

Considering the value of the formation enthalpies and the evaluated $\Delta H_{f,OH_{ads}}^\circ$ this results in:

$$\Delta H_{OH^\bullet} = -59,324 \text{ J/mol} - \frac{1}{2}[-241,820 \text{ J/mol}] = 61,586 \text{ J/mol} \quad (6.34)$$

One should notice that the assigned value for $\Delta H_{f,OH_{ads}}^\circ$ in the present study is -59,324 J/mole. This value differs from the previous one reported by [Garcia Hernandez et al. \(2010\)](#). A reassessment of $\Delta H_{f,OH_{ads}}^\circ$ is required for an accurate estimation of the *PTEF*.

As a result, with the ΔH_{OH^\bullet} of the present study, an η_{OH} as per Eq. (6.29), yields the following:

$$\eta_{OH^\bullet} = \frac{61,586 \text{ J/mol } OH^\bullet}{340,063 \text{ J/mol photon}} = 0.18 \frac{\text{mol photon}}{\text{mol } OH^\bullet} \quad (6.35)$$

On the basis of the above, and considering the QY_{max} , one can establish a $PTEF_{max}$ as follows:

$$PTEF_{\max} = QY_{\max} \eta_{\bullet OH} \quad (6.36)$$

Thus, the $PTEF_{\max}$ represents the highest possible energy efficiency that one can find in a photocatalytic reactor for air treatment and can be assessed as:

$$PTEF_{\max} = 0.249$$

Similarly, as for the overall Quantum Yields, one can define the following:

$$PTEF_{app} = PTEF \Gamma_{abs} \quad (6.37)$$

where the $PTEF$ represents the fraction of photon energy used to form the $\bullet OH$ consumed and Γ_{abs} denotes the fraction of irradiated energy absorbed by the photocatalyst.

Eq. (6.37) has the significant value of decoupling the energy efficiencies from: a) the intrinsic photocatalyst energy used as given by the $PTEF$, and b) the photo reactor irradiation absorption as considered by Γ_{abs} . Furthermore, and considering that there is no preferential absorption of photons on the wavelength range 310-385 nm, Eq. (6.37) becomes:

$$PTEF_{app} = PTEF \eta_{abs} \quad (6.38)$$

One can anticipate that this simplification is adequate given the polychromatic near-UV beam of the present study which has a limited wavelength variation.

In addition, and as described for QY_{app} , the practical use of Eq. (6.36) is of paramount importance for decoupling the energy efficiencies belonging to the photocatalyst and to the photoreactor for air treatment.

6.6 Conclusions

- a) Quantum Yields (QY) and Photochemical Thermodynamic Efficiency Factors (PTEF) in photoreactors for air treatment have to be established on the basis of a carefully determined experimentally-theoretically based methodology.
- b) This calculation has to be based on the hydroxyl radical consumption instead of on molecules photoconverted.
- c) The hydroxyl radical consumption has to consider every oxidation step for the photodegradation of acetone and acetaldehyde.
- d) This methodology has to involve macroscopic balances with the evaluation of irradiated photons, reflected photons and transmitted photon fluxes. This leads to a careful quantification of photons absorbed.
- e) The estimation of the PTEF has to include the evaluation of hydroxyl radical enthalpy using a hypothetical path in between states.

Chapter 7

7 Results and Discussion: Effect of TiO₂ loading and photon utilization on TiO₂-SC and TiO₂-AAS-ASC

This chapter describes the photoactivity evaluation of TiO₂-SC and TiO₂-AAS-ASC meshes using different TiO₂ loadings and acetone initial concentrations (25-50 μmole/L). This allows Quantum Efficiency evaluations (QYs) based on absorbed photons and hydroxyl radical consumed.

On the basis of the QYs an optimum photoactivity and photon utilization was achieved. In addition, a new proposed definition of Quantum Yield per weight of TiO₂ establishes the efficiency of the photocatalyst utilization with both meshes.

7.1 Effect of the TiO₂ Loading

The prepared TiO₂-SC and TiO₂-AAS-ASC meshes were evaluated in terms of photocatalytic activity for the degradation of acetone in the Photo-CREC-Air Reactor. Figure 28 reports the effect of the semiconductor loading on the initial reaction rate per irradiated area.

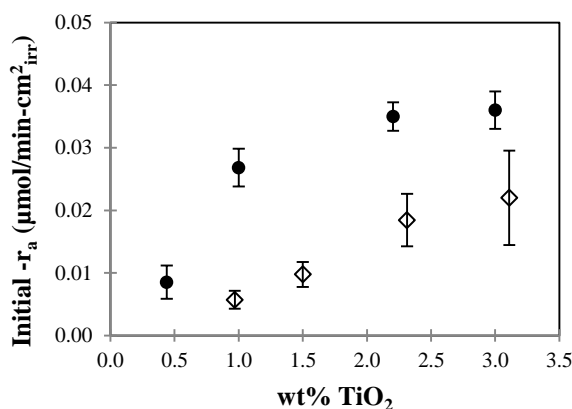


Figure 28: Effect of the TiO₂ Loading on the Initial Reaction Rate of Acetone per Mesh Irradiated Area when Using the TiO₂-SC (empty diamonds) and the TiO₂-AAS-ASC (solid circles). Reported data points and standard deviations included at least 4 repeats of independent experiments.

An initial acetone concentration of 25 $\mu\text{mol/L}$ was considered for these experiments. The data reported in Figure 28 was the result of at least 4 repeats developed per operating condition. Figure 28 reports an increase in the initial acetone conversion rate with the TiO_2 loading. This is the case for both $\text{TiO}_2\text{-SC}$ and $\text{TiO}_2\text{-AAS-ASC}$. In this respect, one can observe that the initial photoconversion rate does not increase significantly once 2.5wt% and 1wt% of TiO_2 loading are respectively reached for $\text{TiO}_2\text{-SC}$ and $\text{TiO}_2\text{-AAS-ASC}$. Thus, one can conclude that the $\text{TiO}_2\text{-AAS-ASC}$ displays a leveling of the rate with 3 times less TiO_2 than the one required for $\text{TiO}_2\text{-SC}$. Furthermore, the $\text{TiO}_2\text{-AAS-ASC}$ appears to offer a more reliable alternative with initial photoconversion rates showing smaller standard deviations for repeats (5-10%). These standard deviations for the $\text{TiO}_2\text{-SC}$ were in the 22% to 34% range.

7.2 Effect of the Initial Acetone Concentration

Table 10 also reports the initial photoconversion rates for acetone. In this table, rates are based on the unit TiO_2 weight. One can observe that the $\text{TiO}_2\text{-AAS-ASC}$ yields a r_{acetone} rate of acetone photoconversion close to 3 times that obtained with the $\text{TiO}_2\text{-SC}$. This is consistently true for all the runs developed using the $\text{TiO}_2\text{-AAS-ASC}$, with initial acetone concentrations in the 25-50 $\mu\text{mol/L}$ range.

Table 10. Initial Acetone Photoconversion Rates per Unit Photocatalyst Weight in the Photo-CREC-Air Reactor using $\text{TiO}_2\text{-SC}$ and $\text{TiO}_2\text{-AAS-ASC}$. Three initial acetone concentrations were considered: 25, 37 and 50 $\mu\text{mol/L}$.

Acetone Initial Concentration ($\mu\text{mol/L}$)	Initial r_{acetone} ($\mu\text{mol/g-min}$)	
	$\text{TiO}_2\text{-SC}$	$\text{TiO}_2\text{-AAS-ASC}$
25	$4.3 \pm 12\%$	$13 \pm 17\%$
37	$5.4 \pm 12\%$	$16 \pm 12\%$
50	$5.9 \pm 8\%$	$18 \pm 22\%$

Regarding the reported effects of the coated mesh on acetone photoconversion, one can attest that a higher photoactivity is achieved when using the $\text{TiO}_2\text{-AAS-ASC}$ given: a) its

reduced particle agglomeration size in the coated layer, b) its minimized particle agglomeration in the wire junctions. These favorable particle dispersions lead to better exposure of the TiO₂ particles to incident photons.

One can notice that these results are consistent with Figures 18 and 19, for the TiO₂-AAS-ASC mesh. As stated, in this case, one can observe a more uniform and reproducible coating. As reported in Figure 28 and Figure 20, when the TiO₂ loading reaches 1%wt TiO₂, the thickness of this coating is 8 μm on average. This can be considered to be the required thickness for complete photon absorption. In this respect, Peral and Ollis (Peral & Ollis, 1992) reported a 99% near-UV light absorption within a TiO₂ anatase layer of 4.5 μm. Ibrahim and de Lasa (Ibrahim & de Lasa, 2002) also showed the highest photocatalytic activity when the thickness of Degussa P25 layer on a fiberglass support reached 5.4 μm. Jacoby et al. (Jacoby et al., 1995) also suggested that a 2 μm TiO₂ thick layer participates in the photoreaction only. Thus, it is concluded that the TiO₂-AAS-ASC of the present study provides a homogeneous and stable coating. This coating has a thickness close to the “optimum” one required for complete photon absorption and maximum photoconversion rates per unit TiO₂ weight.

Figure 29 and Figure 30 report the acetone and CO₂ concentrations formed at different initial conditions. The TiO₂ coating used in all these cases was 1wt% TiO₂ for the TiO₂-AAS-ASC. One can notice a complete mineralization of the acetone after 56 to 100 minutes.

Furthermore, Figures 31 and 32 display the acetone and CO₂ concentration changes with irradiation time using a 3wt% TiO₂ on the TiO₂-SC. Initial concentration values reported in Figures 31 and 32 correspond to initial acetone concentration in the gas phase. Once again, one can observe that the required irradiation times for complete mineralization using TiO₂-SC are in the 56-100 minute range.

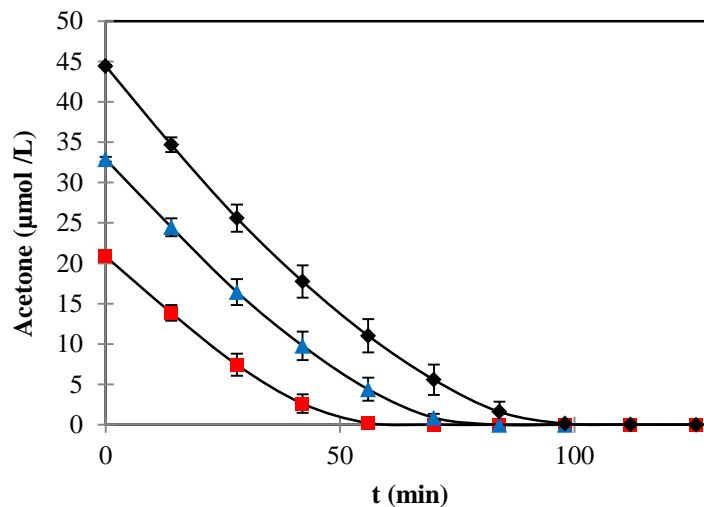


Figure 29: Changes of Acetone Concentration with Irradiation Time Using the 1wt% TiO₂-AAS-ASC Mesh. Three different initial concentrations were considered: a) 25 (□), b) 37 (Δ) and c) 50 µmol/L (◇). Reported data points and standard deviations included at least 4 repeats of independent experiments.

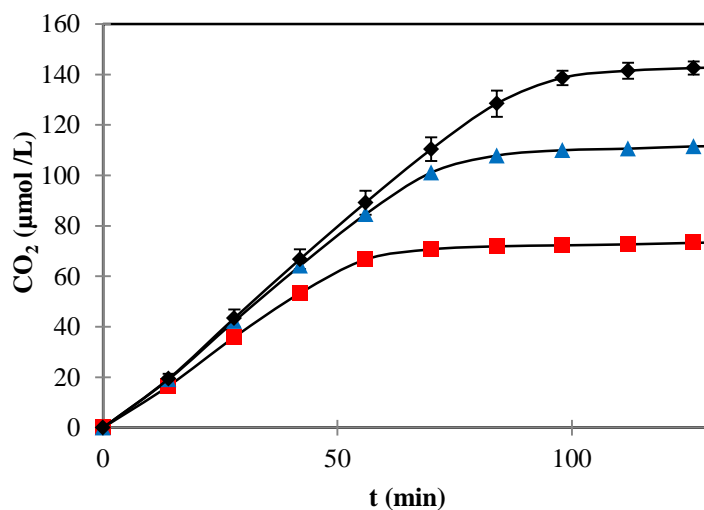


Figure 30: Changes of CO₂ Production for Acetone Photodegradation using the 1wt% TiO₂-AAS-ASC Mesh. Three different initial acetone concentrations were considered: a) 25 (□), b) 37 (Δ) and c) 50 µmol/L (◇). Reported data points and standard deviations included at least 4 repeats of independent experiments.

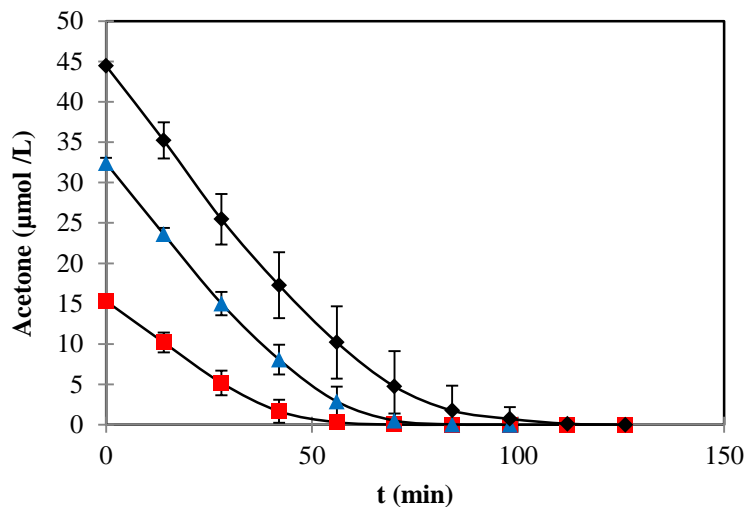


Figure 31: Changes of Acetone Concentration with Irradiation Time using the 3% TiO₂-SC Mesh. Three different initial concentrations were considered: a) 25 (□), b) 37 (Δ) and c) 50 µmol/L (◇). Reported data points and standard deviations included at least 4 repeats of independent experiments.

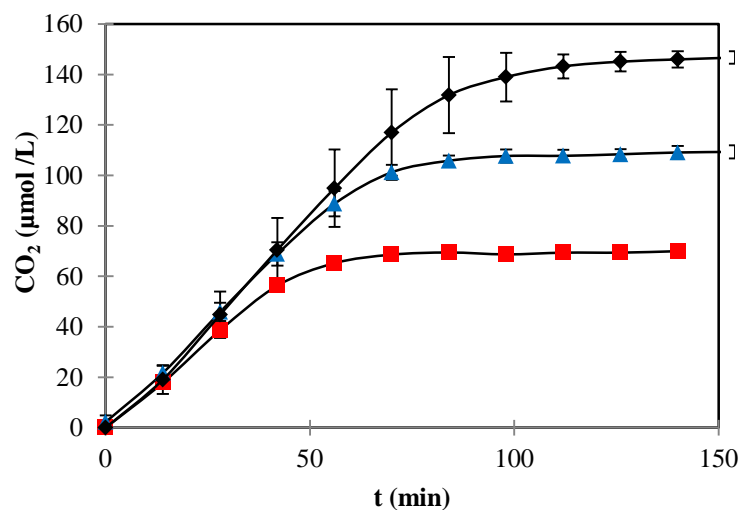


Figure 32: Changes of CO₂ Production with Acetone Photodegradation Using the 3wt% TiO₂-SC Mesh. Three different initial acetone concentrations were considered: a) 25 (□), b) 37 (Δ) and c) 50 µmole/L(◇). Reported data points and standard deviations included at least 4 repeats of independent experiments.

However, an important observation in Figures 29 to 32, is that there is a higher variation of both acetone and CO₂ measured concentrations when using the TiO₂-SC. This is particularly apparent for a 50 μmol/l initial acetone concentration. These higher observed changes can be assigned to a less reproducible TiO₂-SC performance while compared to the TiO₂-AAS-ASC. One can notice that this is true in spite of the fact that the TiO₂-AAS-ASC requires 3 times less TiO₂ than the TiO₂-SC.

7.3 Quantum Yields for TiO₂-SC and TiO₂-AAS-ASC

On the basis of the procedure discussed in Section 4.4 and Section 6.1, Quantum Yields were calculated for the acetone photodegradation in the Photo-CREC-Air Reactor at different initial concentrations. Figure 33 compares the QYs obtained for the acetone photodegradation using the TiO₂-SC and TiO₂-AAS-ASC meshes.

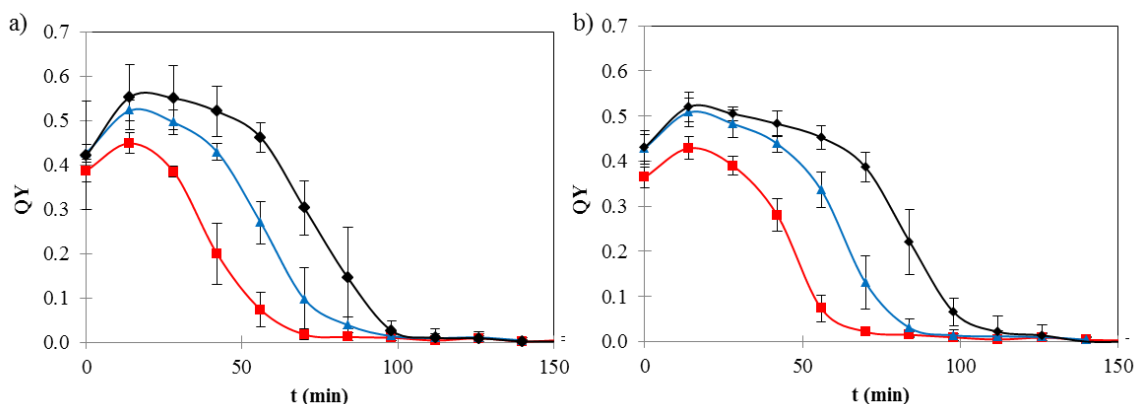


Figure 33: Calculated QYs during the Photocatalytic Degradation of Acetone Using Immobilized: a) 3% TiO₂-SC and b) 1% TiO₂-AAS-ASC. Three initial concentrations were considered: 25 (red squares), 37 (blue triangles) and 50 μmol/L (black diamonds).

Figure 33 shows that for both TiO₂ immobilized meshes, the Quantum Yields consistently reach a 50-60% maximum level. QYs increase first and decrease progressively later with irradiation time. It is assumed that the available •OH radicals first react with acetone molecules. Some of these photoreaction steps lead to complete mineralization while others lead to the formation of intermediates such as acetaldehyde.

Thus, the photocatalytic conversion of acetone in air involves both complete acetone mineralization (CO₂ formation) and partial acetone oxidation to acetaldehyde. As a result, the first stages of photoconversion are influenced by $\bullet OH$ oxidizing both the acetone and the more reactive acetaldehyde. This explains the modest initial increase in QYs. Following this irradiation period, QYs decrease progressively. This is given the simultaneous reduction of both acetone and acetaldehyde concentrations, with all this leading to the complete mineralization of organic species.

One can mention that the observed changes in chemical species with irradiation time are the result of the so-called “series-parallel” reaction network (Ortiz-Gomez et al., 2007). This is the case given the unavoidable photon density differences in various TiO₂ immobilized mesh locations in the Photo-CREC-Air when using the TiO₂-SC and TiO₂-AAS-ASC. One should also notice that the data reported in the present study, is also valuable in order to clarify the magnitude of QY values previously reported by our research group as exceeding 100% (Garcia-Hernandez et al., 2012). It is proven in the present study, that the QYs for TiO₂-SC and TiO₂-AAS-ASC meshes in the Photo-CREC-Air Reactor while showing excellent performance remain in the 55-56% range.

Furthermore, and to complete the review on quantum efficiencies, a Quantum Efficiency (η_w) factor based on the unit weight of the photocatalyst is considered:

$$\eta_w = \frac{QY}{W} \quad (7.1)$$

Figure 34 reports the η_w results as functions of the irradiation time for three initial acetone concentrations.

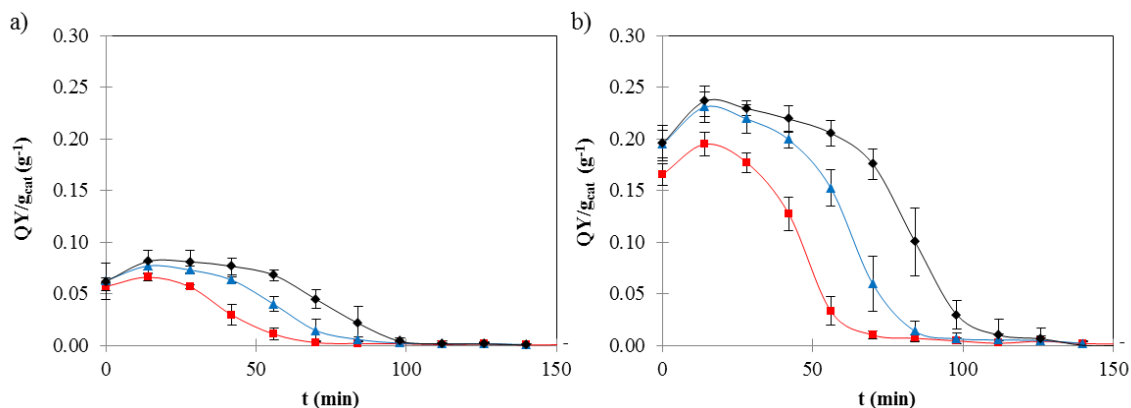


Figure 34: Calculated η_w during the Photocatalytic Degradation of Acetone Using Immobilized: a) 1% TiO₂-SC (2.2g) and b) 3% TiO₂-AAS-ASC (6.8 g). Three initial concentrations were considered: 25 $\mu\text{mol/L}$ (red squares), 37 $\mu\text{mol/L}$ (blue triangles) and 50 $\mu\text{mol/L}$ (black diamonds).

It can be observed that the η_w reaches a maximum value of 0.08 1/g when using the TiO₂-SC method, while this value is 0.24 1/g or three times larger when employing the TiO₂-AAS-ASC technique. This demonstrates that the TiO₂-AAS-ASC provides a mesh with more efficient photocatalyst utilization.

Figures 35a and 35b schematize the utilization of photons when using both TiO₂-AAS-ASC and TiO₂-SC meshes. One can see that the more homogeneous TiO₂ distribution and limited particle agglomeration of the TiO₂-AAS-ASC mesh allows for limited photocatalyst particle exposed areas with higher radiation density. Therefore, and as a result, one can explain the higher rates of $\bullet\text{OH}$ radicals available per unit photocatalyst weight which are observed when using the TiO₂-AAS-ASC method.

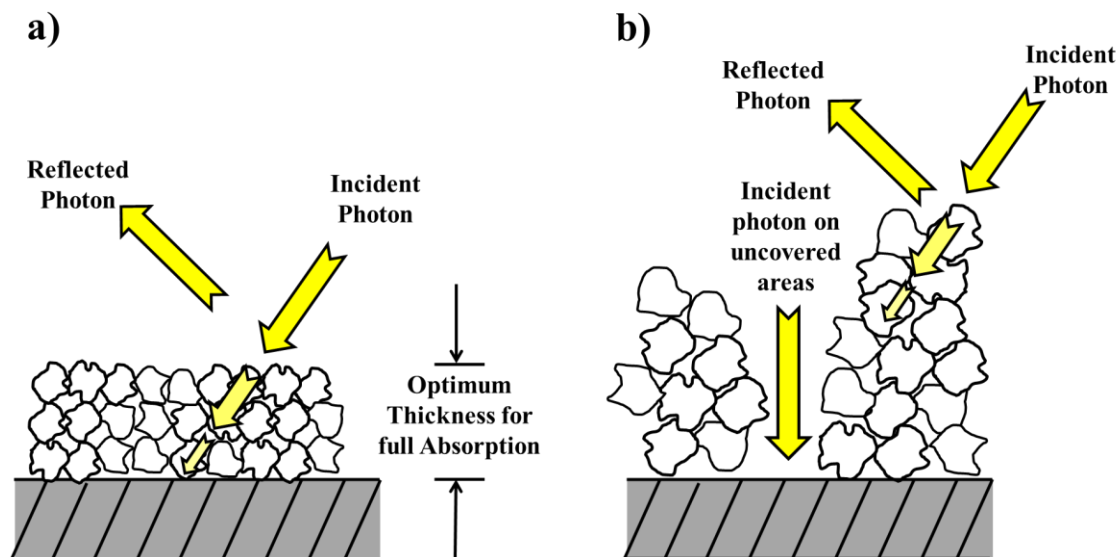


Figure 35: Schematic Representation of the Particle Agglomeration and the Utilization of Photons on the TiO₂ Coatings: a) TiO₂-AAS-ASC and b) TiO₂-SC.

Thus, one can see that once the 6-10 μm coating thickness is reached, a close to complete utilization of irradiated photons is accomplished. An extra TiO₂ thickness on the mesh as in TiO₂-SC, does not contribute to photocatalytic conversion.

Furthermore, one can also argue that the η_w obtained in the present study compares favorably with the so-called optimum η_w calculated as follows:

$$\eta_{w, optimum} = \frac{QY_{max}}{A_c L_{opt} \rho_{TiO_2} (1 - \varepsilon)} = 0.4 g^{-1} \quad (7.2)$$

where the QY_{max} is the maximum Quantum Yield reached in the acetone photodegradation; A_c accounts for the area of the TiO₂ coated mesh (cm^2); L_{opt} represents the optimum thickness for maximum photon utilization (0.0008 cm); ρ_{TiO_2} is the density of the TiO₂ (g/cm^3) and ε stands for the coating porosity (regular porosity of TiO₂ 0.5).

The optimum η_w corresponds to an ideal η_w value where the reaction rate of acetone is the highest and the thickness of the film is constant in every point of the mesh. In the specific case of a QY of 0.52, as shown in Figure 33, this yields an optimum η_w which equals 0.4

g^{-1} . This value is close to the best η_w of 0.24 g^{-1} , which is observed experimentally and reported in Figure 34.

As a result, one can conclude that the TiO_2 -AAS-ASC leads to a TiO_2 immobilized coating with a performance close to the expected optimum values.

7.4 Physically Based Model for the Effect of TiO_2 Loading

The photon absorption on the TiO_2 photocatalyst film of the TiO_2 -AAS-ASC at different photocatalyst loadings can be studied using the Radiative Transfer Equation. The Radiative Transfer Equation for non-relativistic calculations at low temperatures is:

$$\frac{dI(s, \Omega)}{ds} = -\kappa I(s, \Omega) - \sigma I(s, \Omega) + \frac{\sigma}{4\pi} \int_0^{4\pi} I(s, \Omega') \Phi(\Omega, \Omega') d\Omega' \quad (7.3)$$

where s and Ω represent position and solid angle respectively, I accounts for the spectral specific intensity of radiation ($\text{einsteins}/\text{m}^2\text{-s-sr}$), κ represents the absorption coefficient (m^{-1}), σ is the scattering coefficient (m^{-1}), and Φ stands for the phase function for scattering phenomena.

Eq. 7.3 represents a photon flux balance where the radiation can be absorbed, transmitted or scattered by the particle. This equation calculates the photon fluxes through the film and therefore the photoactivity in every depth in the film (refer to Section 6.4). This model is very relevant for photoreactor scale-up to obtain the optimum thickness and optimum photocatalyst loading. Also it is useful for the evaluation of photon density and their effect on the degree of VOC oxidation.

The model assumes that the radiation can travel in two directions leading to a system of two simultaneous equations that can be solved analytically for photon flux through the film. Moreover, in order to associate the photon flux with the photoactivity, a balance of hole-electron pairs is considered to evaluate the conversion of photon absorption to $\bullet\text{OH}$ radicals. This hole-electron pair balance was validated by [Valades-Pelayo \(2014\)](#) in slurry reactors for the photodegradation of oxalic acid and phenol. The complete solution of the model is described in Appendix I and J. Figure 36 reports the prediction of the

Radiative Transfer Equation for the effect of the photocatalyst loading of the TiO₂-AAS-ASC on the initial reaction rate of the photodegradation of 25 μmole/l of acetone.

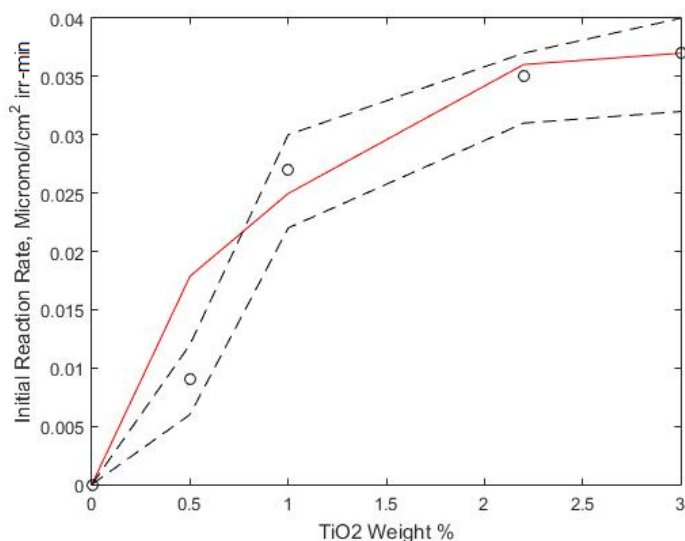


Figure 36: Influence of the TiO₂ Loading on the Initial Acetone Photodegradation rate in the Photo-CREC-Air Reactor Using a TiO₂-AAS-ASC Mesh. Empty circles represent experimental data. Upper and lower broken lines describe the upper and lower limits for experimental data. The red line reports the proposed model.

One can see that this physically based model is in agreement with the experimental data. It is important to mention that the considered model was not fitted to the experimental data and is fully predictive.

7.5 Conclusions

- The TiO₂-AAS-ASC coated mesh is successfully evaluated in a scaled up 55.1 L Photo-CREC-Air Reactor. This demonstrates its high photoactivity for the photoconversion of acetone in air.
- Quantum Yields (QYs) calculated in this unit, using consumed $\bullet OH$ radical groups and absorbed photons give 0.4-0.5 high QY performance values.
- Quantum Yields per unit weight of photocatalyst gives values three times larger for the TiO₂-AAS-ASC mesh than for the TiO₂-SCM mesh.

- d) The 6-10 μm thickness for a 1 wt% TiO_2 loading on a TiO_2 -AAS-ASC mesh allows complete absorption of photons. This optimum thickness is verified using a Monte Carlo method in order to estimate the absorption of photons as well as perform an electron-hole pair balance analysis.

Chapter 8

8 Results and Discussion: Energy Efficiency Limits in Photo-CREC-Air Reactors

This chapter reports the photocatalytic degradation of acetone and acetaldehyde for 50-324 $\mu\text{mole/L}$ high initial model pollutant concentrations using 1% $\text{TiO}_2\text{-AAS-ASC}$. Quantum Yields and Photochemical Thermodynamic Factor Efficiencies are evaluated under operating conditions close to adsorption site saturation. This allows one to obtain the “practical limits” of QYs and PTEFs and to establish an interpretation of energy efficiency factors in the context of reactivity and hydroxyl group consumption.

It is noticed from this analysis that the “Apparent” Quantum Yields (QY_{app}) depend on the combined effect of “intrinsic” QYs for the photocatalyst and the photon absorption efficiency in the photoreactor unit.

8.1 High Acetone and Acetaldehyde Concentrations

Figures 37 and 39 both show the concentration changes of acetone and acetaldehyde, respectively, with irradiation time. The respective CO_2 concentration changes are also reported. Quantum Yields for acetone and acetaldehyde degradation were calculated using the kinetic data described in Chapter 9 and the QY definition as per Eq. (6.6) of Chapter 6.

Furthermore, Figures 38 and 40 report the Quantum Yields for acetone and acetaldehyde, respectively, during irradiation time. One can notice that for acetaldehyde, there is a steady decrease of the QY. This result is attributed to the high reactivity of the acetaldehyde yielding CO_2 directly. On the other hand, acetone QY's display a different trend. They increase during the first 20 minutes, and then decrease steadily until reaching essentially zero values.

This behavior was attributed to the reaction network. Small concentrations of acetaldehyde (0-2 $\mu\text{mole/L}$) were found during the photodegradation of acetone. In addition, the photoconversion of acetaldehyde shows measurable intermediate species

(formaldehyde, formic acid and methanol) which are involved in the reaction path leading to mineralization. The observations of these intermediate compounds are in agreement with other publications on the photodegradation of acetone and acetaldehyde (Bianchi et al., 2014; Hou, Miyafuji, & Saka, 2006; Salvadores et al.).

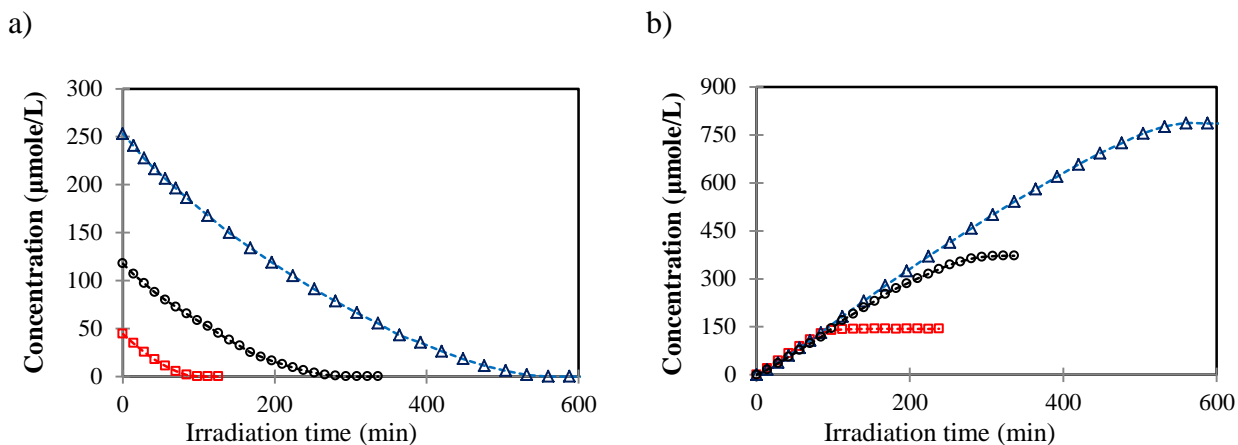


Figure 37: a) Acetone Concentration Changes and b) CO₂ Concentration Changes with Irradiation Time. Three different initial acetone concentrations were used: 50 (red □), 124 (black ○) and 247 μmole/L (blue Δ). Note: Typical standard deviations for repeats: 5%.

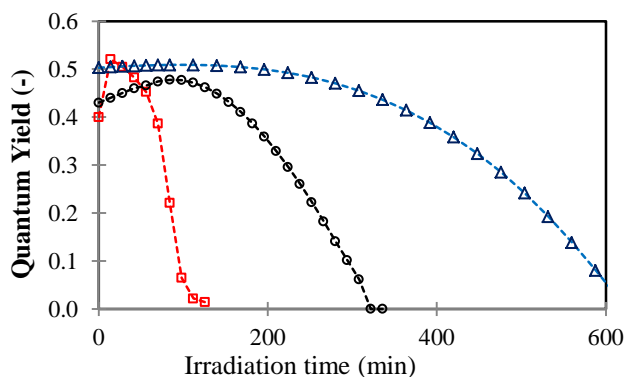


Figure 38: Quantum Yields for the Degradation of Acetone at various Irradiation Times. Three different initial acetone concentrations were considered: 50 (red □), 124 (black ○) and 247 μmole/L (blue Δ). Note: Typical standard deviations for repeats: 15%.

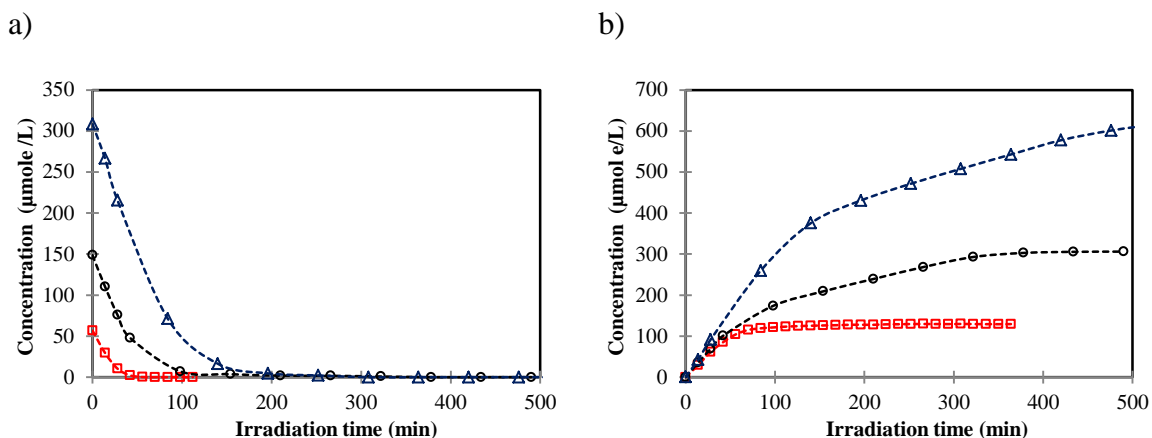


Figure 39: a) Acetaldehyde Concentration Changes and b) CO₂ Concentration Changes with Irradiation Time. Three different initial acetaldehyde concentrations were considered: 65 (red □), 162 (black ○) and 324 µmole/L (blue Δ). Note: Typical standard deviations for repeats: 5%.

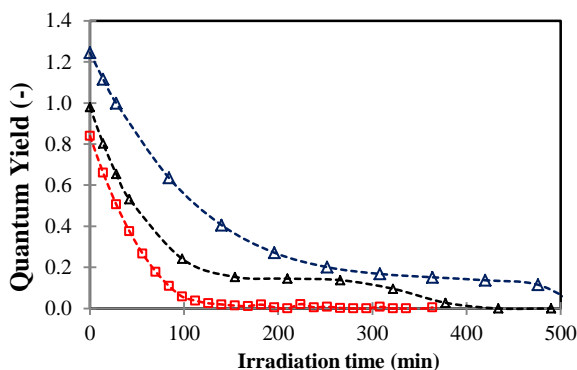


Figure 40: Quantum Yields for the Degradation of Acetaldehyde at various Irradiation Times. Three different initial acetaldehyde concentrations were considered: 65 (red □), 162 (black ○) and 324 µmole/L (blue Δ). Note: Typical standard deviations for repeats: 15%.

Interesting observations in this case, are the QY values for both acetone and acetaldehyde. In the case of acetone, high QYs in the 40 to 50% range were recorded. Furthermore, in the case of acetaldehyde, QYs as high as 124% were observed as shown in Figure 40.

One can also notice that the QY is a parameter that reflects the photonic efficiency at a particular irradiation time in the Photo-CREC-Air. QYs vary through the irradiation period with this being a function of the model pollutant concentration and molecule reactivity. Variations of QYs with organic molecule reactivity are shown using acetone and acetaldehyde. Thus, and in order to have a more representative efficiency parameter, an average QY (QY_{av}) can be defined.

QY_{av} describes the photons utilization efficiency for photoconverting organic molecules using hydroxyl radicals, during the 0 to t irradiation period as follows,

$$QY_{av} = \frac{\int_0^t r_{OH\cdot} dt}{\int_0^t P_{abs} dt} \quad (8.1)$$

Figure 41 reports the average QY or QY_{av} for the acetone (Figure 41a) and acetaldehyde (41b). One can, for instance, notice that at complete mineralization of acetone and acetaldehyde, the average QYs reach values between 0.13-0.26.

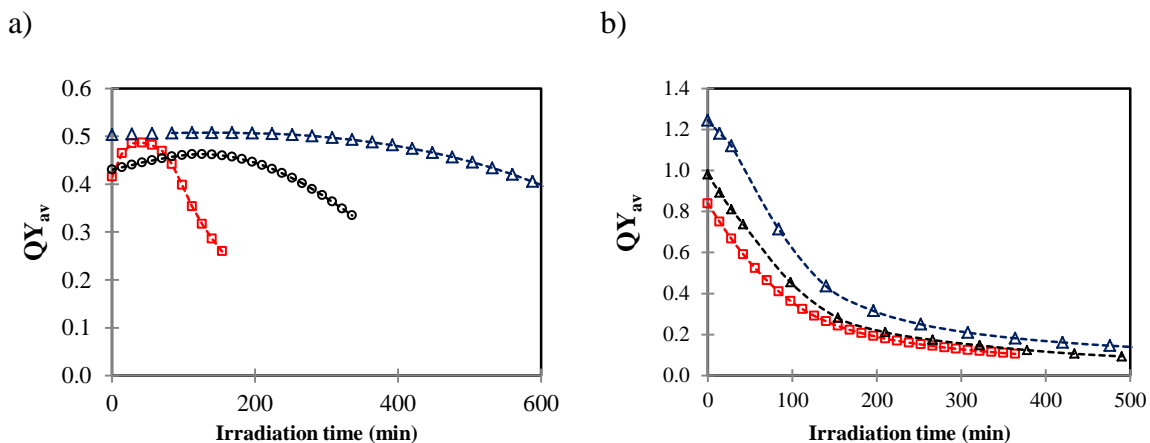


Figure 41: a) Average QY s for the photodegradation of acetone. Three different initial acetone concentrations were considered: 49.8 (red \square), 124 (black \circ) and 247 $\mu\text{mole/L}$ (blue Δ). b) Average QY s for the photodegradation of acetaldehyde. Three different initial acetaldehyde concentrations were considered: 65 (red \square), 162 (black \circ) and 324 $\mu\text{mole/L}$ (blue Δ). Typical standard deviations for repeats: 15%.

One should notice, that the QY_{av} provides a more representative and practical information of the photocatalytic reactor efficiency given it establish an average over an entire “ t ” irradiation period. Since the observed QYs of 124% for 324 $\mu\text{mole/L}$ initial acetaldehyde concentrations, are so close to the anticipated theoretically based QY_{max} values (refer to Appendix A), the following can be stated: a) One can design an immobilized TiO_2 photocatalyst, using the spray dried method with negligible recombination of h^+ sites and electrons, with essentially all electron-hole carriers contributing to the OH^\bullet formation, b) One can use the high observed QYs to validate possible reaction paths and proposed stoichiometric relations setting 133% upper limits for QYs .

8.2 Photochemical Thermodynamic Efficiency Factors

As stated in Section 6.5, the $PTEF$ is another very important parameter to assess photocatalytic reaction efficiency, given that it is based on energy conversion considerations. Figures 42a and 42b report the $PTEFs$ for the degradation of acetone and acetaldehyde, respectively.

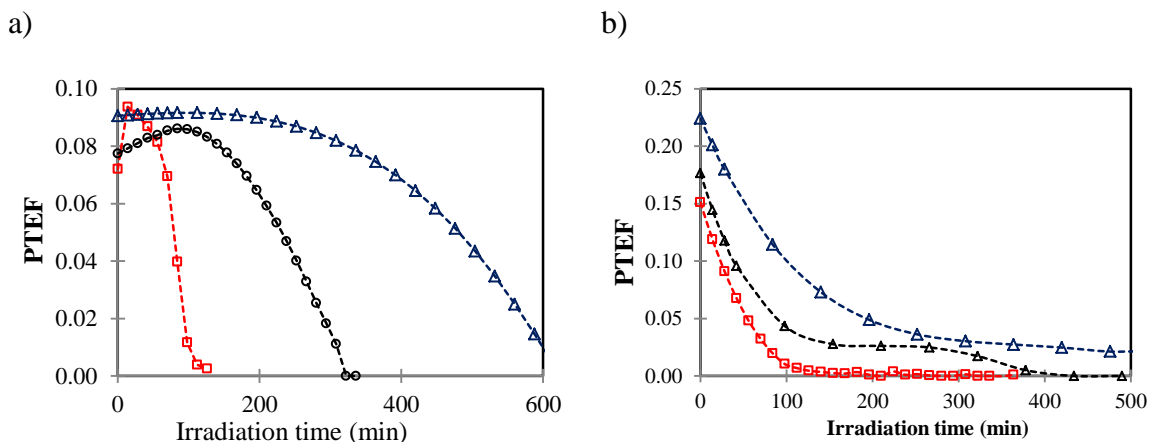


Figure 42: a) PTEFs (Photochemical Thermodynamic Efficiency Factor) for the photodegradation of acetone. Three different initial acetone concentrations were considered: 50 (red \square), 124 (black \circ) and 247 $\mu\text{mole/L}$ (blue Δ). b) PTEFs (Photochemical Thermodynamic Efficiency Factor) for the photodegradation of acetaldehyde. Three different initial acetaldehyde concentrations were considered:

65 (red □), 162 (black ○) and 324 μmole/L (blue Δ). Typical standard deviations for repeats: 15%.

One can observe in Figure 42a that the *PTEF* increases progressively up to 10% during the first irradiation period. This trend mirrors the changes in acetone concentration and the *QYs*. A similar observation can be drawn for acetaldehyde with the very important result that a maximum *PTEF* is obtained close to the 24% level. This *PTEF* value points towards achievable maximum *PTEFs* in the Photo-CREC-Air Reactor, near to the $PTEF_{max}$ as expected by thermodynamics (refer to Chapter 6). It is in all these respects, that one can notice the criticality of having, in this assessment, a correctly established value for ΔH_{OH} .

8.3 Practical Limits for *QYs* and *PTEFs*

Furthermore, Figure 43 reports the changes of both the *PTEFs* and *QYs*, defined at the initial conditions and this as a function of the initial acetone and acetaldehyde concentrations.

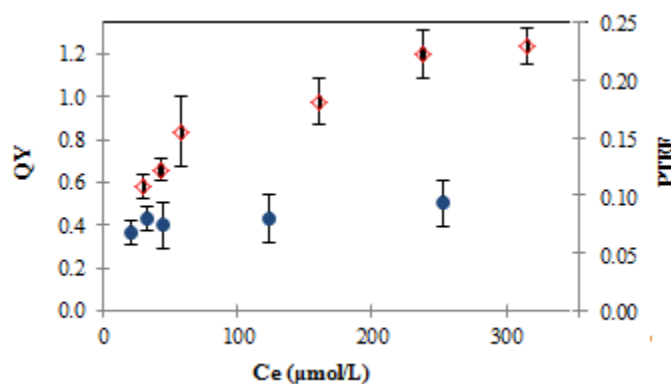


Figure 43: Changes in the Initial *PTEFs* and *QYs* with the Initial Concentrations of Acetone (blue ●) and Acetaldehyde (red ◇). Note. The right coordinate refers to the *PTEFs*, and the left coordinate refers to *QYs*.

One can observe in Figure 43 that *QYs* for both higher acetone and acetaldehyde initial concentrations, display increasing *QY* levels reaching maximum values. These observed maximum *QYs* are the combination of the following: a) A Langmuir-Hinshelwood photoconversion kinetics, yielding zero order OH^\bullet consumption rates above 100-150

$\mu\text{mole/L}$ initial concentrations, b) A fixed flux of absorbed photons. In the particular case of acetaldehyde, one can observe that both the QYs and $PTEFs$ are in the 124% and 23% range conforming closely to the expected maximum limits of 133% and 24% for $PTEFs$ and QYs . One can thus conclude that for a proper assessment of a given photocatalyst, one should consider model pollutants such as acetaldehyde, not limited by the reactivity of the organic molecule bonds with the formed OH^\bullet radicals. In addition, charge recombination is affected by the nature of the molecules. Some molecules can trap the holes more effectively than others thus leading to higher efficiencies (Palmisano, Scandura, et al., 2015; Zhang, Mohamed, Dillert, & Bahnemann, 2012).

Furthermore, it is also demonstrated in the present study, that for the spray dried immobilized TiO_2 using acetaldehyde, QYs and $PTEFs$ showed close to maximum utilization efficiency levels. On the other hand, one can also notice that 80% η_{abs} in the Photo-CREC-Air Reactor, leads to QY_{app} and $PTEF_{app}$ as follows:

$$QY_{app,max} = QY_{max} \eta_{abs} = 0.99 \quad (8.2)$$

$$PTEF_{app,max} = PTEF_{max} \eta_{abs} = 0.18 \quad (8.3)$$

On the basis of the above, one can argue that the Photo-CREC-Air Reactor design displays excellent QYs and $PTEFs$, with good apparent QY_{app} and $PTEF_{app}$ performances. This points to possible further enhancements in the area of η_{abs} photon absorption.

8.4 Conclusions

- a) QY and $PTEF$ efficiencies were evaluated using acetone and acetaldehyde photodegradation at conditions close to full site saturation (50-324 $\mu\text{mole/L}$).
- b) Calculated maximum QYs for acetaldehyde and acetone are 124% and 50%, respectively. The Quantum Yield is limited by both the reactivity of the organic molecule bonds with the formed OH^\bullet radicals and the ability of the molecules to trap the holes more effectively.

- c) Calculated QYs and $PTEFs$ for acetaldehyde are in the 40-124% and in the 10-23% ranges, respectively.
- d) Observed maximum $PTEFs$ and QYs for acetaldehyde at initial concentrations larger than 110-150 $\mu\text{mole/L}$ are very close to the expected 24.7% and 133% maximum values, respectively. This demonstrates the high degree of photon energy utilization when using the prepared spray TiO_2 immobilized photocatalyst.
- e) The high Quantum Yields close to 133%, can be considered an experimental validation of the proposed reaction path and stoichiometry for the calculation of the proposed upper limits for QYs .
- f) The macroscopic energy balances developed in the Photo-CREC-Air Reactor allow decoupling the calculation of the QYs and $PTEFs$ from the η_{abs} absorption efficiency of irradiated photons.
- g) The separately evaluated QYs and η_{abs} , provide valuable insights into the performance of the spray dried immobilized photocatalyst as well as the photon absorption in the Photo-CREC-Air Reactor.

Chapter 9

9 Results and Discussion: Kinetic Analysis for the Photodegradation of Acetone and Acetaldehyde ‘

This chapter addresses the development of a kinetic model for the mineralization of acetone and acetaldehyde into CO₂ in a Photo-CREC-Air Reactor using the 1% TiO₂-AAS-ASC method (2.2g TiO₂). The proposed model is expected to address the following issues:

- ✓ Could a Langmuir-Hinshelwood model based on a series-parallel model be used for the mineralization of acetone and acetaldehyde? Will intermediate species be required for both models?
- ✓ Could kinetic parameters be estimated based on experimental data? Could adsorption constants be calculated by developing independent adsorption experiments?

Regarding these issues, one can mention that the Langmuir-Hinshelwood (L-H) model was successfully considered for the gas phase photodegradation of acetone, acetaldehyde and their intermediate species on TiO₂ (Peral & Ollis, 1992; Sauer & Ollis, 1994; Sauer & Ollis, 1996). The L-H models are based on the following assumptions: a) the acetone, acetaldehyde and intermediate compounds adsorb on the TiO₂ surface prior to their reaction with the oxidizing species, b) the CO₂ does not adsorb on the surface, c) the adsorption steps are in “dynamic equilibrium” and d) the degradation of organic compounds due photolysis is neglected.

On the basis of the above, a L-H equation can be considered using a generic notation with “i” representing any of the organic species,

$$r_{i,j} = \frac{k^k_i K^A_i C_{i,g}}{1 + \sum_{i=1}^n K^A_i C_{i,g}} \quad (9.1)$$

where r_i accounts for the reaction rate ($\mu\text{mole}/\text{cm}^2_{\text{irr}}\text{-min}$), k_i^k denotes the kinetic constant that includes the effects of the local rate of photon absorption ($\mu\text{mole}/\text{cm}^2_{\text{irr}}\text{-min}$), K_i^A refers to the adsorption constant ($1/\mu\text{mole}$) and C_i denotes the concentration of organic species involved in the photocatalytic reaction ($\mu\text{mole}/\text{l}$).

Furthermore, the ‘batch’ operation of the Photo-CREC-Air Reactor, can be modeled via the following equation:

$$r_{i,j} = \frac{1}{A_{\text{irr}}} \frac{dN_i}{dt} = \frac{V}{A_{\text{irr}}} \frac{dC_i}{dt} \quad (9.2)$$

where A_{irr} accounts for the photocatalyst irradiated area (cm^2_{irr}), V represents the reactor volume (l), N_i symbolizes the number of moles of i (μmole) and t indicates the time (min). The final general Langmuir-Hinshelwood equation for this system is therefore,

$$\frac{V}{A_{\text{irr}}} \frac{dC_i}{dt} = \frac{k_i^k K_i^A C_{i,g}}{1 + \sum_{i=1}^n K_i^A C_{i,g}} \quad (9.3)$$

Given that the organic species are measured in the gas phase, and that the organic species are both in the gas and immobilized solid phases, this equation has to be modified as follows,

$$\frac{dC_i}{dt} = \frac{d(C_{i,g} + C_{i,s})}{dt} = \frac{d\left(C_{i,g} + \frac{WQ_{i,\text{max}} K_i^A C_{i,g}}{V (1 + K_i^A C_{i,g})}\right)}{dt} \quad (9.4)$$

The consideration of the full Langmuir term on the numerator in Eq. 9.4 can become a challenge. In order to simplify this, just for this case one can consider that $K_i C_i \ll 1$ for all chemical species (Langmuir isotherm is fitted with a linear curve), Eq. (9.4) becomes,

$$\frac{dC_i}{dt} = \frac{(K_i^A + 1)dC_{i,g}}{dt} \quad (9.5)$$

where $K' = WQ_{i,max}K_i^A/V$.

Thus, equation (9.3) yields,

$$\frac{V}{A_{irr}} \frac{(K'_i + 1) dC_{i,g}}{dt} = \frac{k_i^k K_i^A C_i}{1 + \sum_{i=1}^n K_i^A C_i} \quad (9.6)$$

One can notice that Eq. (9.6) can be used to describe the kinetic behaviour of every organic species as well as the CO₂ present in the photoreactor.

Concerning the parameters included in Eq. (9.6), they are of two classes, as described above: a) kinetic constants and b) adsorption constants. Since the adsorption and kinetic parameters are present in both the numerator and the denominator of Eq. (9.6), there is a potential kinetic parameter calculation uncertainty given their high degree of cross-correlation.

To address the issue of reducing parameter cross-correlation, one can calculate adsorption constants with independent “dark” adsorption experiments, as will be shown in the upcoming “Langmuir Isotherms” section.

9.1 Langmuir Isotherms

It has been shown that the Langmuir model provides a good approximation to describe chemisorption at equilibrium (Batault et al., 2015; Garcia-Hernandez et al., 2012). This isotherm relates the adsorbed organic species per unit TiO₂ weight (Q_i in $\mu\text{mole/g}$ of photocatalyst) to the organic species concentration in the gas phase ($C_{i,g}$ in $\mu\text{mole/L}$) as follows:

$$Q_i = Q_{i,max} \frac{K_i^A C_{i,g}}{1 + K_i^A C_{i,g}} \quad (9.7)$$

where $Q_{i,max}$ ($\mu\text{mole/g}_{cat}$) represents the number of moles of organic species adsorbed as a monolayer per unit of TiO₂ weight; and K_i^A ($\text{L}/\mu\text{mole}$) is the adsorption constant of the

compound. The K^A_i represents the affinity of the organic compound to the immobilized TiO_2 surface.

Adsorption equilibrium was reached after 30 minutes in the Photo-CREC-Air Reactor under dark conditions for both acetone and acetaldehyde. Figure 44 reports the adsorption isotherm of acetone, acetaldehyde and formaldehyde using the TiO_2 -AAS-ASC mesh, and showing the adequacy of the selected Langmuir model.

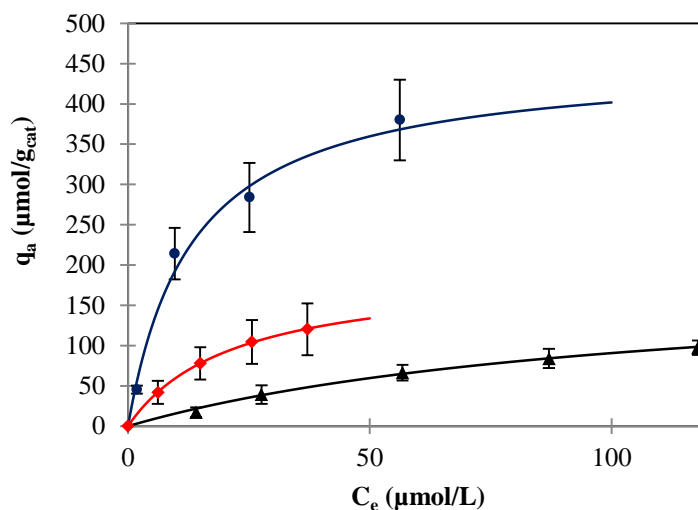


Figure 44: a) Langmuir Adsorption Isotherm of Acetone (red diamonds), Acetaldehyde (black triangles) and Formaldehyde (blue circles) on 1%wt Degussa P25 TiO_2 -AAS-ASC. Reported data points and standard deviations included at least 5 repeats of independent experiments.

The K^A and Q_{max} parameters of eq. (9.7), reported in Table 11, were calculated using a nonlinear least squares regression algorithm.

Table 11. Langmuir Parameters for the Adsorption of Acetone, Acetaldehyde and Formaldehyde at equilibrium conditions on Immobilized Degussa P25 TiO_2 .

	<i>Acetone</i>		<i>Acetaldehyde</i>		<i>Formaldehyde</i>	
Q_{max} ($\mu\text{mole/g}_{\text{cat}}$)	192	± 38	189	± 56	455	± 68
K^A ($1/\mu\text{mole}$)	0.04	± 0.012	0.009	± 0.002	0.1	± 0.016

Regarding adsorption parameters, they can differ under radiation or “dark” conditions (Xu & Langford, 2000). In spite of this, parameters obtained under “dark conditions”, can be considered as close estimates (Moreira et al., 2012). Several authors report Langmuir adsorption parameters for acetone, acetaldehyde and formaldehyde in air using Degussa P25 (Batault et al., 2015; Coronado et al., 2003; El-Maazawi et al., 2000; Noguchi, Fujishima, Sawunyama, & Hashimoto, 1998; Raupp & Junio, 1993; Sauer & Ollis, 1994). The estimated parameter values can vary with temperature, humidity and semiconductor immobilization, with all of them being possible contributing factors (Batault et al., 2015). Furthermore, other authors prefer to estimate the adsorption constants under reaction conditions (Ballari et al., 2015; Bettoni et al., 2013; Le Behec et al., 2015). In this respect, this strategy was adopted in previous studies using the Photo-CREC-Air Reactor: a) 4.5×10^{-5} and $7.1 \times 10^{-6} \text{ m}^3/\mu\text{mole}$, respectively for acetone and acetaldehyde (Ibrahim & de Lasa, 2004) and b) 4.8×10^{-5} and $3.1 \times 10^{-6} \text{ m}^3/\mu\text{mole}$ for acetone and acetaldehyde, respectively (Garcia-Hernandez et al., 2012). There are issues with this approach given high adsorption parameter cross-correlation.

To address this issue, adsorption parameters were calculated in the present study under “dark conditions”. This led as shown in Table 11, to close and more trustable adsorption parameters (less degree of cross-correlation) of 4×10^{-5} and $9 \times 10^{-6} \text{ m}^3/\mu\text{mole}$ for acetone and acetaldehyde, respectively.

9.2 Acetone Kinetic Model and Parameter Estimation

9.2.1 *Series- Parallel and L-H Model for Acetone*

The photocatalytic degradation of acetone was performed in the Photo-CREC-Air Reactor for initial acetone concentrations ranging from 25 to 250 $\mu\text{mole/L}$. Regarding acetone decomposition, it is anticipated that this involves more than one measurable organic species, with acetaldehyde having a special role in this. To confirm this, organic solvent extraction was practiced on the immobilized TiO_2 . In addition, gas samples were taken very close to the mesh. Acetaldehyde was identified as an intermediate species in the photodegradation of acetone. No other intermediate compounds were identified. This finding is in agreement with others that claim that this species is a main measurable

intermediate in the photodegradation of acetone (Bianchi et al., 2014; Sauer & Ollis, 1996).

On the basis of the above experimental observations, Figure 45 describes the proposed macro kinetic model for acetone mineralization. Three species (acetone, acetaldehyde and CO_2) and the related kinetic constants are considered: a) kinetic constant for the conversion of acetone to acetaldehyde, $k_{\text{Acetone} \rightarrow \text{Acetal}}$; 2) kinetic constant for the conversion of acetone to CO_2 , $k_{\text{Acetone} \rightarrow \text{CO}_2}$; and 3) kinetic constant for the conversion of acetaldehyde to CO_2 , $k_{\text{Acetal} \rightarrow \text{CO}_2}$.

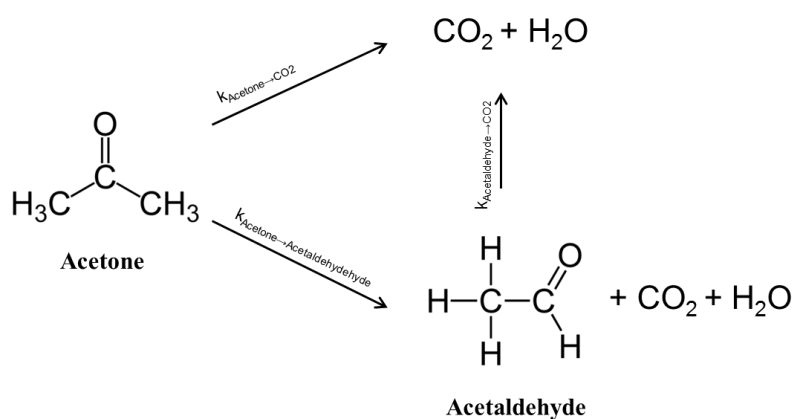
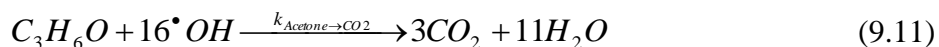
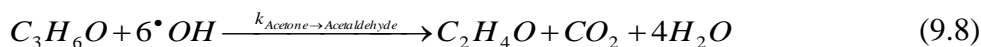


Figure 45: Schematic Representation of the Proposed Mechanism for the Photodegradation of Acetone in the Photo-CREC-Air Reactor.

On this basis, the following stoichiometric relations can be established based on:



Regarding acetaldehyde, it was observed to be present in small concentrations with no species other than acetone and CO_2 being detected. For instance, acetaldehyde never

surpassed 10 $\mu\text{mole/L}$ in the gas phase for 49 $\mu\text{mole/L}$ initial acetone concentrations. These small levels of acetaldehyde were rather difficult to measure and quantify accurately. Therefore, acetaldehyde was accounted via total carbon closure using the following equation,

$$N_C = N_{C,Acetone} + N_{C,Acetal} + N_{C,CO_2} \quad (9.12)$$

where N_C is the total number of moles of carbon molecules, $N_{C,Acetone}$ is the number of moles of carbon contained in acetone, $N_{C,Acetal}$ is the number of moles of carbon contained in acetaldehyde, and N_{C,CO_2} is the number of moles of carbon contained in CO_2 .

Thus, the number of moles of carbon contained in acetaldehyde can be defined as,

$$N_{C,Acetal} = N_C - N_{C,Acetone} - N_{C,CO_2} \quad (9.13)$$

Eq. (9.13) can be transformed in terms of concentration of the species at constant volume into,

$$(1 + K'_{Acetal})C_{Acetal} = \frac{3}{2}(1 + K'_{Acetone})(C_{Acetone,0} - C_{Acetone}) - \frac{1}{2}(1 + K'_{CO_2})C_{CO_2} \quad (9.14)$$

where the adsorption constant of CO_2 on TiO_2 is considered to be $K_{CO_2}=0$, and therefore,

$$(1 + K'_{Acetal})C_{Acetal} = \frac{3}{2}(1 + K'_{Acetone})(C_{Acetone,0} - C_{Acetone}) - \frac{1}{2}C_{CO_2} \quad (9.15)$$

Based on the Langmuir-Hinshelwood reaction rate formulation, the reaction rate for acetone, acetaldehyde and CO_2 is given by,

$$\frac{V}{A_{irr}} \frac{(1 + K'_{Acetone})dC_{Acetone,g}}{dt} = \frac{(k_{Acetone \rightarrow Acetal} + k_{Acetone \rightarrow CO_2})K^A_{Acetone}C_{Acetone,g}}{1 + K^A_{Acetone}C_{Acetone,g} + K^A_{Acetal}C_{Acetal,g}} \quad (9.16)$$

$$\frac{V}{A_{irr}} \frac{(1 + K'_{Acetal}) dC_{Acetal,g}}{dt} = \frac{3/2 k_{Acetone \rightarrow Acetal} K^A_{Acetone} C_{Acetone,g} - k_{Acetal \rightarrow CO_2} K^A_{Acetal} C_{Acetal,g}}{1 + K^A_{Acetone} C_{Acetone,g} + K^A_{Acetal} C_{Acetal,g}} \quad (9.17)$$

$$\frac{V}{A_{irr}} \frac{dC_{CO_2}}{dt} = \frac{(k_{Acetone \rightarrow Acetal} + 3k_{Acetone \rightarrow CO_2}) K^A_{Acetone} C_{Acetone,g} + 2k_{Acetal \rightarrow CO_2} K^A_{Acetal} C_{Acetal,g}}{1 + K^A_{Acetone} C_{Acetone,g} + K^A_{Acetal} C_{Acetal,g}} \quad (9.18)$$

where $C_{i,g}$ is the concentration of species “i” in the gas phase ($\mu\text{mole/l}$); C_{CO_2} is the total concentration of CO_2 ($\mu\text{mole/l}$); $k_{Acetone \rightarrow Acetal}$, $k_{Acetal \rightarrow CO_2}$ and $k_{Acetone \rightarrow CO_2}$ are the rate constants for the reactions (9.8), (9.10) and (9.11), respectively ($\mu\text{mole/cm}^2_{irr}\text{-min}$); K^A_i is the adsorption constant for the species “i” ($l/\mu\text{mole}$); A_{irr} is the wire mesh irradiated area (1042 cm^2_{irr}) and V is the volume of the reactor (55.08 L).

9.2.2 Parameter Estimation for Acetone Photo-Conversion

Parameter estimation for the selected L-H model using experimental data was performed using MATLAB with three parameters to be calculated: $k_{Acetone \rightarrow Acetal}$, $k_{Acetal \rightarrow CO_2}$ and $k_{Acetone \rightarrow CO_2}$ (Appendix K).

The MATLAB program used involved two subroutines: a) *lsqcurvefit* that minimizes the integration of the objective function and b) *ode45* that solves for the numerical integration of the three differential equations. Five initial concentrations of acetone were considered: 25, 37, 50, 124, 247 $\mu\text{mole/L}$ using the experimental profiles of CO_2 , acetone and acetaldehyde with 5 replicas at 6 irradiation times. Therefore, the parameters were estimated using 450 experimental data points. Parameter boundaries of $k_{Acetone \rightarrow Acetal}$ and $k_{Acetone \rightarrow CO_2}$ were established analytically using initial reaction rate experimental data.

Figure 46 reports the initial reaction rates for acetone and CO_2 at the different initial acetone concentrations. One can notice that the reaction rates for acetone and CO_2 reach a constant value after initial acetone concentrations of 50 $\mu\text{mole/L}$.

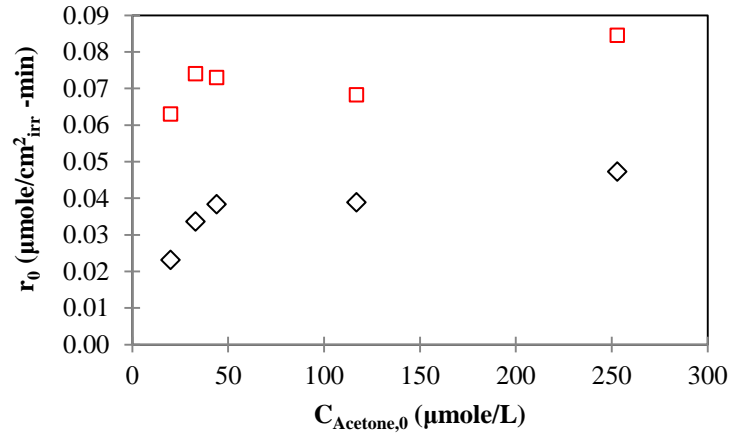


Figure 46: Effect of the Initial Acetone Concentration on the Initial Reaction Rate of Acetone (empty black diamonds) and CO₂ (empty red squares).

Table 12 reports the calculated parameters $k_{Acetone \rightarrow Acetal}$ and $k_{Acetone \rightarrow CO_2}$ at initial conditions. In fact, at $t=0$ the concentration of acetaldehyde can be considered zero and the parameters can be calculated analytically using the Eq. (9.16) and Eq. (9.18) simultaneously.

$$k_{Acetone \rightarrow Acetal} + 3k_{Acetone \rightarrow CO_2} = \frac{1 + K^A_{Acetone} C_{Acetone,g}}{K^A_{Acetone} C_{Acetone,g}} \frac{V}{A_{irr}} \frac{dC_{CO_2}}{dt} \quad (9.19)$$

$$k_{Acetone \rightarrow Acetal} + k_{Acetone \rightarrow CO_2} = \frac{1 + K^A_{Acetone} C_{Acetone,g}}{K^A_{Acetone} C_{Acetone,g}} \frac{V}{A_{irr}} \frac{(1 + K'^{Acetone}) dC_{Acetone,g}}{dt} \quad (9.20)$$

Table 12. Parameter Boundary Estimation at Initial Conditions. Concentrations are expressed in μmole/L, Reaction Rates in μmole/cm²_{irr}-min and Kinetic Reaction Constants in μmole/cm²_{irr}-min.

$C_{Acetone,0}$	r_{CO_2}	$r_{Acetone,0}$	$k_{Acetone \rightarrow Acetal} + k_{Acetone \rightarrow CO_2}$	$k_{Acetone \rightarrow Acetal} + 3k_{Acetone \rightarrow CO_2}$	$k_{Acetone \rightarrow CO_2}$	$k_{Acetone \rightarrow Acetal}$
20	0.063	0.023	0.052	0.142	0.045	0.007
33	0.074	0.034	0.059	0.130	0.036	0.024
44	0.073	0.038	0.060	0.114	0.027	0.033
117	0.068	0.039	0.047	0.083	0.018	0.029
253	0.084	0.047	0.052	0.093	0.020	0.031
Average			0.055±0.005	0.112±0.025	0.029±0.011	0.025±0.011

One should notice that the standard deviation of the calculated parameters as reported in Table 12, was used as the boundary condition for the parameter estimation employing MATLAB.

Table 13 reports the $k_{Acetone \rightarrow Acetal}$, $k_{Acetal \rightarrow CO_2}$ and $k_{Acetone \rightarrow CO_2}$ estimated parameters, the 95% Confidence Intervals (CI) and the Standard Deviation (STD) of each parameter. One can notice that the STD is smaller than 15%. Confidence Intervals are 21%, 8% and 22% for $k_{Acetone \rightarrow Acetal}$, $k_{Acetal \rightarrow CO_2}$ and $k_{Acetone \rightarrow CO_2}$, respectively.

Table 13. Estimated Parameters with a 0.98 Correlation Coefficient for Acetone Photodegradation using 1%wt% TiO₂-AAS-ASC.

Parameter ($\mu\text{mole}/\text{cm}^2_{\text{irr}}\text{-min}$)	Value	95% CI	STD
$k_{Acetone \rightarrow Acetaldehyde}$	0.025	0.005	0.003
$k_{Acetone \rightarrow CO_2}$	0.030	0.003	0.002
$k_{Acetaldehyde \rightarrow CO_2}$	0.046	0.011	0.007

Furthermore, Table 14 reports the cross-correlation parameters for $k_{Acetone \rightarrow Acetal}$, $k_{Acetone \rightarrow CO_2}$ and $k_{Acetal \rightarrow CO_2}$. One can observe that all parameter pairs display from low to moderate cross-correlation coefficients, with these findings further validating the kinetic model proposed.

Table 14. Cross-Correlation Coefficient Matrix for the Estimated Parameters in the Case of Acetone Photodegradation using 1%wt% TiO₂-AAS-ASC.

	$k_{Acetone \rightarrow Acetaldehyde}$	$k_{Acetone \rightarrow CO_2}$	$k_{Acetaldehyde \rightarrow CO_2}$
$k_{Acetone \rightarrow Acetaldehyde}$	1.00		
$k_{Acetone \rightarrow CO_2}$	-0.73	1.00	
$k_{Acetaldehyde \rightarrow CO_2}$	0.55	-0.80	1.00

Figure 48 reports the experimental concentration profiles of acetone and CO₂ as well as the ones predicted using the proposed acetone photocatalytic degradation kinetics with the 1%wt% TiO₂-AAS-ASC mesh. It is in this way proven, that the proposed kinetics is able to predict the concentrations of acetone and CO₂ for the entire acetone initial concentration range, fitting the kinetic model to the experimental data with a correlation coefficient of 0.98.

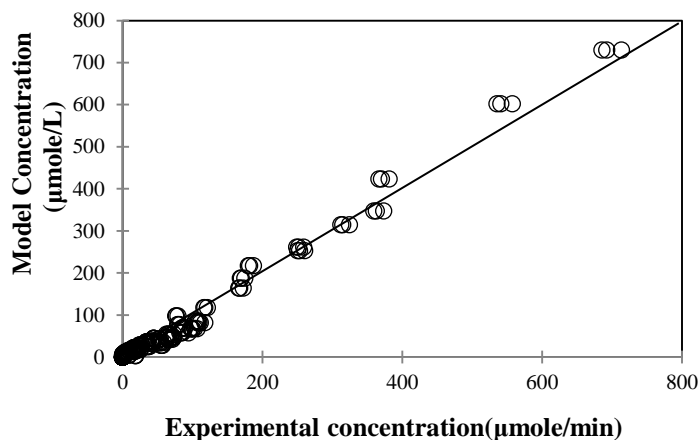


Figure 47: Comparison of the Experimental Data and the L-H Model for Acetone and CO₂ concentrations, using the 3 Fitted Parameters for the Photodegradation of Acetone using 1%wt% TiO₂-AAS-ASC.

Furthermore, Figures 48 and 49 display the acetone and CO₂ concentrations and their changes with irradiation times for various runs.

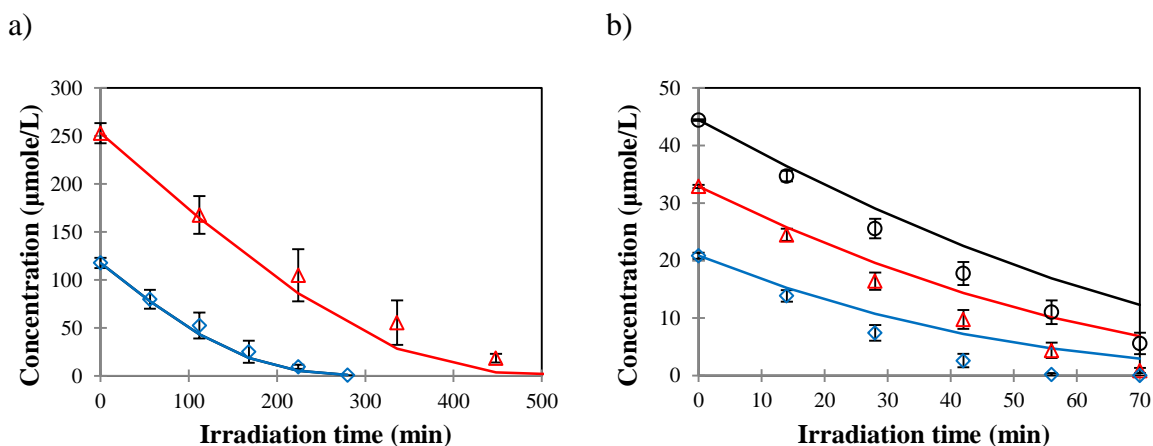


Figure 48: Acetone Concentration Changes with Irradiation Time using the 1%wt% TiO₂-AAS-ASC. Codes: a) Empty Symbols Shows Experimental Concentrations; b) Full Lines Describes Concentration as per the L-H Method Five initial concentrations of acetone were considered: a) 124 (blue \diamond), 247 (red Δ) $\mu\text{mole/L}$; b) 25 (blue \diamond), 37 (red Δ) and 50 (black \circ) $\mu\text{mole/L}$. Note: the error bars show the standard deviation of each point.

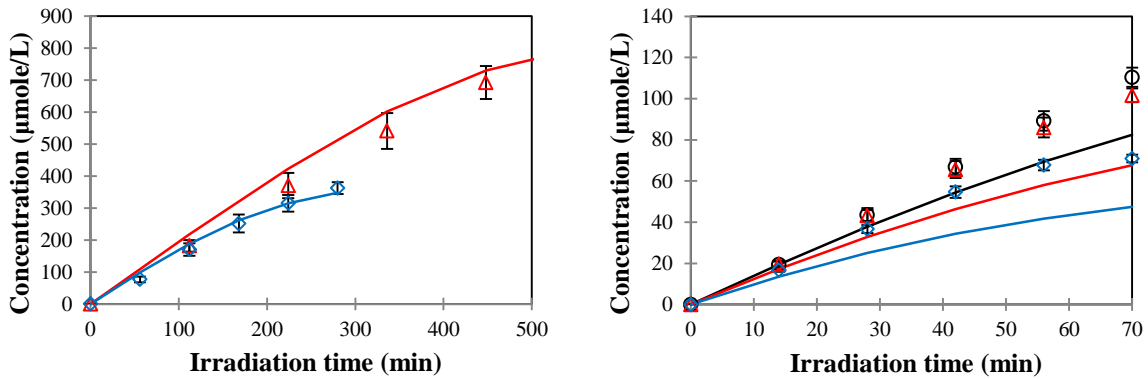


Figure 49: CO₂ Concentration Changes with Irradiation Time during the Photocatalytic Degradation of Acetone using the 1% wt% TiO₂-AAS-ASC. Empty Symbols Shows Experimental Data, Full line displays L-H Model Predictions. Five initial concentrations of acetone were considered: a) 124 (blue \diamond), 247 (red Δ); b) 25 (blue \diamond), 37 (red Δ) and 50 (black \circ) $\mu\text{mole/L}$. Note: the error bars show the standard deviation of each point.

One can observe in Figures 48 and 49 that the L-H model describes acetone and CO₂ concentrations particularly well at high initial $C_{Acetone}$. On the other hand, at the lower initial $C_{Acetone}$ concentrations, the kinetic model, while describing the overall concentration changes, appears to be less reliable.

In order to further establish the causes of the deviation of the proposed kinetics, the combined total carbon concentration changes in both the gas phase and solid phases were calculated including CO₂, acetone and acetaldehyde as follows,

$$C_C = (1 + K'_{Acetone})C_{Acetone} + (1 + K'_{Acetal})C_{Acetal} + (1 + K'_{CO_2})C_{CO_2} \quad (9.21)$$

with a K_{CO_2} assumed to be zero.

Figure 50 reports the combined carbon concentration including all species present. It is valuable to see that the total carbon as predicted by the L-H model and the experimental data remains close to constant. Thus, this provides a strong backing of one main model L-H assumption: acetone, acetaldehyde and CO₂ are the sole species to be considered in the model formulation.

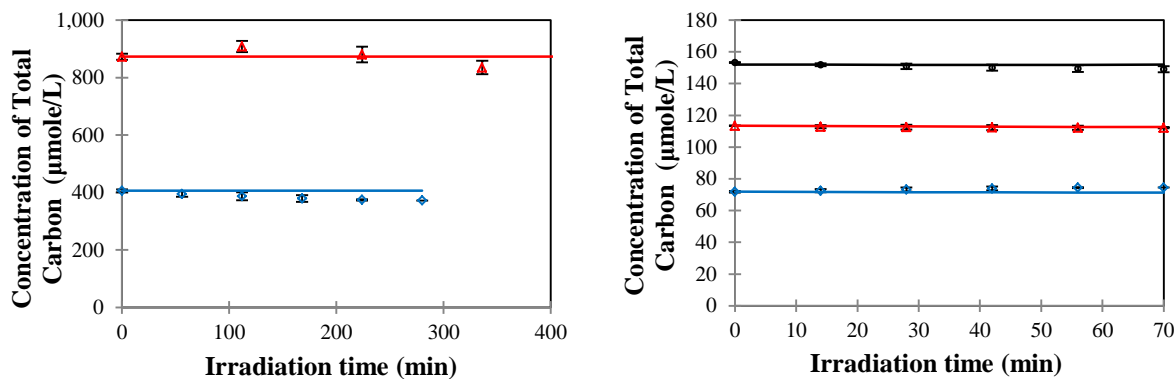


Figure 50: Total Carbon Concentration in both gas and solid phases during Photocatalytic Degradation of Acetone using the 1%wt% TiO₂-AAS-ASC at various irradiation times. Filled Symbols show experimental data, Full lines represent L-H Model Predictions. Five initial concentrations of acetone were used: a) 124 (blue \diamond), 247 (red Δ); b) 25 (blue \diamond), 37 (red Δ) and 50 (black \circ) $\mu\text{mole/L}$.

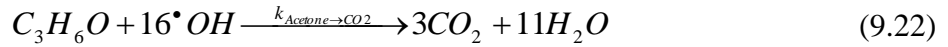
Given Figure 49 results, and given that one still has to shed light into the issue of modest fitting at low initial acetone concentrations, a further attempt of model fitting suitable for low initial acetone concentrations was attempted. This approach is described in the upcoming section 9.2.3.

9.2.3 Kinetic Model for Low Concentrations

The kinetic model as established in Section 9.2.2 included acetaldehyde as an intermediate species. Model parameters were adjusted using acetone and CO₂ concentrations. Model predictions were adequate for high initial acetone concentrations in the 124-247 $\mu\text{mole/L}$ range. These predictions were less accurate for 25-50 $\mu\text{mole/L}$ acetone initial concentrations. It was noticed that at these conditions, the acetaldehyde concentration was in the range of experimental error. Therefore, the model was in fact overparametrized for the lower acetone initial concentrations. In this respect, [Chang et al. \(2003\)](#) also reported that acetone conversion could be described as a direct conversion to CO₂ at low initial concentrations, without the specific need of intermediate species. [Moreira et al. \(2012\)](#) also argued regarding the advantages of not accounting for

intermediate species at small organic model molecule concentrations in order to avoid overparametrization.

Therefore, a simplified model was proposed for the 0-50 $\mu\text{mole/L}$ acetone initial concentration range with acetone being converted to CO_2 directly:



As a result, and based on the Langmuir-Hinshelwood reaction rate formulation, the reaction rate for acetone conversion and CO_2 formation are given by,

$$\frac{V}{A_{\text{irr}}} \frac{(1 + K'_{\text{Acetone}}) dC_{\text{Acetone},g}}{dt} = \frac{k_{\text{Acetone} \rightarrow \text{CO}_2} K^A_{\text{Acetone}} C_{\text{Acetone},g}}{1 + K^A_{\text{Acetone}} C_{\text{Acetone},g}} \quad (9.23)$$

$$\frac{V}{A_{\text{irr}}} \frac{dC_{\text{CO}_2}}{dt} = \frac{3k_{\text{Acetone} \rightarrow \text{CO}_2} K^A_{\text{Acetone}} C_{\text{Acetone},g}}{1 + K^A_{\text{Acetone}} C_{\text{Acetone},g}} \quad (9.24)$$

Table 15 reports the estimated parameters for the photoconversion of acetone to CO_2 at conditions of low initial acetone concentrations (25-50 $\mu\text{mole/L}$). One can notice the narrow CIs and low STDs which provide evidence of simplified model adequacy for low acetone initial concentrations.

Furthermore, Figure 51 shows the predicted and experimental profiles of acetone and CO_2 . The simplified model predicts the changes of acetone and CO_2 well with a correlation coefficient of 0.97.

It is of interest to notice that the findings of this PhD thesis are in agreement with those of other authors who showed the value of a simplified model for the conversion of acetone in the same range as in the initial concentrations (Bettoni et al., 2013; Peral & Ollis, 1992; Sauer & Ollis, 1994). In addition, it is valuable to report that previous studies by Garcia-Hernandez et al. (2012) and Ibrahim and de Lasa (2004) reported 204 $\mu\text{mole/m}^3\text{-min}$ and 1315 $\mu\text{mole/m}^3\text{-min}$ kinetic constants respectively. These kinetic constants are in line with the 0.053 $\mu\text{mole/cm}^2_{\text{irr}}\text{-min}$ and the 1002 $\mu\text{mole/m}^3\text{-min}$ (1042 cm^2_{irr} and 55.08 l of reactor volume) of the present study.

Table 15. Estimated Parameters with a 0.97 Correlation Coefficient for Acetone Photodegradation using 1%wt% TiO₂-AAS-ASC.

Parameter ($\mu\text{mole}/\text{cm}^2_{\text{irr}}\cdot\text{min}$)	Value	95% CI	STD
$k_{\text{Acetone}\rightarrow\text{CO}_2}$	0.053	0.002	0.001

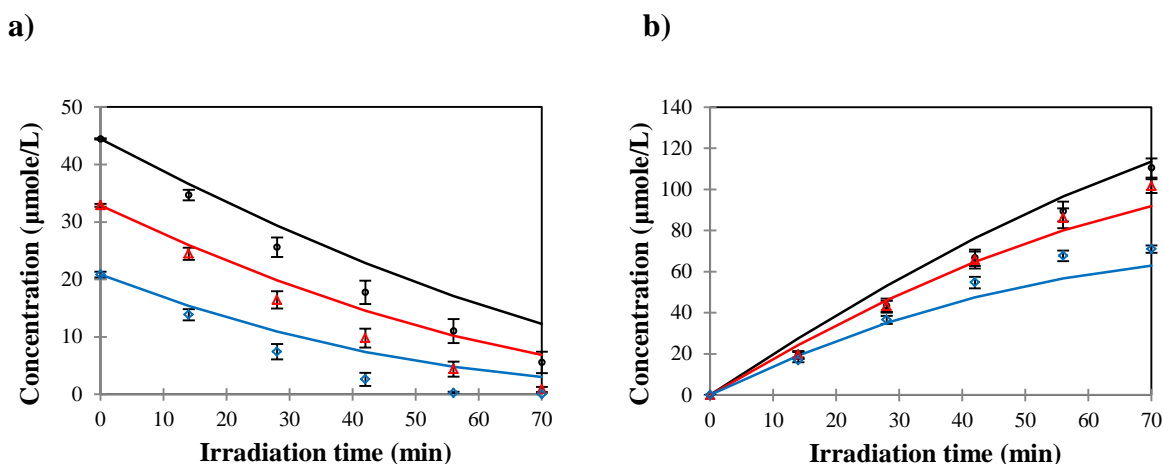


Figure 51: Changes of a) Acetone and b) CO₂ Concentrations. (empty symbols) and the estimated concentration profiles obtained by L-H method (continuous line) using the 1%wt% TiO₂-AAS-ASC. Three initial concentrations of acetone were considered: 25 (blue \diamond), 37 (red Δ) and 50 (black \circ) $\mu\text{mol}/\text{L}$. Note: The Error bars show the standard deviation of each point.

9.3 Acetaldehyde Modeling

9.3.1 Series- Parallel and L-H Model for Acetaldehyde

Acetaldehyde is an intermediate for acetone photodegradation and many other photodegradation reactions of VOCs (Debono et al., 2013; Debono et al., 2011; Farhanian & Haghightat, 2014). Thus, in order to understand the acetone kinetics better, it is valuable to consider the photoconversion of acetaldehyde.

To analyze this, acetaldehyde photocatalytic degradation studies were performed in the Photo-CREC-Air Reactor using five initial acetaldehyde concentrations: 31, 45, 59, 152 and 316 $\mu\text{mole/L}$. Figure 52 shows a typical run of acetaldehyde photodegradation using an initial concentration of 324 $\mu\text{mole/L}$.

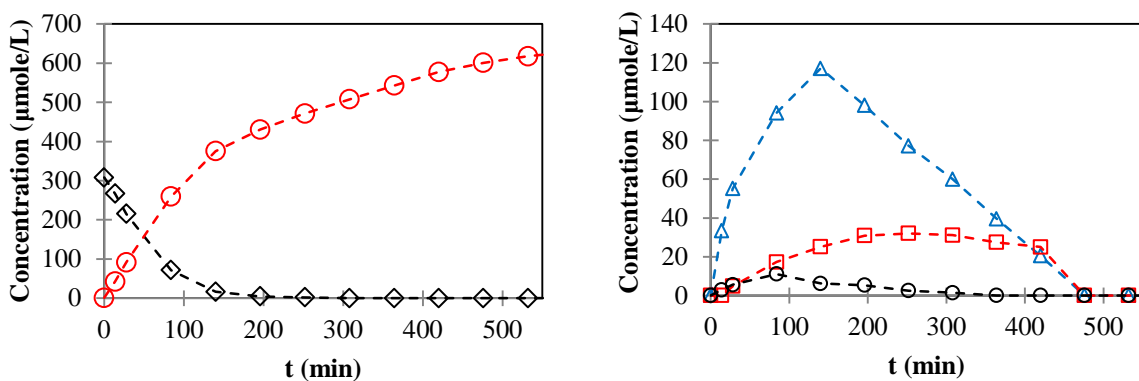


Figure 52: Concentration Profiles during the Photodegradation of 324 $\mu\text{mole/L}$ Acetaldehyde on 1%wt% $\text{TiO}_2\text{-AAS-ASC}$. a) Acetaldehyde (black \diamond), CO_2 (red \circ) b) Formaldehyde (blue Δ), Formic Acid (red \square) and Methanol (black \circ).

Figure 52 shows formaldehyde, formic acid and methanol as observed intermediate species of the photoconversion of acetaldehyde. These observed intermediate species are in agreement with previous studies (Bianchi et al., 2014; Hauchecorne & Lenaerts, 2013).

On the basis of the above data, Figure 53 reports a schematic representation of the series-parallel model for the photodegradation of acetaldehyde. One can notice that this reaction network including 7 parameters: $k_{\text{Acetald} \rightarrow \text{Formaldehyde}}$, $k_{\text{Acetal} \rightarrow \text{FormicAcid}}$, $k_{\text{Acetal} \rightarrow \text{CO}_2}$, $k_{\text{Acetal} \rightarrow \text{Methanol}}$, $k_{\text{Formaldehyde} \rightarrow \text{CO}_2}$, $k_{\text{FormicAcid} \rightarrow \text{CO}_2}$ and $k_{\text{Methanol} \rightarrow \text{CO}_2}$.

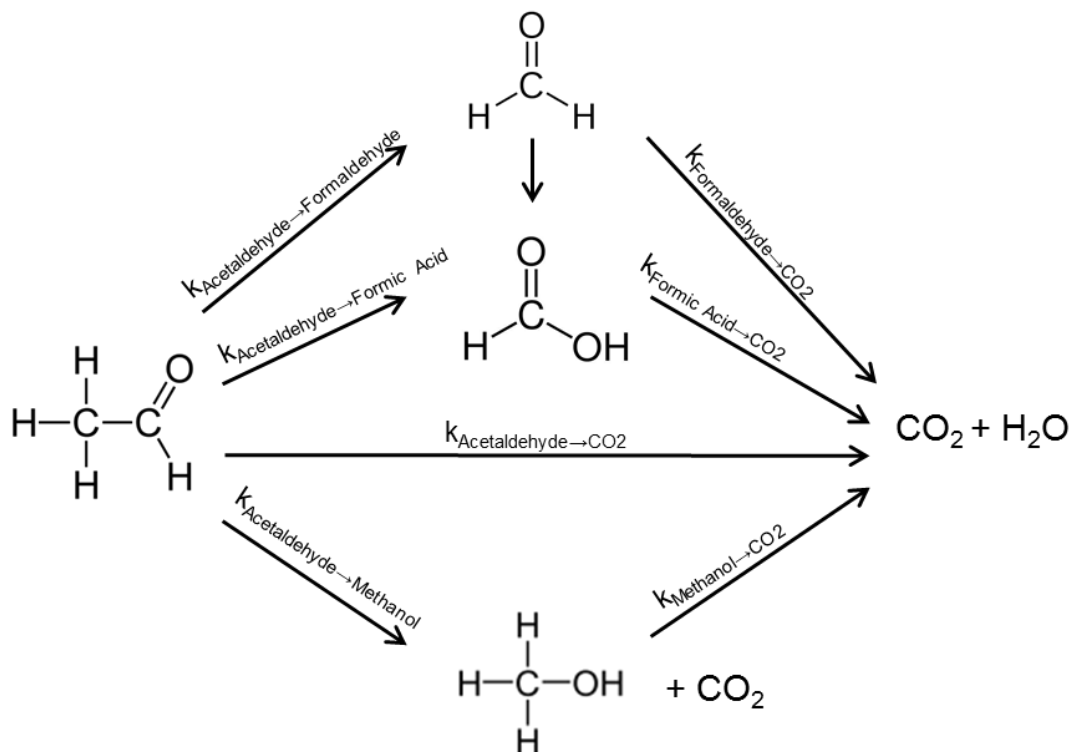


Figure 53: Schematic Representation of the Proposed Mechanism for the Photodegradation of Acetaldehyde in the Photo-CREC-Air Reactor.

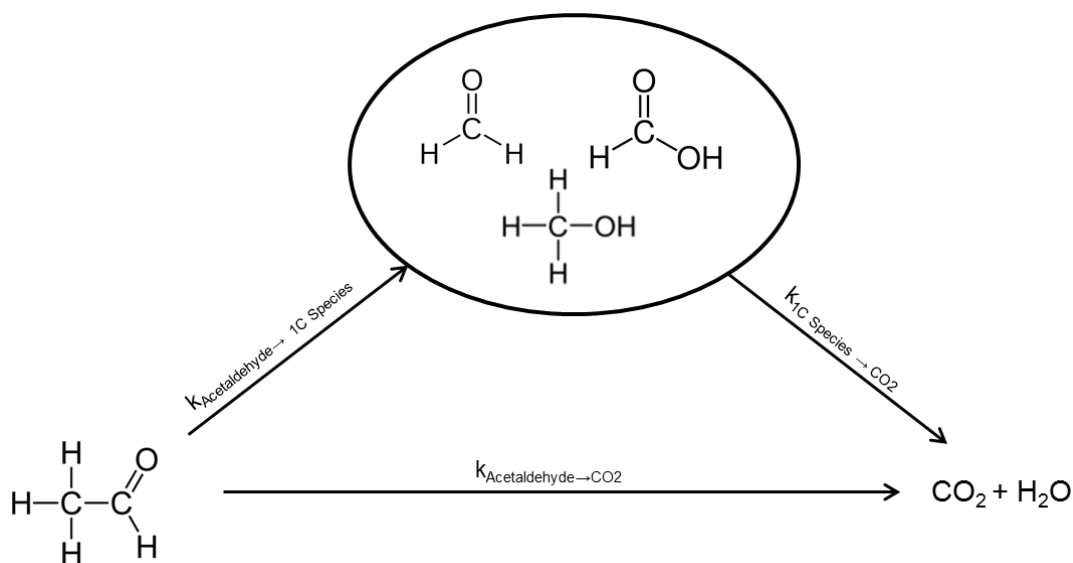
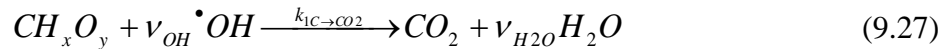
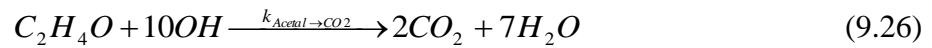
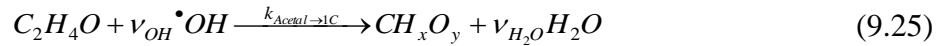


Figure 54: Schematic Representation of the Simplified Proposed Mechanism for the Photodegradation of Acetaldehyde in the Photo-CREC-Air Reactor.

Given the potential issues with cross-correlation and overparametrization, the kinetic model for acetaldehyde was simplified as described in Figure 54. One can notice that in this case, all the intermediate species having one carbon atom were lumped together in one single pseudo species designated as CH_xO_y . Hence, the number of parameters to be estimated ($k_{Acetal \rightarrow 1C}$, $k_{Acetal \rightarrow CO_2}$ and $k_{1C \rightarrow CO_2}$) decreased from 7 to 3 constants.

On the basis of the above the following set of stoichiometric equations can be considered,



Thus, the total concentration of one carbon intermediate species can be calculated using the following equation,

$$C_{1C,g} = \sum_{n=1}^n C_{1Ci,g} \quad (9.28)$$

Furthermore, and based on the Langmuir-Hinshelwood reaction rate formulation, the reaction rate for acetaldehyde, for the one carbon containing organic species lump and CO_2 are given as,

$$\frac{V}{A_{irr}} \frac{(1 + K'_{Acetal}) dC_{Acetal,g}}{dt} = - \frac{(k_{Acetal \rightarrow 1C} + k_{Acetal \rightarrow CO_2}) K^A_{Acetal} C_{Acetal,g}}{1 + K^A_{Acetal} C_{Acetal,g} + \overline{K^A}_{1C} C_{1C,g}} \quad (9.29)$$

$$\frac{V}{A_{irr}} \frac{(1 + \overline{K^A}_{1C}) dC_{1C,g}}{dt} = \frac{k_{Acetal \rightarrow 1C} K^A_{Acetal} C_{Acetal,g} - k_{1C \rightarrow CO_2} \overline{K^A}_{1C} C_{1C,g}}{1 + K^A_{Acetal} C_{Acetal,g} + \overline{K^A}_{1C} C_{1C,g}} \quad (9.30)$$

$$\frac{V}{A_{irr}} \frac{dC_{CO_2}}{dt} = \frac{2k_{Acetal \rightarrow CO_2} K^A_{Acetal} C_{Acetal,g} + k_{1C \rightarrow CO_2} \overline{K^A}_{1C} C_{1C,g}}{1 + K^A_{Acetal} C_{Acetal,g} + \overline{K^A}_{1C} C_{1C,g}} \quad (9.31)$$

with $\overline{K^A}_{1C}$ and $\overline{K^1}_{1C}$ representing the average adsorption constants, $k_{Acetal \rightarrow 1C}$, $k_{Acetal \rightarrow CO_2}$ and $k_{1C \rightarrow CO_2}$ denoting the reaction rate constants for the reactions (9.25), (9.26) and (9.27) in $\mu\text{mole}/\text{cm}^2_{\text{irr}}\text{-min}$.

9.3.2 Parameter Estimation for Acetaldehyde Photo-Conversion

Parameter estimation for the selected L-H model utilizing experimental data was performed using MATLAB. On this basis, three parameters were calculated: $k_{Acetal \rightarrow 1C}$, $k_{1C \rightarrow CO_2}$ and $k_{Acetal \rightarrow CO_2}$ (Appendix K). The numerical routines for parameter estimation are described in Section 9.2.2. Five initial concentrations of acetaldehyde were considered: 31, 45, 59, 152, 316 $\mu\text{mole}/\text{L}$. Parameter adjustment involved CO_2 , acetaldehyde and 1C species concentration profiles with 3 replicas at 6 strategically selected irradiation times. Therefore, kinetic parameters were predicted with 270 data points or a degree of freedom of 267.

Table 16 reports the $k_{Acetal \rightarrow 1C}$, $k_{1C \rightarrow CO_2}$ and $k_{Acetal \rightarrow CO_2}$ estimated parameters for acetaldehyde photodegradation on 1% wt $\text{TiO}_2\text{-AAS-ASC}$. Confidence Intervals and Standard Deviations for the calculated parameters are in the range of 12-18% and 10-14%, respectively.

Table 16. Estimated Parameters with a 0.97 Correlation Coefficient for Acetaldehyde Photodegradation using a 1%wt% $\text{TiO}_2\text{-AAS-ASC}$ mesh.

Parameter ($\mu\text{mole}/\text{cm}^2_{\text{irr}}\text{-min}$)	Value	95% CI	STD
$k_{Acetaldehyde \rightarrow 1C}$	0.77	0.14	0.11
$k_{Acetaldehyde \rightarrow CO_2}$	0.50	0.06	0.06
$k_{1C \rightarrow CO_2}$	0.04	0.006	0.004

Furthermore, Table 17 reports the cross-correlation matrix of the $k_{Acetal \rightarrow 1C}$, $k_{1C \rightarrow CO_2}$ and $k_{Acetal \rightarrow CO_2}$ estimated parameters. One can notice the modest cross-correlation of the parameters in the 0.43-0.52 range.

Table 17. Cross-Correlation Coefficient Matrix for Estimated Parameters. Acetaldehyde Photodegradation using 1%wt% TiO₂-AAS-ASC mesh.

	$k_{\text{Acetaldehyde} \rightarrow \text{1C}}$	$k_{\text{Acetaldehyde} \rightarrow \text{CO}_2}$	$k_{\text{1C} \rightarrow \text{CO}_2}$
$k_{\text{Acetone} \rightarrow \text{Acetaldehyde}}$	1.00		
$k_{\text{Acetone} \rightarrow \text{CO}_2}$	0.43	1.00	
$k_{\text{Acetaldehyde} \rightarrow \text{CO}_2}$	0.52	-0.45	1.00

Figure 55 reports the correlation of the experimental data with the predicted data. Thus, it is proven that the three estimated parameters and the kinetic model fitted the experimental data well with a correlation coefficient of 0.97.

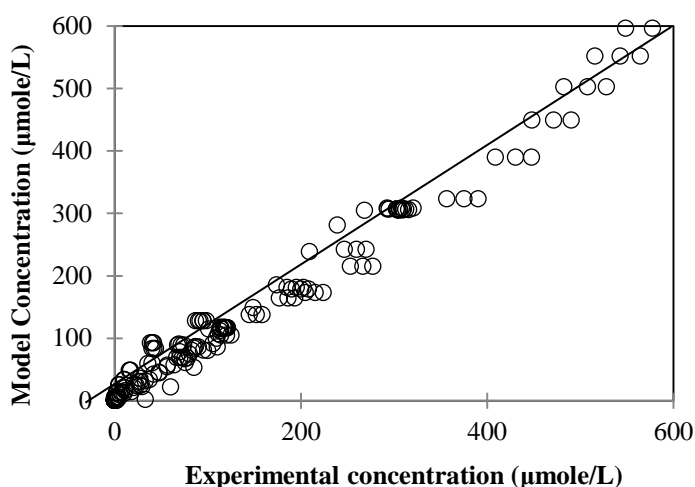


Figure 55: Comparison of the Experimental Data and the L-H Model Using 3 Fitted Parameters for the Photodegradation of Acetaldehyde using 1%wt% TiO₂-AAS-ASC mesh.

The parameters obtained in the present study are significantly larger than the 204 $\mu\text{mole}/\text{m}^3$ obtained in an early Photo-CREC-Air Reactor: (Ibrahim & de Lasa, 2004). This is a consequence of the various improvements of the Photo-CREC-Air Reactor in the area of photoreaction efficiency. It is also valuable to comment that the sum of the parameters for the degradation of acetaldehyde, $k_{\text{Acetal} \rightarrow \text{1C}} + k_{\text{Acetal} \rightarrow \text{CO}_2} = 1.27 \mu\text{mole}/\text{cm}^2_{\text{irr}}\text{-min}$ ($2.4 \times 10^4 \mu\text{mole}/\text{m}^3\text{-min}$) also surpasses the $2 \times 10^4 \mu\text{mole}/\text{m}^3\text{-min}$ for direct conversion of acetaldehyde to CO₂ ($k_{\text{Acetal} \rightarrow \text{CO}_2}$) as reported by Garcia-Hernandez et al. (2012) in the same Photo-CREC-Air Reactor. This represents about a 20% improvement with respect

to previous research, with this being assigned to a better engineering of the AAS-ASC mesh which uses a much lower loading of photocatalyst (close to three times lower).

Figures 56-58 report the comparison of experimental and predicted concentration profiles of acetaldehyde, CO₂ and one carbon containing species using the kinetic parameters reported in Table 16.

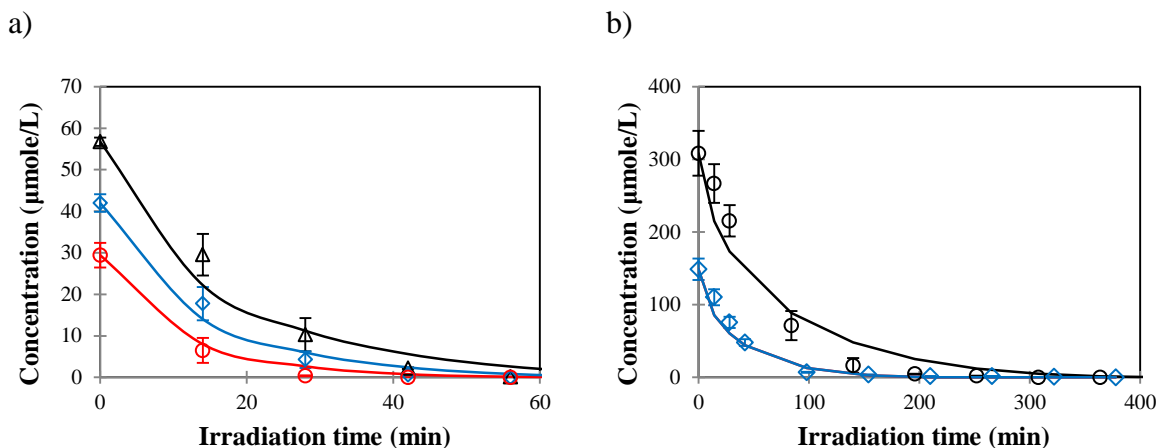


Figure 56: Changes of Acetaldehyde Concentration with irradiation time. Empty symbols represent experimental data and full lines calculated concentrations obtained by L-H Model using the 1%wt% TiO₂-AAS-ASC mesh. Five initial concentrations of acetaldehyde were considered: a) 31 (red ○), 45 (blue ◇) and 59 (black △) µmole/L; b) 152 (blue ◇), 316 µmole/L (black ○). Note: the error bars show the standard deviation of each point.

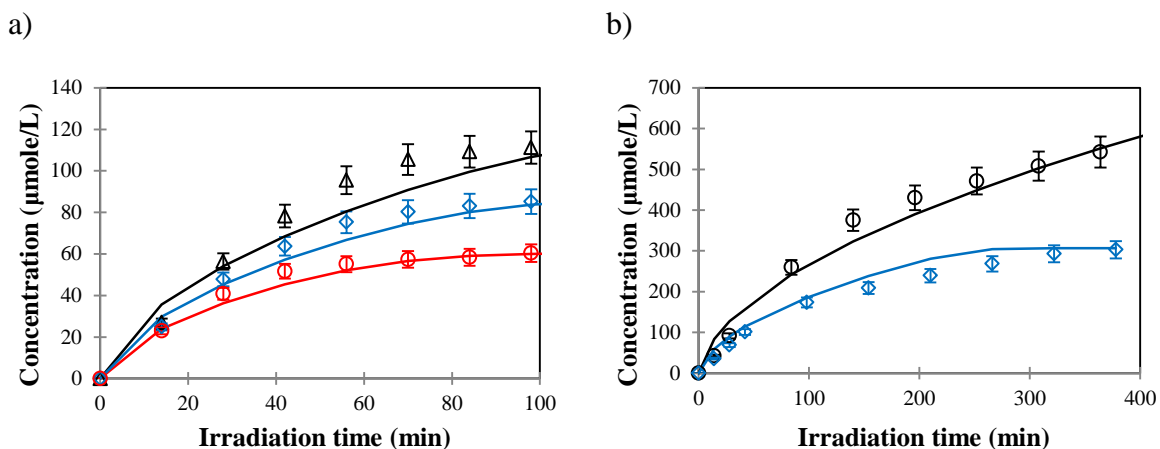


Figure 57: Changes of CO₂ Concentrations with Irradiation time. Empty Symbols report Experimental Data. Full lines describe Calculated Concentration Profiles Obtained by L-H Model, Using the 1%wt% TiO₂-AAS-ASC mesh. Five initial concentrations of acetaldehyde were considered: a) 31 (red ○), 45 (blue ◇) and 59 (black △) µmole/L; b) 152 (blue ◇), 316 (black ○) µmole/L. Note: the error bars show the standard deviation of each point.

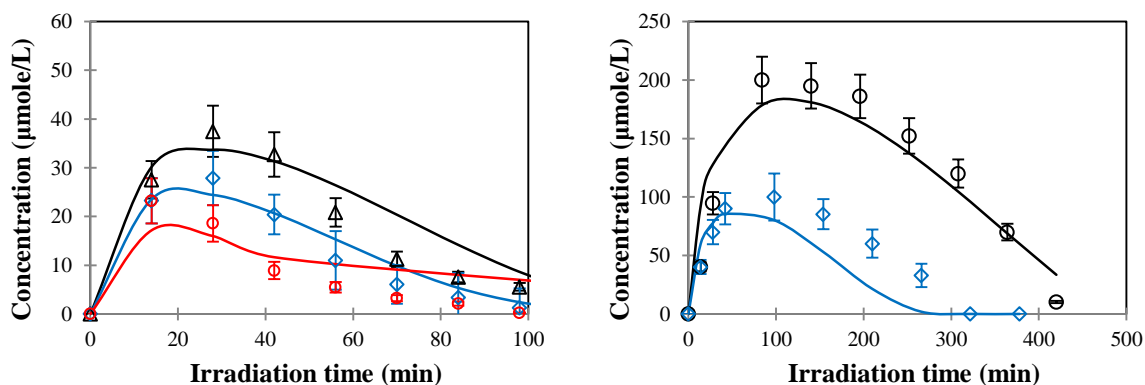


Figure 58: Changes of One Carbon Containing Species Concentrations with Irradiation Time. Empty Symbols represent Experimental Data and Full lines describe Concentration Profiles Obtained by L-H Method (continuous line) Using the 1%wt% TiO₂-AAS-ASC. Five initial concentrations of acetaldehyde were considered: a) 31 (red ○), 45 (blue ◇) and 59 (black △) µmole/L; b) 152 (blue ◇), 316 µmole/L (black ○). Note: the error bars show the standard deviation of each point.

One can notice in Figure 58 that there is a need of inclusion of intermediate species as suggested in previous studies (Garcia-Hernandez et al., 2012; Ibrahim & de Lasa, 2004). It is also observed that the proposed kinetic model is very adequate in representing various chemical species for the entire range of initial acetaldehyde concentrations.

Furthermore, and to establish the applicability of the proposed kinetics, a combined total carbon concentration including both the gas phase and solid phase species were considered,

$$C_C = (1 + K'_{Acetal})C_{Acetal} + (1 + \overline{K}'_{1C})C_{1C} + (1 + K'_{CO_2})C_{CO_2} \quad (9.21)$$

with a K_{CO_2} assumed to be zero.

Figure 59 reports the combined total carbon concentration showing that the L-H kinetics comply with the necessary condition of good carbon balance closure and this at all irradiation times and for all initial acetaldehyde concentrations .

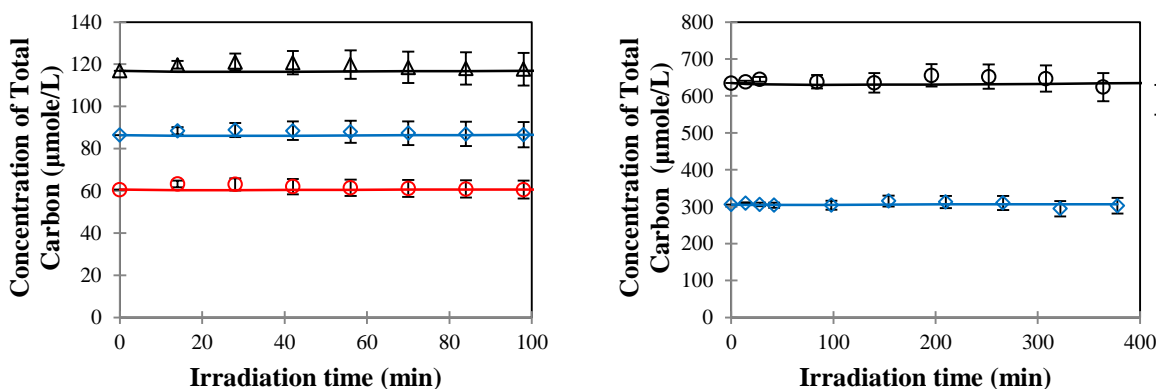


Figure 59: Changes of Total Carbon Concentration in the Gas and Solid Phases with Irradiation time. Empty symbols represent Experimental Data and Full Lines Calculated Concentration by L-H Model Using the 1%wt% TiO₂-AAS-ASC. Five initial concentrations of acetaldehyde were considered: a) 31 (red ○), 45 (blue ◇) and 59 (black Δ) µmole/L; b) 152 (blue ◇), 316 µmole/L (black ○). Note: the error bars show the standard deviation of each point.

9.4 Significance of the Developed Kinetic Model

As was shown in Sections 9.2 and 9.3, the series-parallel kinetic model is adequate for the prediction of the photodegradation of two characteristic model pollutants: acetone and acetaldehyde. Thus, and on this basis, it is considered quite possible that the series-parallel model will apply to the photodegradation of other organic molecules. The implication of this is that there is, on the prepared mesh, a variable photon density and as a result a distribution of TiO_2 sites with variable oxidation strengths.

Thus, one can expect different local $\bullet\text{OH}$ groups concentrations. This leads to a diversity of steps, each of them contributing to different oxidation extents. In the case of acetaldehyde, for example, the sites with higher strength lead to a complete mineralization of CO_2 while others with less strength lead to one carbon species formation. The same applies for acetone.

This distribution of oxidation sites is the result of different photon densities on the immobilized semiconductor. This phenomenon is very relevant given that it occurs regardless of photoreactor configuration, lamp nature or photocatalyst. One can notice that in the case of the immobilized photocatalyst, the photon density also varies through the film thickness depth. Thus, one can anticipate that the number of photons reaching the photocatalyst sites decreases progressively with the distance from the film mesh outer surface.

Figure 60a reports a description of the photon density and its changes with the photocatalyst normalized film depth. This finding is also supported by the RTE model reported in Appendix H. Therefore, even in isoactinic reactors, photons reaching the photocatalyst sites might differ given their location in the photocatalyst film.

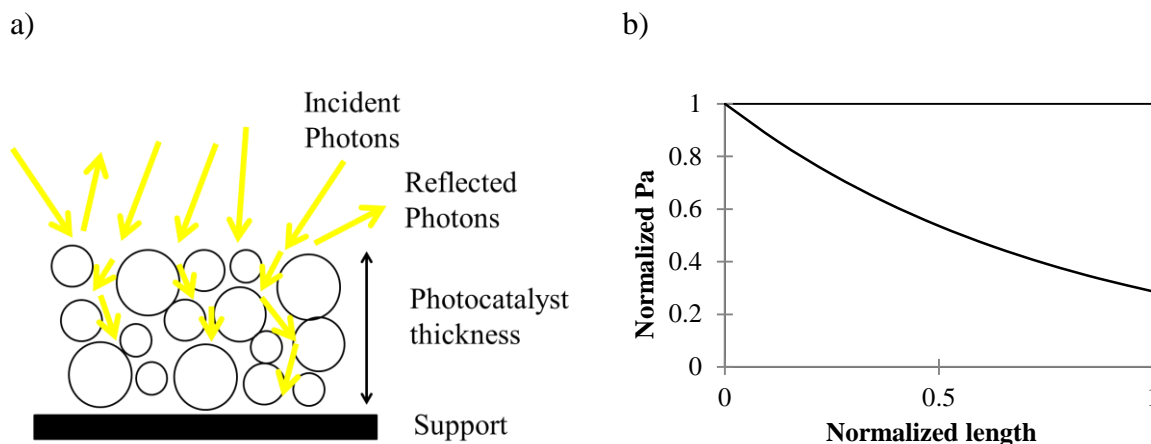


Figure 60: a) Schematic representation of the photons reaching the semiconductor surface through the TiO_2 film, b) Incident photons moving through the photocatalyst film as represented by the RTE model as shown in Appendix H.

One can see that regardless of the pollutant, the reactor configuration, the lamp source or the photocatalyst, a kinetic model which includes adsorption and intrinsic kinetics, being based in a parallel-in series model is of general applicability. The proposed parallel-in series kinetics, given its physicochemical basis, is a recommended strategy for the modeling of the photocatalytic degradation rate of organic pollutants in air.

Thus, the obtained kinetics and kinetic parameters must be applicable to a wide pollutant concentration range, with these findings being likely suitable for reactor scale-up.

9.5 Conclusions

- Both acetone and acetaldehyde photoconversion kinetics, are successfully considered on the basis of a series-parallel reaction network.
- The proposed series-parallel reaction network encompasses a Langmuir-Hinshelwood kinetics accounting for both adsorption and intrinsic reaction.
- Both the acetone and the acetaldehyde photoconversion kinetics require the inclusion of intermediate species, as a requirement for adequate photoconversion rates.

- d) The estimated kinetic parameters provide a successful prediction of the changes of the concentration of CO₂, acetaldehyde and one carbon containing species.
- e) The proposed kinetic models can be simplified using a reduced number of species under some conditions (e.g. low initial concentration of acetone, low intermediates acetaldehyde concentration). This is critical to avoid model overparametrization.
- f) The proposed kinetic model while being restricted to two model pollutants and one specific photoreactor (e.g. 55.1 liter Photo-CREC-Air), provides a framework of reference to establish the photodegradation kinetic of other organic species in air and other photoreactor scales.

Chapter 10

10 Conclusions and Recommendations

10.1 Conclusions

a) *Improved Immobilization TiO₂ Method*

An AAS-ASC spray slurry method was implemented for the immobilization of TiO₂ on a stainless steel mesh. Characterizations with SEM and gravimetry demonstrated that TiO₂-AAS-ASC provides a uniform and stable TiO₂ particle coating with little agglomeration. A thickness of 6-10 μm allows complete absorption of photons on the immobilized TiO₂. The developed TiO₂-AAS-ASC is highly active for the photodegradation of acetone and acetaldehyde in the 55.1 L Photo-CREC-Air Reactor. Moreover, the TiO₂-AAS-ASC method provides photocatalyst utilization 3 times more efficient than the previous TiO₂-SC technique.

b) *Energy Efficiency Factors*

Definitions and methodologies for photonic efficiency evaluations were established. Two Efficiency Parameters were considered: Quantum Yields (QY) and Photochemical Thermodynamic Efficiency Factors (PTEF). Definitions of these two factors involved macroscopic balances with the evaluation of irradiated, reflected and transmitted photons. The macroscopic energy balances developed in the Photo-CREC-Air Reactor allowed decoupling the calculations of the QYs and PTEFs from the η_{abs} absorption efficiency of irradiated photons. This provided valuable insights into the performance of the spray dried immobilized photocatalyst as well as the photon absorption in the Photo-CREC-Air Reactor.

The acetaldehyde photodegradation exhibited a higher photoreaction rate than acetone photodegradation. Therefore, the QYs and PTEFs for acetaldehyde mineralization values were in the 40-124% and in the 10-23% ranges; while the QYs and the PTEFs for acetone were in the 50-60% and 7-12% ranges. It was observed that the QYs and PTEFs were limited by the reaction of the organic

molecules with the formed OH^\bullet radicals and the ability of the molecules to trap semiconductor holes.

It was observed at initial concentrations larger than 110-150 $\mu\text{mole/L}$ that maximum PTEFs and QYs for acetaldehyde were very close to the expected 24.7% and 133% maximum values, respectively. This demonstrates the high degree of photon energy utilization with the spray TiO_2 immobilized photocatalysts in the Photo-CREC-Air Reactor. These high Quantum Yields close to 133%, can be considered an experimental validation of the reaction path, the stoichiometry and the thermodynamics for the calculation of the upper QYs and PTEFs limits.

c) *Series Parallel Reaction Network*

The proposed series-parallel reaction network encompasses a Langmuir-Hinshelwood kinetics. This kinetics accounts for both adsorption and intrinsic reaction. The L-H kinetic model for acetone photodegradation (initial concentrations of 25-253 $\mu\text{mole/L}$) with acetaldehyde as an intermediate fitted well the experimental data. In this case, a 98% correlation coefficient and an STD less than 15% were obtained. For lower initial concentrations of acetone (25-50 $\mu\text{mole/L}$) however, both acetone and CO_2 concentrations were predicted accurately, using a simplified kinetics without intermediates. On the other hand, the L-H kinetic model for acetaldehyde photodegradation included one intermediate species lump (formaldehyde, methanol and formic acid) and this for all initial acetaldehyde concentrations. The model was fitted with a 0.97 correlation coefficient and a STD less than 18% for 31-316 $\mu\text{mole/L}$ initial acetaldehyde concentrations.

Methodology for Scale-Up Air Photoreactors Analysis

- d) This PhD dissertation proposes a comprehensive methodology for a) photocatalyst immobilization, b) energy efficiency evaluation and c) a kinetic analysis for scaled-up photoreactors. It is our view that air photoreactors scale up should follow the methodology presented in this study in order to account adequately for the efficiency of the photocatalyst, the adequacy of the immobilization method and the design of the photoreactor.

10.2 Future Work and Recommendations

a) *Radiation Analysis*

It is proposed for future studies the effects of a) radiation intensity, b) photocatalyst loading, c) material support and d) photocatalyst nature, on macroscopic balance (incident, reflected and transmitted photons). It is suggested to evaluate these effects with experimental data and a Monte Carlo probabilistic model.

b) *Photocatalyst Development*

It is recommended to synthesize the photocatalyst (doped or non-doped) in order to achieve higher photoactivity, larger irradiated surface areas (porosity) and possibly visible light photoactivity.

c) *Analysis of Intermediate Species*

It is suggested to further analyze and measure all the intermediate species in the photodegradation of acetone and acetaldehyde. This will provide a complete kinetic analysis of these species' mineralization.

d) *Attack by \bullet OH radicals*

It is recommended to analyze the mechanisms involved during the attack of the \bullet OH radicals to the organic molecules.

e) *Industrial Case*

It is proposed to study an actual industrial case problem for the photodegradation of VOCs in a gas stream using the Photo-CREC-Air Reactor. It is suggested to analyze this case using the kinetic of the present study together with reactor and process simulation softwares.

f) *Cost Evaluation*

It is advised to perform an overall cost evaluation of the Photo-CREC-Air reactor. The cost evaluation requires including the operation costs of UV lamps and blower plus the material (photocatalyst and unit) costs.

References or Bibliography

- Adán, C., Marugán, J., Sánchez, E., Pablos, C., & van Grieken, R. (2016). Understanding the effect of morphology on the photocatalytic activity of TiO₂ nanotube array electrodes. *Electrochimica Acta*, *191*, 521-529. doi: <http://dx.doi.org/10.1016/j.electacta.2016.01.088>
- Aguado, S., Polo, A. C., Bernal, M. a. P., Coronas, J. n., & Santamaría, J. (2004). Removal of pollutants from indoor air using zeolite membranes. *Journal of Membrane Science*, *240*(1-2), 159-166. doi: <http://dx.doi.org/10.1016/j.memsci.2004.05.004>
- Arancibia-Bulnes, C. A., Jiménez, A. E., & Estrada, C. A. (2009). Development and Modeling of Solar Photocatalytic Reactors. In I. d. L. Hugo & R. Benito Serrano (Eds.), *Advances in Chemical Engineering* (Vol.36, pp. 185-227): Academic Press.
- Ballari, M. M., Carballada, J., Minen, R. I., Salvadores, F., Brouwers, H. J. H., Alfano, O. M., & Cassano, A. E. (2015a). Visible light TiO₂ photocatalysts assessment for air decontamination. *Process Safety and Environmental Protection*, *101*, 124-133. doi: <http://dx.doi.org/10.1016/j.psep.2015.08.003>
- Batault, F., Thevenet, F., Hequet, V., Rillard, C., Le Coq, L., & Locoge, N. (2015). Acetaldehyde and acetic acid adsorption on TiO₂ under dry and humid conditions. *Chemical Engineering Journal*, *264*, 197-210. doi: <http://dx.doi.org/10.1016/j.cej.2014.10.089>
- Bestetti, M., Sacco, D., Brunella, M. F., Franz, S., Amadelli, R., & Samiolo, L. (2010). Photocatalytic degradation activity of titanium dioxide sol-gel coatings on stainless steel wire meshes. *Materials Chemistry and Physics*, *124*(2-3), 1225-1231. doi: <http://dx.doi.org/10.1016/j.matchemphys.2010.08.062>
- Bettoni, M., Candori, P., Falcinelli, S., Marmottini, F., Meniconi, S., Rol, C., & Sebastiani, G. V. (2013). Gas phase photocatalytic efficiency of TiO₂ powders evaluated by acetone photodegradation. *Journal of Photochemistry and Photobiology A: Chemistry*, *268*, 1-6. doi: <http://dx.doi.org/10.1016/j.jphotochem.2013.06.014>
- Bianchi, C. L., Gatto, S., Pirola, C., Naldoni, A., Di Michele, A., Cerrato, G., Capucci, V. (2014). Photocatalytic degradation of acetone, acetaldehyde and toluene in gas-phase: Comparison between nano and micro-sized TiO₂. *Applied Catalysis B: Environmental*, *146*, 123-130. doi: <http://dx.doi.org/10.1016/j.apcatb.2013.02.047>
- Bolton, J. R., Safarzadeh-Amiri, A., & Cater, S. R. (1995). The detoxification of waste water streams using solar and artificial UV light sources. *Alternative Fuels and the Environment*, 187-192.

- Brown, S. K., Sim, M. R., Abramson, M. J., & Gray, C. N. (1994). Concentrations of Volatile Organic Compounds in Indoor Air – A Review. *Indoor Air*, 4(2), 123-134. doi: [10.1111/j.1600-0668.1994.t01-2-00007.x](https://doi.org/10.1111/j.1600-0668.1994.t01-2-00007.x)
- Byrne, J. A., Eggins, B. R., Brown, N. M. D., McKinney, B., & Rouse, M. (1998). Immobilisation of TiO₂ powder for the treatment of polluted water. *Applied Catalysis B: Environmental*, 17(1–2), 25-36. doi: [http://dx.doi.org/10.1016/S0926-3373\(97\)00101-X](http://dx.doi.org/10.1016/S0926-3373(97)00101-X)
- Cassano, A. E., Martin, C. A., Brandi R. J. & Alfano, O. M. (1995). Photoreactor Analysis and Design: Fundamentals and Applications. *Industrial Chemical Engineering Research*, 34(7), 2155-2201. doi: [10.1021/ie00046a001](https://doi.org/10.1021/ie00046a001)
- Chang, C.-P., Chen, J.-N., & Lu, M.-C. (2003). Heterogeneous Photocatalytic Oxidation of Acetone for Air Purification by Near UV-Irradiated Titanium Dioxide. *Journal of Environmental Science and Health, Part A*, 38(6), 1131-1143. doi: [10.1081/ESE-120019869](https://doi.org/10.1081/ESE-120019869)
- Chen, C. H., Kelder, E. M., & Schoonman, J. (1999). Electrostatic sol-spray deposition (ESSD) and characterisation of nanostructured TiO₂ thin films. *Thin Solid Films*, 342(1–2), 35-41. doi: [http://dx.doi.org/10.1016/S0040-6090\(98\)01160-2](http://dx.doi.org/10.1016/S0040-6090(98)01160-2)
- Choi, W., Ko, J. Y., Park, H., & Chung, J. S. (2001). Investigation on TiO₂-coated optical fibers for gas-phase photocatalytic oxidation of acetone. *Applied Catalysis B: Environmental*, 31(3), 209-220. doi: [http://dx.doi.org/10.1016/S0926-3373\(00\)00281-2](http://dx.doi.org/10.1016/S0926-3373(00)00281-2)
- Choi, W., Termin, A., & Hoffmann, M. R. (1994). The Role of Metal Ion Dopants in Quantum-Sized TiO₂: Correlation between Photoreactivity and Charge Carrier Recombination Dynamics. *The Journal of Physical Chemistry*, 98(51), 13669-13679. doi: [10.1021/j100102a038](https://doi.org/10.1021/j100102a038)
- Conde-Gallardo, A., Guerrero, M., Castillo, N., Soto, A. B., Fragoso, R., & Cabañas-Moreno, J. G. (2005). TiO₂ anatase thin films deposited by spray pyrolysis of an aerosol of titanium diisopropoxide. *Thin Solid Films*, 473(1), 68-73. doi: <http://dx.doi.org/10.1016/j.tsf.2004.07.010>
- Coronado, J. M., Zorn, M. E., Tejedor-Tejedor, I., & Anderson, M. A. (2003). Photocatalytic oxidation of ketones in the gas phase over TiO₂ thin films: a kinetic study on the influence of water vapor. *Applied Catalysis B: Environmental*, 43(4), 329-344. doi: [http://dx.doi.org/10.1016/S0926-3373\(03\)00022-5](http://dx.doi.org/10.1016/S0926-3373(03)00022-5)
- Dahmash, E. Z., & Mohammed, A. R. (2016). Characterisation and surface-profiling techniques for composite particles produced by dry powder coating in pharmaceutical drug delivery. *Drug Discovery Today*, 21(4), 550-561. doi: <http://dx.doi.org/10.1016/j.drudis.2015.11.013>

- Dawson, H. E., & McAlary, T. (2009). A Compilation of Statistics for VOCs from Post-1990 Indoor Air Concentration Studies in North American Residences Unaffected by Subsurface Vapor Intrusion. *Ground Water Monitoring & Remediation*, 29(1), 60-69. doi: [10.1111/j.1745-6592.2008.01215.x](https://doi.org/10.1111/j.1745-6592.2008.01215.x)
- de Lasa, H., Serrano, B., & Salaiques, M. (2005a). The Energy Efficiency Factors in Photocatalytic Processes *Photocatalytic Reaction Engineering* (pp. 119-131): Springer US.
- de Lasa, H., Serrano, B., & Salaiques, M. (2005b). Establishing Photocatalytic Kinetic Rate Equations: Basic Principles and Parameters *Photocatalytic Reaction Engineering* (pp. 1-15): Springer US.
- Debono, O., Thévenet, F., Gravejat, P., Héquet, V., Raillard, C., Le Coq, L., & Locoge, N. (2013). Gas phase photocatalytic oxidation of decane at ppb levels: Removal kinetics, reaction intermediates and carbon mass balance. *Journal of Photochemistry and Photobiology A: Chemistry*, 258, 17-29. doi: <http://dx.doi.org/10.1016/j.jphotochem.2013.02.022>
- Debono, O., Thevenet, F., Gravejat, P., Hequet, V., Raillard, C., Lecoq, L., & Locoge, N. (2011). Toluene photocatalytic oxidation at ppbv levels: Kinetic investigation and carbon balance determination. *Applied Catalysis B: Environmental*, 106(3-4), 600-608. doi: <http://dx.doi.org/10.1016/j.apcatb.2011.06.021>
- Dibble, L. A., & Raupp, G. B. (1992). Fluidized-bed photocatalytic oxidation of trichloroethylene in contaminated air streams. *Environmental Science & Technology*, 26(3), 492-495. doi: [10.1021/es00027a006](https://doi.org/10.1021/es00027a006)
- Dwivedi, P., Gaur, V., Sharma, A., & Verma, N. (2004). Comparative study of removal of volatile organic compounds by cryogenic condensation and adsorption by activated carbon fiber. *Separation and Purification Technology*, 39(1-2), 23-37. doi: <http://dx.doi.org/10.1016/j.seppur.2003.12.016>
- El-Maazawi, M., Finken, A. N., Nair, A. B., & Grassian, V. H. (2000). Adsorption and Photocatalytic Oxidation of Acetone on TiO₂: An in Situ Transmission FT-IR Study. *Journal of Catalysis*, 191(1), 138-146. doi: <http://dx.doi.org/10.1006/jcat.1999.2794>
- Environment and Climate Change Canada. (2008a). *Volatile Organic Compound (VOC) Concentration Limits for Architectural Coatings Regulations (SOR/2009-264)*. Canada: Canada Gazette.
- Environment and Climate Change Canada. (2008b). *Volatile Organic Compound (VOC) Concentration Limits for Automotive Refinishing Products Regulations SOR/2009-197*. Canada: Canada Gazette.
- Environment and Climate Change Canada. (2008c). *Volatile Organic Compound (VOC) Concentration Limits for Certain Products Regulations*. Canada: Canada Gazette.

- Environment and Climate Change Canada. (2016). *Canadian Environmental Sustainability Indicators: Air Pollutant Emissions*. Retrieved from http://www.ec.gc.ca/indicateurs-indicators/64B9E95D-5B44-42A8-98E2-7FBFED3CD6D2/Air%20Pollutant%20Emissions_EN.pdf.
- Estevan, C., Sogorb, M. A., & Vilanova, E. (2016) Air Quality of Textile and Related Industries *Comprehensive Analytical Chemistry*: Elsevier. doi:10.1016/bs.coac.2016.02.016
- Farhanian, D., & Haghghat, F. (2014). Photocatalytic oxidation air cleaner: Identification and quantification of by-products. *Building and Environment*, 72, 34-43. doi: <http://dx.doi.org/10.1016/j.buildenv.2013.10.014>
- Finlayson-Pitts, B. J., & Pitts Jr, J. N. (2000). Chapter 15 - Indoor Air Pollution: Sources, Levels, Chemistry, and Fates. *Chemistry of the Upper and Lower Atmosphere* (pp. 844-870). San Diego: Academic Press.
- Fox M. & Dulay M. (1993). Heterogeneous Photocatalysis. *Chemical Reviews*, 93, 341-357.
- Fujihara, K., Kumar, A., Jose, R., Ramakrishna, S., & Uchida, S. (2007). Spray deposition of electrospun TiO₂ nanorods for dye-sensitized solar cell. *Nanotechnology*, 18(36), 365709.
- Fujishima, A., Zhang, X., & Tryk, D. A. (2008). TiO₂ photocatalysis and related surface phenomena. *Surface Science Reports*, 63(12), 515-582. doi: <http://dx.doi.org/10.1016/j.surfrep.2008.10.001>
- Garcia-Hernandez, J. M. (2012). *Photocatalytic Reactors for Air Treatment: Energy Efficiencies and Kinetic Modeling*. (Doctor of Philosophy), University of Western Ontario, London, ON. Canada.
- Garcia-Hernandez, J. M., Rosales, B. S., & de Lasa, H. (2010). The photochemical thermodynamic efficiency factor (PTEF) in photocatalytic reactors for air treatment. *Chemical Engineering Journal*, 165(3), 891-901. doi: <http://dx.doi.org/10.1016/j.cej.2010.06.034>
- Garcia-Hernandez, J. M., Serrano-Rosales, B., & de Lasa, H. (2012). Energy Efficiencies in a Photo-CREC-Air Reactor: Conversion of Model Organic Pollutants in Air. *Industrial & Engineering Chemistry Research*, 51(16), 5715-5727. doi: [10.1021/ie300177p](http://dx.doi.org/10.1021/ie300177p)
- Gervasini, A., Vezzoli, G. C., & Ragaini, V. (1996). VOC removal by synergic effect of combustion catalyst and ozone. *Catalysis Today*, 29(1-4), 449-455. doi: [10.1016/0920-5861\(95\)00319-3](http://dx.doi.org/10.1016/0920-5861(95)00319-3)
- Giolli, C., Borgioli, F., Credi, A., Fabio, A. D., Fossati, A., Miranda, M. M., Bardi, U. (2007). Characterization of TiO₂ coatings prepared by a modified electric arc-

- physical vapour deposition system. *Surface and Coatings Technology*, 202(1), 13-22. doi: <http://dx.doi.org/10.1016/j.surfcoat.2007.04.043>
- Goldstein, A. H., & Galbally, I. E. (2007). Known and Unexplored Organic Constituents in the Earth's Atmosphere. *Environmental Science & Technology*, 41(5), 1514-1521. doi: [10.1021/es072476p](https://doi.org/10.1021/es072476p)
- Guenther, A. (1997). Seasonal and Spatial Variations in Natural Volatile Organic Compound Emissions. *Ecological Applications*, 7(1), 34-45. doi: [10.1890/1051-0761\(1997\)007\[0034:SASVIN\]2.0.CO;2](https://doi.org/10.1890/1051-0761(1997)007[0034:SASVIN]2.0.CO;2)
- Hager, S., Bauer, R., & Kudiella, G. (2000). Photocatalytic oxidation of gaseous chlorinated organics over titanium dioxide. *Chemosphere*, 41(8), 1219-1225. doi: [http://dx.doi.org/10.1016/S0045-6535\(99\)00558-5](http://dx.doi.org/10.1016/S0045-6535(99)00558-5)
- Han, Z., Chang, V. W., Zhang, L., Tse, M. S., Tan, O. K., & Hildemann, L. M. (2012). Preparation of TiO₂-coated polyester fiber filter by spray-coating and its photocatalytic degradation of gaseous formaldehyde. *Aerosol Air Qual. Res*, 12, 1327-1335.
- Hauchecorne, B., & Lenaerts, S. (2013). Unravelling the mysteries of gas phase photocatalytic reaction pathways by studying the catalyst surface: A literature review of different Fourier transform infrared spectroscopic reaction cells used in the field. *Journal of Photochemistry and Photobiology C: Photochemistry Reviews*, 14, 72-85. doi: <http://dx.doi.org/10.1016/j.jphotochemrev.2012.09.003>
- Hayes, R. E., Kolaczowski, S. T., & Thomas, W. J. (1992). An International Journal of Computer Applications in Chemical Engineering Finite-element model for a catalytic monolith reactor. *Computers & Chemical Engineering*, 16(7), 645-657. doi: [http://dx.doi.org/10.1016/0098-1354\(92\)80014-Z](http://dx.doi.org/10.1016/0098-1354(92)80014-Z)
- Hossain, M. M., Raupp, G. B., Hay, S. O., & Obee, T. N. (1999). Three-dimensional developing flow model for photocatalytic monolith reactors. *AIChE Journal*, 45(6), 1309-1321. doi: [10.1002/aic.690450615](https://doi.org/10.1002/aic.690450615)
- Hou, H., Miyafuji, H., & Saka, S. (2006). Photocatalytic activities and mechanism of the supercritically treated TiO₂-activated carbon composites on decomposition of acetaldehyde. *Journal of Materials Science*, 41(24), 8295-8300. doi: [10.1007/s10853-006-1009-4](https://doi.org/10.1007/s10853-006-1009-4)
- Hu, Y., Tsai, H. L., & Huang, C. L. (2003). Effect of brookite phase on the anatase-rutile transition in titania nanoparticles. *Journal of the European Ceramic Society*, 23(5), 691-696. doi: [http://dx.doi.org/10.1016/S0955-2219\(02\)00194-2](http://dx.doi.org/10.1016/S0955-2219(02)00194-2)
- Huang, P., Xu, N., Shi, J., & Lin, Y. S. (1997). Recovery of Volatile Organic Solvent Compounds from Air by Ceramic Membranes. *Industrial & Engineering Chemistry Research*, 36(9), 3815-3820. doi: [10.1021/ie960760b](https://doi.org/10.1021/ie960760b)

- Hulin, M., Simoni, M., Viegi, G., & Annesi-Maesano, I. (2012). Respiratory health and indoor air pollutants based on quantitative exposure assessments. *European Respiratory Journal*, 40(4), 1033-1045.
- Hussain, A., Gracia, J., Nieuwenhuys, B. E., & Niemantsverdriet, J. W. (2010). Chemistry of O- and H-Containing Species on the (001) Surface of Anatase TiO₂: A DFT Study. *ChemPhysChem*, 11(11), 2375-2382. doi: [10.1002/cphc.201000185](https://doi.org/10.1002/cphc.201000185)
- Ibrahim, H. (2001). *Photo Catalytic Reactor for the Degradation of Airborne Pollutants: Photo Conversion Efficiency and Kinetic Modeling*. (Doctor of Philosophy), University of Western Ontario, London, Canada.
- Ibrahim, H., & de Lasa, H. (1999). Novel Photocatalytic Reactor for the Destruction of Airborne Pollutants Reaction Kinetics and Quantum Yields. *Industrial & Engineering Chemistry Research*, 38(9), 3211-3217. doi: [10.1021/ie980712m](https://doi.org/10.1021/ie980712m)
- Ibrahim, H., & de Lasa, H. (2002). Photo-catalytic conversion of air borne pollutants: Effect of catalyst type and catalyst loading in a novel photo-CREC-air unit. *Applied Catalysis B: Environmental*, 38(3), 201-213. doi: [http://dx.doi.org/10.1016/S0926-3373\(02\)00043-7](http://dx.doi.org/10.1016/S0926-3373(02)00043-7)
- Ibrahim, H., & de Lasa, H. (2003). Photo-catalytic degradation of air borne pollutants apparent quantum efficiencies in a novel photo-CREC-air reactor. *Chemical Engineering Science*, 58(3-6), 943-949. doi: [http://dx.doi.org/10.1016/S0009-2509\(02\)00632-2](http://dx.doi.org/10.1016/S0009-2509(02)00632-2)
- Ibrahim, H., & de Lasa, H. (2004). Kinetic modeling of the photocatalytic degradation of air-borne pollutants. *AIChE Journal*, 50(5), 1017-1027. doi: [10.1002/aic.10097](https://doi.org/10.1002/aic.10097)
- Iranpour, R., Cox, H. H. J., Deshusses, M. A., & Schroeder, E. D. (2005). Literature review of air pollution control biofilters and biotrickling filters for odor and volatile organic compound removal. *Environmental Progress*, 24(3), 254-267. doi: [10.1002/ep.10077](https://doi.org/10.1002/ep.10077)
- Iskandar, F., Gradon, L., & Okuyama, K. (2003). Control of the morphology of nanostructured particles prepared by the spray drying of a nanoparticle sol. *Journal of Colloid and Interface Science*, 265(2), 296-303. doi: [http://dx.doi.org/10.1016/S0021-9797\(03\)00519-8](http://dx.doi.org/10.1016/S0021-9797(03)00519-8)
- Jacoby, W. A., Blake, D. M., Noble, R. D., & Koval, C. A. (1995). Kinetics of the Oxidation of Trichloroethylene in Air via Heterogeneous Photocatalysis. *Journal of Catalysis*, 157(1), 87-96. doi: <http://dx.doi.org/10.1006/jcat.1995.1270>
- Jung, D. S., Hwang, T. H., Park, S. B., & Choi, J. W. (2013). Spray Drying Method for Large-Scale and High-Performance Silicon Negative Electrodes in Li-Ion Batteries. *Nano Letters*, 13(5), 2092-2097. doi: [10.1021/nl400437f](https://doi.org/10.1021/nl400437f)

- Khan, F. I., & Kr. Ghoshal, A. (2000). Removal of Volatile Organic Compounds from polluted air. *Journal of Loss Prevention in the Process Industries*, 13(6), 527-545. doi: [10.1016/S0950-4230\(00\)00007-3](https://doi.org/10.1016/S0950-4230(00)00007-3)
- Kim, D.-J., Kang, J.-Y., & Kim, K.-S. (2010). Coating of TiO₂ thin films on particles by a plasma chemical vapor deposition process. *Advanced Powder Technology*, 21(2), 136-140. doi: <http://dx.doi.org/10.1016/j.apt.2009.12.014>
- Kim, H. J., Nah, S. S., & Min, B. R. (2002). A new technique for preparation of PDMS pervaporation membrane for VOC removal. *Advances in Environmental Research*, 6(3), 255-264. doi: [http://dx.doi.org/10.1016/S1093-0191\(01\)00056-9](http://dx.doi.org/10.1016/S1093-0191(01)00056-9)
- Kisch, H., & Bahnemann, D. (2015). Best Practice in Photocatalysis: Comparing Rates or Apparent Quantum Yields? *The Journal of Physical Chemistry Letters*, 6(10), 1907-1910. doi: [10.1021/acs.jpcllett.5b00521](https://doi.org/10.1021/acs.jpcllett.5b00521)
- Krämer, A., Kunz, C., Gräf, S., & Müller, F. A. (2015). Pulsed laser deposition of anatase thin films on textile substrates. *Applied Surface Science*, 353, 1046-1051. doi: <http://dx.doi.org/10.1016/j.apsusc.2015.07.055>
- Le Behec, M., Kinadjian, N., Ollis, D., Backov, R., & Lacombe, S. (2015). Comparison of kinetics of acetone, heptane and toluene photocatalytic mineralization over TiO₂ microfibers and Quartzel® mats. *Applied Catalysis B: Environmental*, 179, 78-87. doi: <http://dx.doi.org/10.1016/j.apcatb.2015.05.015>
- Lee, D. Y., Kim, J.-T., Park, J.-H., Kim, Y.-H., Lee, I.-K., Lee, M.-H., & Kim, B.-Y. (2013). Effect of Er doping on optical band gap energy of TiO₂ thin films prepared by spin coating. *Current Applied Physics*, 13(7), 1301-1305. doi: <http://dx.doi.org/10.1016/j.cap.2013.03.025>
- Li, X., Anton, N., Arpagaus, C., Belleteix, F., & Vandamme, T. F. (2010). Nanoparticles by spray drying using innovative new technology: The Büchi Nano Spray Dryer B-90. *Journal of Controlled Release*, 147(2), 304-310. doi: <http://dx.doi.org/10.1016/j.jconrel.2010.07.113>
- Li, X. Z., Liu, H., Cheng, L. F., & Tong, H. J. (2003). Photocatalytic Oxidation Using a New Catalyst TiO₂ Microspherfor Water and Wastewater Treatment. *Environmental Science & Technology*, 37(17), 3989-3994. doi: [10.1021/es0262941](https://doi.org/10.1021/es0262941)
- Lin, C.-C., Liu, W.-T., & Tan, C.-S. (2003). Removal of Carbon Dioxide by Absorption in a Rotating Packed Bed. *Industrial & Engineering Chemistry Research*, 42(11), 2381-2386. doi: [10.1021/ie020669+](https://doi.org/10.1021/ie020669+)
- Lopez, L., Daoud, W. A., Dutta, D., Panther, B. C., & Turney, T. W. (2013). Effect of substrate on surface morphology and photocatalysis of large-scale TiO₂ films. *Applied Surface Science*, 265, 162-168. doi: <http://dx.doi.org/10.1016/j.apsusc.2012.10.156>

- Lugo Vega, C. S., Serrano-Rosales, B., & de Lasa, H. (2016). Immobilized Particle Coating for Optimum Photon And TiO₂ Utilization in Scaled Air Treatment Reactors. *Applied Catalysis B: Environmental*, 198, 211-223.
- Maleki-Ghaleh, H., Shahzadeh, M., Hoseinizadeh, S. A., Arabi, A., Aghaie, E., & Siadati, M. h. Evaluation of the photo-electro-catalytic behavior of Nano-structured ZnO films fabricated by electrodeposition process. *Materials Letters*. doi: <http://dx.doi.org/10.1016/j.matlet.2016.01.090>
- Marugán, J., van Grieken, R., Pablos, C., Satuf, M. L., Cassano, A. E., & Alfano, O. M. (2013). Modeling of a bench-scale photocatalytic reactor for water disinfection from laboratory-scale kinetic data. *Chemical Engineering Journal*, 224, 39-45. doi: <http://dx.doi.org/10.1016/j.cej.2012.11.082>
- Mehrvar, M., Anderson, W. A., & Moo-Young, M. (2002). Preliminary analysis of a tellerette packed-bed photocatalytic reactor. *Advances in Environmental Research*, 6(4), 411-418. doi: [http://dx.doi.org/10.1016/S1093-0191\(01\)00068-5](http://dx.doi.org/10.1016/S1093-0191(01)00068-5)
- Mo, J., Zhang, Y., Xu, Q., Lamson, J. J., & Zhao, R. (2009). Photocatalytic purification of volatile organic compounds in indoor air: A literature review. *Atmospheric Environment*, 43(14), 2229-2246. doi: <http://dx.doi.org/10.1016/j.atmosenv.2009.01.034>
- Mo, Z., Shao, M., Lu, S., Qu, H., Zhou, M., Sun, J., & Gou, B. (2015). Process-specific emission characteristics of volatile organic compounds (VOCs) from petrochemical facilities in the Yangtze River Delta, China. *Science of The Total Environment*, 533, 422-431. doi: <http://dx.doi.org/10.1016/j.scitotenv.2015.06.089>
- Momeni, M., Golestani-Fard, F., Saghafian, H., Barati, N., & Khanahmadi, A. (2015). Development of visible light activated TiO₂ thin films on stainless steel via sol spraying with emphasis on microstructural evolution and photocatalytic activity. *Applied Surface Science*, 357, Part B, 1902-1910. doi: <http://dx.doi.org/10.1016/j.apsusc.2015.09.122>
- Moreira, J., Serrano, B., Ortiz, A., & de Lasa, H. (2012). A unified kinetic model for phenol photocatalytic degradation over TiO₂ photocatalysts. *Chemical Engineering Science*, 78, 186-203. doi: <http://dx.doi.org/10.1016/j.ces.2012.04.033>
- Muñoz-Batista, M. J., Kubacka, A., Hungría, A. B., & Fernández-García, M. (2015). Heterogeneous photocatalysis: Light-matter interaction and chemical effects in quantum efficiency calculations. *Journal of Catalysis*, 330, 154-166. doi: <http://dx.doi.org/10.1016/j.jcat.2015.06.021>
- Noguchi, T., Fujishima, A., Sawunyama, P., & Hashimoto, K. (1998). Photocatalytic Degradation of Gaseous Formaldehyde Using TiO₂ Film. *Environmental Science & Technology*, 32(23), 3831-3833. doi: [10.1021/es980299+](https://doi.org/10.1021/es980299+)

- Nolan, N. T., Seery, M. K., & Pillai, S. C. (2009). Spectroscopic Investigation of the Anatase-to-Rutile Transformation of Sol–Gel-Synthesized TiO₂ Photocatalysts. *The Journal of Physical Chemistry C*, 113(36), 16151-16157. doi: [10.1021/jp904358g](https://doi.org/10.1021/jp904358g)
- Obee, T. N. (1996). Photooxidation of Sub-Parts-per-Million Toluene and Formaldehyde Levels on Titania Using a Glass-Plate Reactor. *Environmental Science & Technology*, 30(12), 3578-3584. doi: [10.1021/es9602713](https://doi.org/10.1021/es9602713)
- Okuyama, K., & Wuled Lenggoro, I. (2003). Preparation of nanoparticles via spray route. *Chemical Engineering Science*, 58(3–6), 537-547. doi: [http://dx.doi.org/10.1016/S0009-2509\(02\)00578-X](http://dx.doi.org/10.1016/S0009-2509(02)00578-X)
- Ong, W. L., & Ho, G. W. (2016). Enhanced Photocatalytic Performance of TiO₂ Hierarchical Spheres Decorated with Ag₂S Nanoparticles. *Procedia Engineering*, 141, 7-14. doi: <http://dx.doi.org/10.1016/j.proeng.2015.09.217>
- Ortiz-Gomez, A., Serrano-Rosales, B., Salaires, M., & de Lasa, H. (2007). Photocatalytic Oxidation of Phenol: Reaction Network, Kinetic Modeling, and Parameter Estimation. *Industrial & Engineering Chemistry Research*, 46(23), 7394-7409. doi: [10.1021/ie0611960](https://doi.org/10.1021/ie0611960)
- Palmisano, G., Loddo, V., Augugliaro, V., Bellardita, M., Camera Roda, G., & Parrino, F. (2015). Validation of a two-dimensional modeling of an externally irradiated slurry photoreactor. *Chemical Engineering Journal*, 262, 490-498. doi: <http://dx.doi.org/10.1016/j.cej.2014.10.013>
- Palmisano, G., Scandura, G., Augugliaro, V., Loddo, V., Pace, A., Tek, B. S., Palmisano, L. (2015). Unexpectedly ambivalent O₂ role in the autocatalytic photooxidation of 2-methoxybenzyl alcohol in water. *Journal of Molecular Catalysis A: Chemical*, 403, 37-42. doi: <http://dx.doi.org/10.1016/j.molcata.2015.03.021>
- Paz, Y. (2010). Application of TiO₂ photocatalysis for air treatment: Patents' overview. *Applied Catalysis B: Environmental*, 99(3–4), 448-460. doi: <http://dx.doi.org/10.1016/j.apcatb.2010.05.011>
- Pelaez, M., Nolan, N. T., Pillai, S. C., Seery, M. K., Falaras, P., Kontos, A. G., Dionysiou, D. D. (2012). A review on the visible light active titanium dioxide photocatalysts for environmental applications. *Applied Catalysis B: Environmental*, 125, 331-349. doi: <http://dx.doi.org/10.1016/j.apcatb.2012.05.036>
- Peral, J., & Ollis, D. F. (1992). Heterogeneous photocatalytic oxidation of gas-phase organics for air purification: Acetone, 1-butanol, butyraldehyde, formaldehyde, and m-xylene oxidation. *Journal of Catalysis*, 136(2), 554-565. doi: [http://dx.doi.org/10.1016/0021-9517\(92\)90085-V](http://dx.doi.org/10.1016/0021-9517(92)90085-V)
- Pun, B. K., Wu, S.-Y., & Seigneur, C. (2002). Contribution of Biogenic Emissions to the Formation of Ozone and Particulate Matter in the Eastern United States.

Environmental Science & Technology, 36(16), 3586-3596. doi:
[10.1021/es015872v](https://doi.org/10.1021/es015872v)

- Raupp, G. B., & Junio, C. T. (1993). Photocatalytic oxidation of oxygenated air toxics. *Applied Surface Science*, 72(4), 321-327. doi: [http://dx.doi.org/10.1016/0169-4332\(93\)90369-M](http://dx.doi.org/10.1016/0169-4332(93)90369-M)
- Riffat, S. B., & Zhao, X. (2007). Preliminary study of the performance and operating characteristics of a mop-fan air cleaning system for buildings. *Building and Environment*, 42(9), 3241-3252. doi: <http://dx.doi.org/10.1016/j.buildenv.2006.07.038>
- Romero-Vargas Castrillón, S., & de Lasa, H. I. (2007). Performance Evaluation of Photocatalytic Reactors for Air Purification Using Computational Fluid Dynamics (CFD). *Industrial & Engineering Chemistry Research*, 46(18), 5867-5880. doi: [10.1021/ie060696q](https://doi.org/10.1021/ie060696q)
- Sakthivel, S., Shankar, M. V., Palanichamy, M., Arabindoo, B., Bahnemann, D. W., & Murugesan, V. (2004). Enhancement of photocatalytic activity by metal deposition: characterisation and photonic efficiency of Pt, Au and Pd deposited on TiO₂ catalyst. *Water Research*, 38(13), 3001-3008. doi: <http://dx.doi.org/10.1016/j.watres.2004.04.046>
- Salaices, M., Serrano, B., & de Lasa, H. I. (2004). Photocatalytic conversion of phenolic compounds in slurry reactors. *Chemical Engineering Science*, 59(1), 3-15. doi: <http://dx.doi.org/10.1016/j.ces.2003.07.015>
- Salvadores, F., Minen, R. I., Carballada, J., Alfano, O. M., & Ballari, M. M. (2016). Kinetic Study of Acetaldehyde Degradation Applying Visible Light Photocatalysis. *Chemical Engineering & Technology*, 39(1), 166-174. doi: [10.1002/ceat.201500507](https://doi.org/10.1002/ceat.201500507)
- Sauer, M. L., & Ollis, D. F. (1994). Acetone Oxidation in a Photocatalytic Monolith Reactor. *Journal of Catalysis*, 149(1), 81-91. doi: <http://dx.doi.org/10.1006/jcat.1994.1274>
- Sauer, M. L., & Ollis, D. F. (1996). Photocatalyzed Oxidation of Ethanol and Acetaldehyde in Humidified Air. *Journal of Catalysis*, 158(2), 570-582. doi: <http://dx.doi.org/10.1006/jcat.1996.0055>
- Serpone, N. (1997). Relative photonic efficiencies and quantum yields in heterogeneous photocatalysis. *Journal of Photochemistry and Photobiology A: Chemistry*, 104(1-3), 1-12. doi: [http://dx.doi.org/10.1016/S1010-6030\(96\)04538-8](http://dx.doi.org/10.1016/S1010-6030(96)04538-8)
- Serpone, N., & Pelizzetti, E. (1989). Adsorption-desorption, related mobility and reactivity in photocatalysis *Photocatalysis: Fundamentals and Applications* (pp. 217-250). New York: Wiley.

- Serrano, B., & de Lasa, H. (1997). Photocatalytic Degradation of Water Organic Pollutants. Kinetic Modeling and Energy Efficiency. *Industrial & Engineering Chemistry Research*, 36(11), 4705-4711. doi: [10.1021/ie970104r](https://doi.org/10.1021/ie970104r)
- Shan, A. Y., Ghazi, T. I. M., & Rashid, S. A. (2010). Immobilisation of titanium dioxide onto supporting materials in heterogeneous photocatalysis: A review. *Applied Catalysis A: General*, 389(1-2), 1-8. doi: <http://dx.doi.org/10.1016/j.apcata.2010.08.053>
- Shareefdeen, Z., Taqvi, S., & Elkamel, A. (2016). Air Quality Management in Electronic Industries *Comprehensive Analytical Chemistry*, 73, 765-784.
- Smith, C. M., & Brown, W. E. (1993). Elimination of VOC Emissions from Surface Coating Operations. *Air & Waste*, 43(7), 1015-1019. doi: [10.1080/1073161X.1993.10467175](https://doi.org/10.1080/1073161X.1993.10467175)
- Sopyan, I. (2007). Kinetic analysis on photocatalytic degradation of gaseous acetaldehyde, ammonia and hydrogen sulfide on nanosized porous TiO₂ films. *Science and Technology of Advanced Materials*, 8(1-2), 33-39. doi: <http://dx.doi.org/10.1016/j.stam.2006.10.004>
- Spivey, J. J. (1987). Complete catalytic oxidation of volatile organics. *Industrial & Engineering Chemistry Research*, 26(11), 2165-2180. doi: [10.1021/ie00071a001](https://doi.org/10.1021/ie00071a001)
- Šuligoj, A., Štangar, U. L., Ristić, A., Mazaj, M., Verhovšek, D., & Tušar, N. N. (2016). TiO₂-SiO₂ films from organic-free colloidal TiO₂ anatase nanoparticles as photocatalyst for removal of volatile organic compounds from indoor air. *Applied Catalysis B: Environmental*, 184, 119-131. doi: <http://dx.doi.org/10.1016/j.apcatb.2015.11.007>
- Thiruvengkatachari, R., Vigneswaran, S., & Moon, I. S. (2008). A review on UV/TiO₂ photocatalytic oxidation process (Journal Review). *Korean Journal of Chemical Engineering*, 25(1), 64-72. doi: [10.1007/s11814-008-0011-8](https://doi.org/10.1007/s11814-008-0011-8)
- Tompkins, D. T., Lawnicki, B. J., Zeltner, W. A., & Anderson, M. A. (2005). Evaluation of photocatalysis for gas-phase air cleaning—Part 1: Process, technical and sizing considerations. *Ashrae Transactions*, 111(2), 60-84.
- Traid, H. D., Vera, M. L., Ares, A. E., & Litter, M. I. (2015). Porous Titanium Dioxide Coatings Obtained by Anodic Oxidation for Photocatalytic Applications. *Procedia Materials Science*, 9, 619-626. doi: <http://dx.doi.org/10.1016/j.mspro.2015.05.038>
- Turchi, C. S., & Ollis, D. F. (1990). Photocatalytic degradation of organic water contaminants: Mechanisms involving hydroxyl radical attack. *Journal of Catalysis*, 122(1), 178-192. doi: [http://dx.doi.org/10.1016/0021-9517\(90\)90269-P](http://dx.doi.org/10.1016/0021-9517(90)90269-P)

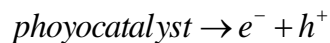
- U.S. Environmental Protection Agency. (1989). *Assesment and Control of Indoor Air Pollution*. (EPA 400-1-89-001C). Washington D.C.
- U.S. Environmental Protection Agency. (2008). *National Emission Standards for Hazardous Air Pollutants: Area Source Standards for Nine Metal Fabrication and Finishing Source Categories; Final Rule*. (40 CFR Part 63). Retrieved from <https://www3.epa.gov/airtoxics/area/fr23jy08.pdf>.
- Valades-Pelayo, P. (2014). *Scale-up Methodology for Bench-Scale Slurry Photocatalytic Reactors using combined Irradiation and Kinetic Modeling*. (PhD in Chemical and Biochemical Engineering), University of Western Ontario, London, Canada. (Paper 2528)
- Valadés-Pelayo, P. J., Guayaquil Sosa, F., Serrano, B., & de Lasa, H. (2015a). Eight-lamp externally irradiated bench-scale photocatalytic reactor: Scale-up and performance prediction. *Chemical Engineering Journal*, 282, 142-151. doi: <http://dx.doi.org/10.1016/j.cej.2015.03.039>
- Valadés-Pelayo, P. J., Guayaquil Sosa, F., Serrano, B., & de Lasa, H. (2015b). Photocatalytic reactor under different external irradiance conditions: Validation of a fully predictive radiation absorption model. *Chemical Engineering Science*, 126, 42-54. doi: <http://dx.doi.org/10.1016/j.ces.2014.12.003>
- Valadés-Pelayo, P. J., Moreira del Rio, J., Solano-Flores, P., Serrano, B., & de Lasa, H. (2014). Establishing photon absorption fields in a Photo-CREC Water II Reactor using a CREC-spectroradiometric probe. *Chemical Engineering Science*, 116, 406-417. doi: <http://dx.doi.org/10.1016/j.ces.2014.04.041>
- Valades-Pelayo, P. J., Moreira, J., Serrano, B., & de Lasa, H. (2014). Boundary conditions and phase functions in a Photo-CREC Water-II reactor radiation field. *Chemical Engineering Science*, 107, 123-136. doi: <http://dx.doi.org/10.1016/j.ces.2013.12.013>
- Valladares, J. & Bolton J. (1993). A Method for the Determination of Quantum Yields in Heterogeneous Systems: the Titanium Dioxide Photocatalyzed Bleaching of Methylene Blue.. *Trace Metals in the Enviornment*, 3, 111-120.
- Verbruggen, S. W., Deng, S., Kurttepli, M., Cott, D. J., Vereecken, P. M., Bals, S., . . . Lenaerts, S. (2014). Photocatalytic acetaldehyde oxidation in air using spacious TiO₂ films prepared by atomic layer deposition on supported carbonaceous sacrificial templates. *Applied Catalysis B: Environmental*, 160–161, 204-210. doi: <http://dx.doi.org/10.1016/j.apcatb.2014.05.029>
- Wallace, L. A. (1987). *The Total Exposure Assesment Methodology (TEAM) Study*. (EPA-600-S6-87-002). Washington D.C.
- Wang, W., Yu, J., Xiang, Q., & Cheng, B. (2012). Enhanced photocatalytic activity of hierarchical macro/mesoporous TiO₂-graphene composites for photodegradation

- of acetone in air. *Applied Catalysis B: Environmental*, 119–120, 109–116. doi: <http://dx.doi.org/10.1016/j.apcatb.2012.02.035>
- WHO. (1999). *Monitoring ambient air quality for health impact assessment*. Copenhagen: WHO Regional Publications.
- Wiederkehr, P. (1994). Emission reduction programmes for VOC in some OECD countries. In J. H. S. Vigneron & J. Chaouki (Eds.), *Studies in Environmental Science* (Vol. 61, pp. 11–28): Elsevier.
- Xu, Y., & Langford, C. H. (2000). Variation of Langmuir adsorption constant determined for TiO₂-photocatalyzed degradation of acetophenone under different light intensity. *Journal of Photochemistry and Photobiology A: Chemistry*, 133(1–2), 67–71. doi: [http://dx.doi.org/10.1016/S1010-6030\(00\)00220-3](http://dx.doi.org/10.1016/S1010-6030(00)00220-3)
- Zazueta, A. L. L., Destailats, H., & Li Puma, G. (2013). Radiation field modeling and optimization of a compact and modular multi-plate photocatalytic reactor (MPPR) for air/water purification by Monte Carlo method. *Chemical Engineering Journal*, 217, 475–485. doi: <http://dx.doi.org/10.1016/j.cej.2012.11.085>
- Zhang, L., & Anderson, W. A. (2013). Kinetic analysis of the photochemical decomposition of gas-phase chlorobenzene in a UV reactor: Quantum yield and photonic efficiency. *Chemical Engineering Journal*, 218, 247–252. doi: <http://dx.doi.org/10.1016/j.cej.2012.12.004>
- Zhang, L., Mohamed, H. H., Dillert, R., & Bahnemann, D. (2012). Kinetics and mechanisms of charge transfer processes in photocatalytic systems: A review. *Journal of Photochemistry & Photobiology, C: Photochemistry Reviews*, 13(4), 263–276. doi: 10.1016/j.jphotochemrev.2012.07.002
- Zhao, J., & Yang, X. (2003). Photocatalytic oxidation for indoor air purification: a literature review. *Building and Environment*, 38(5), 645–654. doi: [http://dx.doi.org/10.1016/S0360-1323\(02\)00212-3](http://dx.doi.org/10.1016/S0360-1323(02)00212-3)
- Zhao, X. S., Ma, Q., & Lu, G. Q. (1998). VOC Removal: Comparison of MCM-41 with Hydrophobic Zeolites and Activated Carbon. *Energy & Fuels*, 12(6), 1051–1054. doi: [10.1021/ef980113s](http://dx.doi.org/10.1021/ef980113s)
- Zhao, Z., Sun, J., Zhang, G., & Bai, L. (2015). The study of microstructure, optical and photocatalytic properties of nanoparticles(NPs)-Cu/TiO₂ films deposited by magnetron sputtering. *Journal of Alloys and Compounds*, 652, 307–312. doi: <http://dx.doi.org/10.1016/j.jallcom.2015.08.117>

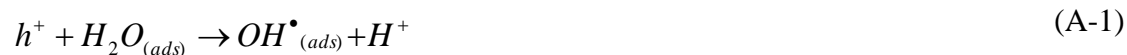
Appendices

Appendix A: Proposed Mechanism of OH^\bullet Radical Formation

A photocatalytic oxidation reaction takes place once a photon hits a semiconductor surface.



Physisorbed H_2O or chemisorbed OH^\bullet can react with the h^+ holes at the surface of the photocatalyst and the following occurs:



On the other hand, molecular oxygen can react with the electrons in the conduction band:



This $O_2^{\bullet-}$ super oxide ion can react with water producing more OH^\bullet radicals:



A linear combination of the mechanism presented above leads to the following stoichiometry:



According with this stoichiometry, 3 photons can produce 4 hydroxyl radicals. This would yield an ideal $4 OH^\bullet / 3 hv$ equivalent to a maximum QY of 133%.

Appendix B: Effect of the Air Pressure in the TiO₂ Slurry Volumetric Flow and Selected AAS Conditions.

The operation parameters for the Air Assisted Spray were experimentally determined. Air Pressure plays a very important role on the TiO₂ immobilization, since it has an effect on the droplet size, impact velocity and slurry flow rate. Figure 61 shows the effect of the Air Pressure on the Impacted TiO₂ slurry flow. One can also see the higher degree of experimental error when the pressure is low. On the other hand, when operating with air pressures after 30 psia, big droplets were formed on the mesh.

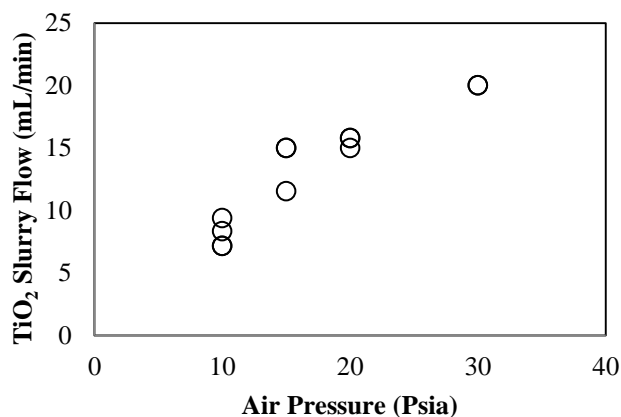


Figure 61: Effect of the Air Pressure in the Atomized TiO₂ Slurry Flow

Therefore, it was selected 20 psia air pressure and 15.7 ml/min of 16wt% TiO₂ atomized slurry solution (12 RPM, 1.31 mL per drum revolution). The mesh was sprayed with one revolution slurry flow for each axial step of 2 cm. On this basis, the expected TiO₂ mass sprayed on the mesh is 5.85 gr. The actual amount of Titanium Dioxide deposited on the mesh as established via gravimetry was however, 2.2 gr (1% wt TiO₂) on a 1220 cm² stainless steel wire mesh surface. This shows that the AAS-ASC method displays an impregnation efficiency of 38%, with the resulting coating being both homogenous and free of agglomerates.

Appendix C: Spectral Intensity and Radiation Distribution of the UV Lamps

A polychromatic EiKO Global Lamp was used in the present study. Figure 62 shows the distribution of spectral emitted intensity in the 325nm to 410nm range with a radiation peak at 350 nm. Given that only photons with a wavelength smaller than 368nm activate TiO_2 , only 94% of the photons emitted by this lamp activate the TiO_2 (grey shaded area in Figure 62) (Thiruvengkatachari, Vigneswaran, & Moon, 2008). One should also note that consistent with the data of Figure 62, only the fraction of absorbed photons with wavelengths below 386nm (gray area) shall be used in the Quantum Yield calculations, with this being in agreement with eq. (6.6)

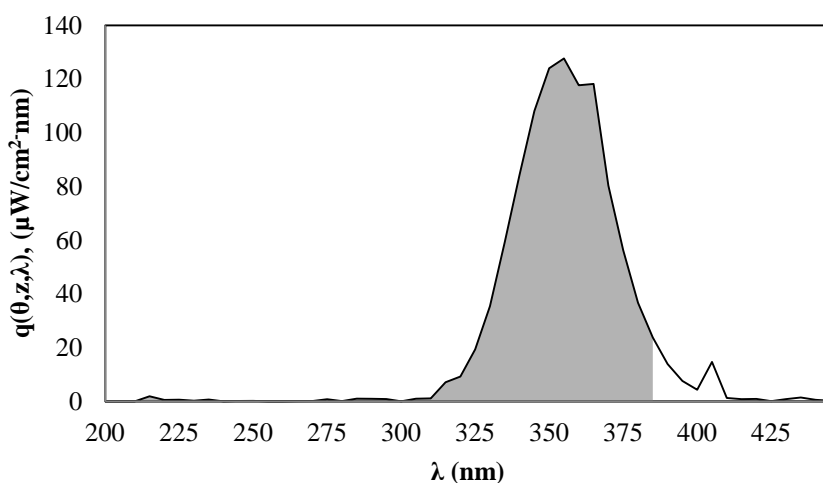


Figure 62: Spectral Intensity of a Polychromatic EiKO Global UV Lamp.

.Appendix D: Calibration of the Periscopic Device with Optic Probe

The periscopic device consists in aluminum housing with polished walls (refer to Section 4.4) in order to measure the radiation 90° in respect with the optic probe. However, a percentage of the radiation reaching the periscopic device could be diffused or absorbed by the aluminum and therefore, it is not measured by the optic probe. Hence, the radiation measurements using the periscopic device require to be calibrated. The periscopic device was calibrated for these two cases: 1) 1 in long housing and 2) $\frac{3}{4}$ in long housing. Measurements for incident and transmitted radiation were performed with 1 in long

housing and for reflected with $\frac{3}{4}$ in long. Figure 63 reports the calibration of the 1 in housing periscopic device. The calibration was completed using one reflector and two 15 W lamps. Locations of the measurements were: a) 1.3 cm b) 2.8 cm and c) 6.3 cm away from the lamps at different x,y plane positions.

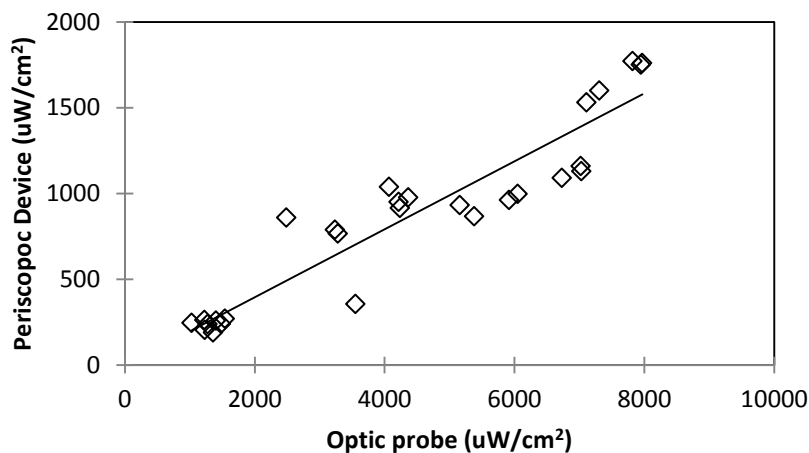


Figure 63: Calibration of the Periscopic Device in respect with the Optic Probe

Table 18 reports the calculated slopes from the calibration measurements. The radiation measured in the Photo-CREC-Air reactor using the periscopic device was then multiplied by the corresponding factor in order to obtain the real radiation flux.

Table 18. Calibration slopes for the periscopic device

Housing length	Slope (Periscopic device/Optic Probe)
1 in	1/5
$\frac{3}{4}$ in	1/3

Appendix E: GC Parameters, Chromatograms and Calibration Curves

An adequate GC program method was used in order to separate and measure acetone, acetaldehyde, formaldehyde, methanol and CO₂ using a packed Poropak Q column, FID

detector and a methanizer. Figure 64 and table 19 report the parameters and conditions used in this GC program method.

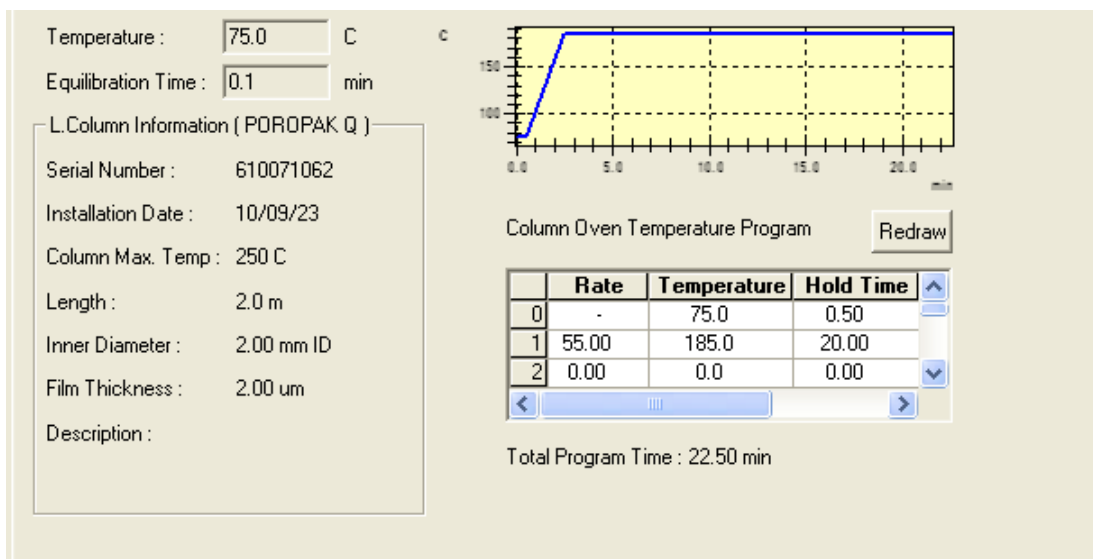


Figure 64: GC parameters of the column separation method

Table 19. GC parameters of Injection and Detection

Injection	Helium Flow	10 mL/min
	Temperature	125 °C
Porapak Q	Column Length	2 m
	Inner Diameter	2 mm ID
FID	Temperature	125 °C
	Sampling Rate	40 msec
	Stop time	14 min
	Delay time	0 min
	Substract Detector	None
Methanizer	Temperature	380 C

Figures 65 and 66 are examples of the FID chromatograms obtained during the photodegradation of acetone and acetaldehyde using the described method above. The samples were injected using an automatic system with a 8 position valve. This also made possible to automatize the sampling time (Figures 67 and 68).

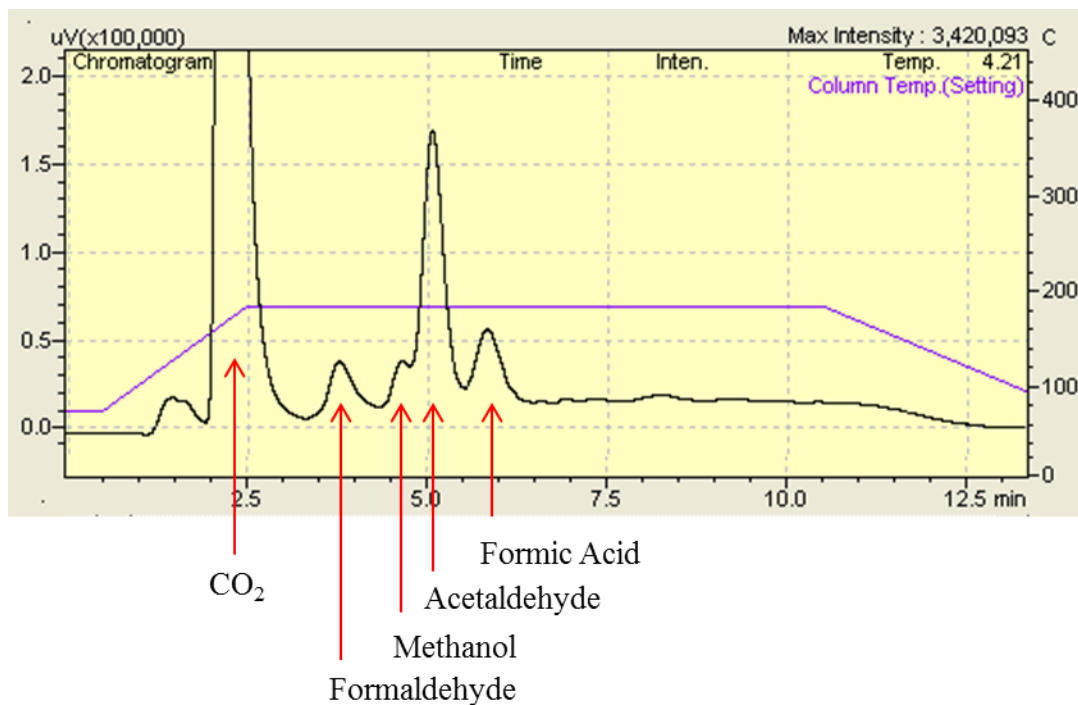


Figure 65: Chromatogram obtained during the photodegradation of acetaldehyde in the Photo-CREC-Air reactor.

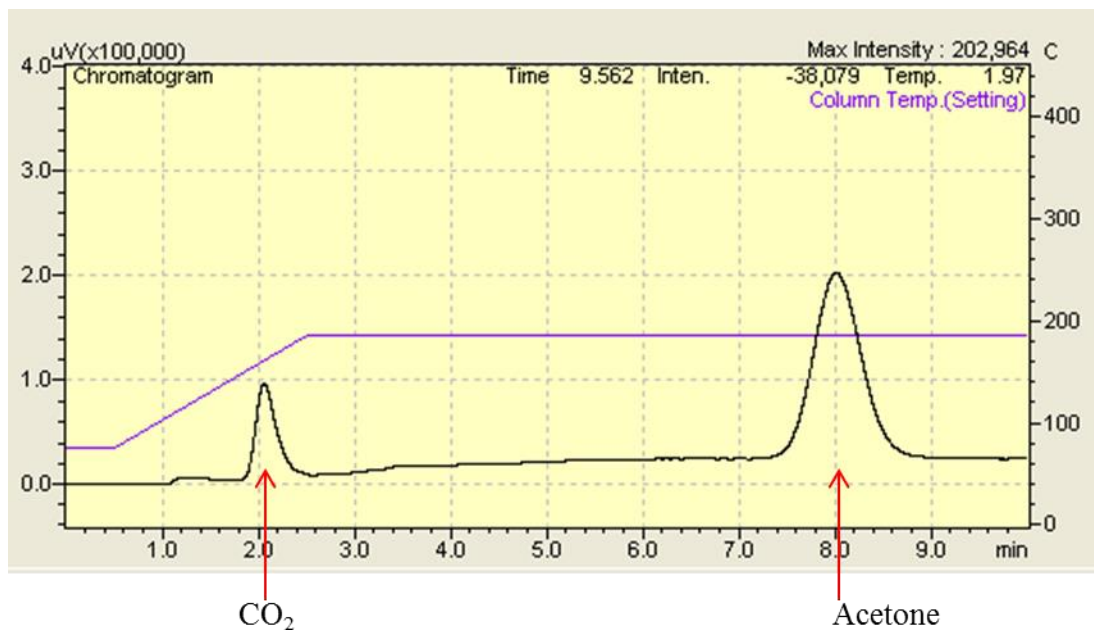


Figure 66: Chromatogram obtained during the photodegradation of acetone in the Photo-CREC-Air reactor.

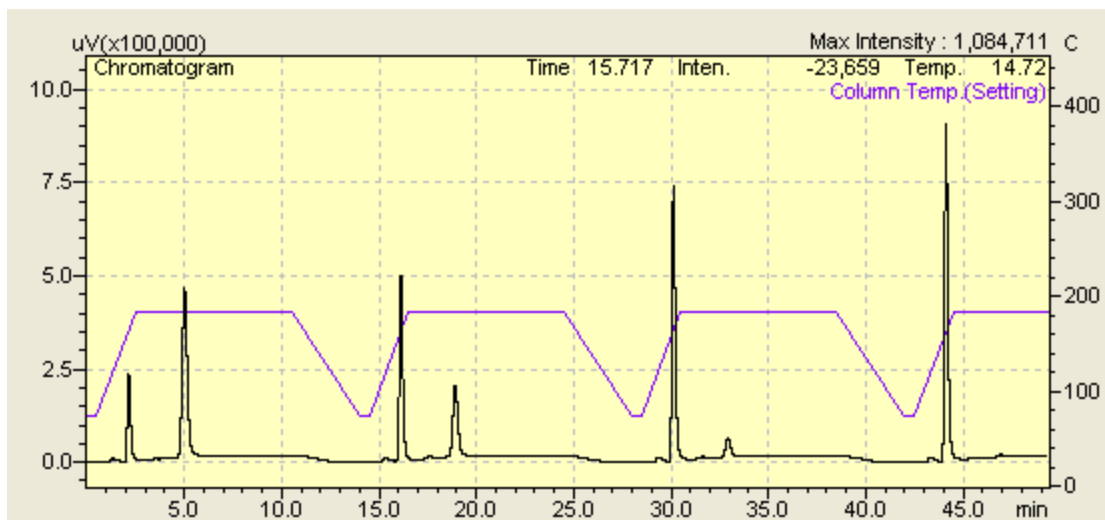


Figure 67: Full chromatogram obtained during the photodegradation of acetaldehyde in the Photo-CREC-Air reactor using automatized multi-injection

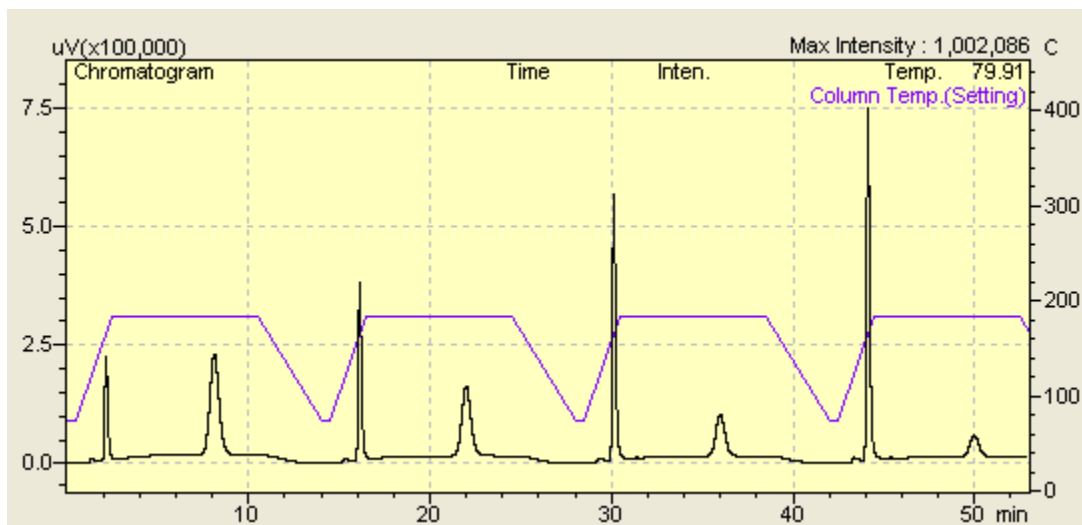


Figure 68: Full chromatogram obtained during the photodegradation of acetone in the Photo-CREC-Air reactor using automatized multi-injection

Different volume liquid (10-1000 ml) of the target organic compound was injected into the Photo-CREC-Air reactor (in dark conditions with no mesh) in order to evaluate the response in the FID detector. Calibration curves of acetone, acetaldehyde, CO₂ (Figure 69), methanol and formaldehyde (Figure 70) were completed. The calibration slopes are reported in Table 20.

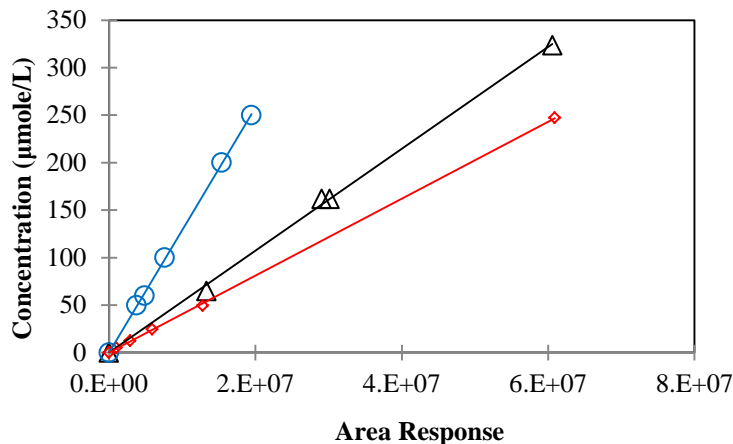


Figure 69: Calibration curves of acetone (red \diamond), acetaldehyde (black Δ) and CO₂ (blue \circ).

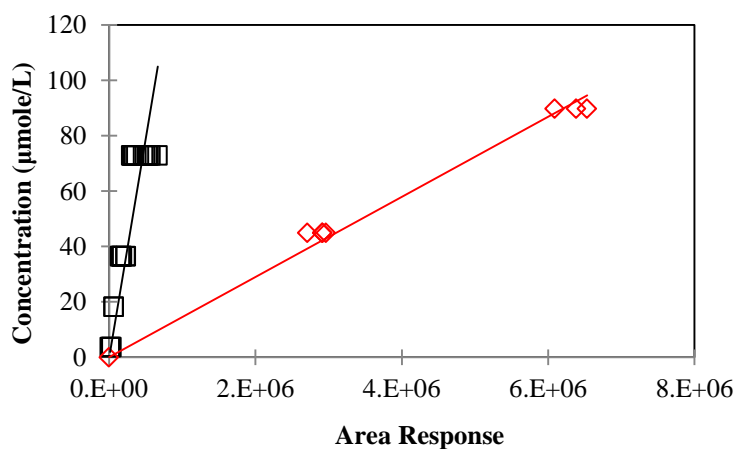


Figure 70: Calibration curves of methanol (red \diamond) and acetaldehyde (black \square).

Table 20. Calibration Slopes between FID Response and VOC Concentration in the Photo-CREC-Air Reactor

Compound	Calibration Slope ($\mu\text{mole/L-UA}$)
Acetone	4×10^{-6}
Acetaldehyde	5.4×10^{-6}
CO ₂	1×10^{-5}
Methanol	1.5×10^{-5}
Formaldehyde	1×10^{-4}

Appendix F: Photo-CREC-Air Reactor Leaks

The leaks in the Photo-CREC reactor were tested by pressurizing the unit with air. The reaction section, Venturi section and cooler are completely sealed. However, the compressor shows a minor leak on the impeller. The leaks in the reactor were monitored by injecting a set volume of acetone or CO₂ and the concentration loss was evaluated at dark conditions with no mesh. CO₂ shows a decay of 0.03% loss per minute while acetone shows a 0.045% loss per minute. The photodegradation reactions involve at least 2% degradation per minute. This means that the leak represents just about 2-3% of error in the experiments. The leak is included with the 10% of regular experimental error and therefore is not considered representative.

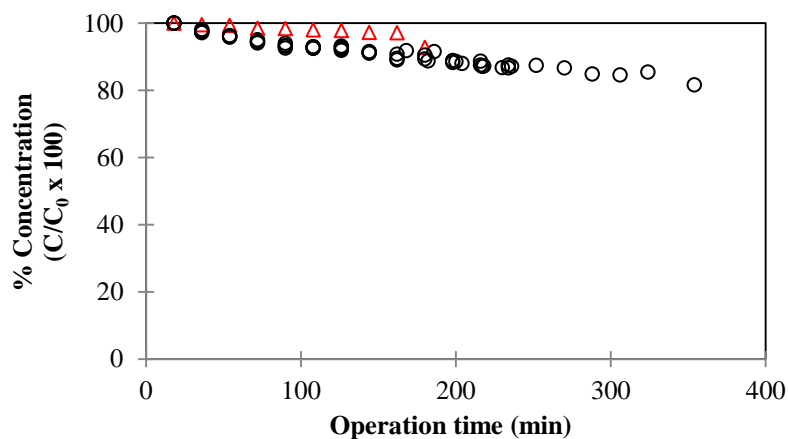
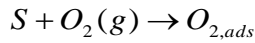


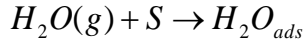
Figure 71: Concentration monitoring of acetone (black ○) and CO₂ (red Δ) with time at dark conditions with no mesh. A wide concentration range was considered (25-250 μmole/L).

Appendix G: Evaluation of the Heat of Formation of OH[•] Groups.

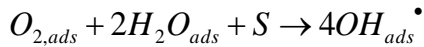
The calculation of the enthalpy of formation of hydroxyl radicals according with Figure 27, involves different thermodynamic states. The thermodynamic states include the energy of formation of hydroxyl radicals starting from oxygen and water in the gas phase as follows,



$$\Delta H_1 = \Delta H^\circ_{f,O_2,ads} - \Delta H^\circ_{f,O_2(g)} \quad (G-1)$$

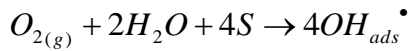


$$\Delta H_2 = \Delta H^\circ_{f,H_2O,ads} - \Delta H^\circ_{f,H_2O(g)} \quad (G-2)$$



$$\Delta H_3 = 4\Delta H^\circ_{f,OH^\bullet_{ads}} - 2\Delta H^\circ_{f,H_2O_{ads}} - \Delta H^\circ_{O_{2,ads}} \quad (G-3)$$

The addition of these three steps for the calculation of overall enthalpy is written as,



$$\Delta H_T = \Delta H_1 + 2\Delta H_2 + \Delta H_3 \quad (G-4)$$

$$\Delta H_T = \left[\Delta H^\circ_{f,O_2,ads} - \Delta H^\circ_{f,O_2(g)} \right]$$

$$+ 2 \left[\Delta H^\circ_{f,H_2O,ads} - \Delta H^\circ_{f,H_2O(g)} \right]$$

$$+ \left[4\Delta H^\circ_{f,OH^\bullet_{ads}} - 2\Delta H^\circ_{f,H_2O_{ads}} - \Delta H^\circ_{O_{2,ads}} \right] \quad (G-5)$$

$$\Delta H_T = 4\Delta H^\circ_{f,OH^\bullet_{ads}} - \Delta H^\circ_{f,O_2(g)} - 2\Delta H^\circ_{f,H_2O(g)} \quad (G-6)$$

Rewriting eq. (G-6) for the formation of one mole of hydroxyl radicals,

$$\Delta H_{OH^\bullet} = \frac{\Delta H_T}{4} = \Delta H^\circ_{f,OH^\bullet_{ads}} - \frac{1}{4} \Delta H^\circ_{f,O_2(g)} - \frac{1}{2} \Delta H^\circ_{f,H_2O(g)} \quad (G-7)$$

Where the enthalpy of formation of oxygen and water are given by,

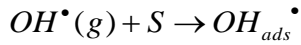
$$\Delta H^{\circ}_{f,O_2(g)} = 0 \text{ J/mol}$$

$$\Delta H^{\circ}_{f,H_2O(g)} = -241,820 \text{ J/mol}$$

The enthalpy of formation of the hydroxyl radicals can be calculated from the reported energy (Hussain, Gracia, Nieuwenhuys, & Niemantsverdriet, 2010) of hydroxyl radical adsorption,

$$\Delta H^{\circ}_{OH^{\bullet}ads} = -96,352 \text{ J/mol}$$

The enthalpy of hydroxyl radical formation on TiO_2 is defined by,



$$\Delta H^{\circ}_{OH^{\bullet}ads} = \Delta H^{\circ}_{f,OH^{\bullet}ads} - \Delta H^{\circ}_{f,OH^{\bullet}(g)} \quad (G-8)$$

From this definition, it is possible to find the enthalpy of hydroxyl radical formation using the following approach,

$$\Delta H^{\circ}_{f,OH^{\bullet}ads} = \Delta H^{\circ}_{OH^{\bullet}ads} + \Delta H^{\circ}_{f,OH^{\bullet}(g)} \quad (G-9)$$

$$\Delta H^{\circ}_{f,OH^{\bullet}(g)} = 37,028 \text{ J/mol}$$

$$\Delta H^{\circ}_{f,OH^{\bullet}ads} = -96,352 \text{ J/mol} + 37,028 \text{ J/mol} = -59,324 \text{ J/mol} \quad (G-10)$$

And finally to calculate the enthalpy required to produce an adsorbed radical starting from oxygen and water, these results in the following,

$$\Delta H_{OH^{\bullet}} = -59,324 \text{ J/mol} - \frac{1}{2}[-241,820 \text{ J/mol}] = 61,586 \text{ J/mol} \quad (G-11)$$

Appendix H: Radiative Transfer for Photon Absorption in the Film

The Radiative Transfer Equation for non-relativistic calculations at low temperatures is:

$$\frac{dI(s, \Omega)}{ds} = -\kappa I(s, \Omega) - \sigma I(s, \Omega) + \frac{\sigma}{4\pi} \int_0^{4\pi} I(s, \Omega') \Phi(\Omega, \Omega') d\Omega' \quad (\text{H-1})$$

where s and Ω represent position and solid angle respectively, I accounts for the spectral specific intensity of radiation (einsteins/m²-s-sr), κ represents the absorption coefficient (m⁻¹), σ is the scattering coefficient (m⁻¹), and Φ stands for the phase function for scattering phenomena. However for a thin layer of scattering and absorbing media, such as a photocatalyst layer, the equation can be simplified assuming that the irradiance field can be adequately described by considering radiation can only travel in two directions. This assumption then leads to the following set of equations:

$$\frac{dI^+(x)}{dx} = -(\kappa + \sigma) I^+(x) + \sigma [I^+(x) P_f + I^-(x) (1 - P_f)] \quad (\text{H-2})$$

$$\frac{dI^-(x)}{dx} = -(\kappa + \sigma) I^-(x) + \sigma [I^-(x) P_f + I^+(x) (1 - P_f)] \quad (\text{H-3})$$

where x represents depth in the photocatalyst layer (m), I^+ stands for the radiative intensity flowing in the positive direction (einsteins/m²-s-sr), I^- accounts for the radiative flux flowing on the opposite direction (einsteins/m²-s-sr) and finally:

$$P_f = \int_0^1 \Phi(\mu) d\mu \quad (\text{H-4})$$

where μ represents the cosine of the scattering angle. Additionally, given that a system of two linear first order, odes are obtained, two boundary conditions are required. The boundary conditions are:

$$I^+(x = 0) - I^-(x = 0) = \phi \quad (\text{H-5})$$

$$R I^+(x = L) - I^-(x = L) = 0 \quad (\text{H-6})$$

where R is the reflectance of the photocatalyst-support interface and ϕ represents the total radiation absorbed by the photocatalyst layer at every given location (einsteins/m²-s-sr), obtained from a suitable Monte Carlo simulation for a give photoreactor geometry. The

system can be solved by using the method of eigenvalues-eigenvectors, where the following equations are obtained:

$$I^+(x) = C_1 e^{(\gamma(2P_f-1)-1)\beta x} + C_2 e^{(\gamma-1)\beta x} \quad (\text{H-7})$$

$$I^-(x) = -C_1 e^{(\gamma(2P_f-1)-1)\beta x} + C_2 e^{(\gamma-1)\beta x} \quad (\text{H-8})$$

where γ is the albedo and β is the extinction coefficient. Finally, by applying the corresponding boundary conditions the values of the integration constants are found to be:

$$C_1 = \frac{\phi}{2} \quad (\text{H-9})$$

$$C_2 = -\frac{\phi}{2} \left(\frac{R+1}{R-1} \right) e^{2\gamma(P_f-1)\beta L} \quad (\text{H-10})$$

From these expressions for the irradiance field, the local volumetric rate of energy absorption (LVREA) can be determined, given that by definition:

$$\varphi(s) = \kappa \int_0^{4\pi} I(s, \Omega) d\Omega \quad (\text{H-11})$$

and under the current assumption of a two flux model, the LVREA equation above, would simplify to:

$$\varphi(x) = \kappa [I^+(x) + I^-(x)] \quad (\text{H-12})$$

which ultimately leads to:

$$\varphi(x) = \kappa \phi \left(\frac{R+1}{R-1} \right) e^{-2\sigma P_b L} e^{-\kappa x} \quad (\text{H-12})$$

where P_b represents the fraction of radiation being back scattered by the effective medium approximation on the photocatalyst layer, i.e. $P_f + P_b = 1$.

Appendix I: Electron-hole Kinetics

If a simplified model for photodegradation is considered such that a balance for the hole-electron hole-pairs can be established as:

$$\frac{d[h^+]}{dt} = \varphi - k_r[h^+][e^-] - (k_{h1}[OH^-_{ads}] + k_{h2}[H_2O_{ads}])[h^+] \quad (I-1)$$

$$\frac{d[e^-]}{dt} = \varphi - k_r[h^+][e^-] - k_e[O_{2ads}][e^-] \quad (I-2)$$

where φ is the number existent charged species, k_r , k_{h2} , k_{h1} , k_e account for the reaction rate of electron-hole recombination, reaction A-1, reaction A-2 and reaction A-3 respectively.

Assuming stationary state for both charge balances (Zhang, Mohamed, Dillert, & Bahnemann, 2012), and assuming things such as pH, humidity, oxygen, and irradiance remain relatively stable throughout the experiment, then:

$$[h^+] = \frac{[O_{2ads}] k_e}{k_r} \left[\sqrt{\left(\frac{4k_r}{k_e[O_{2ads}] (k_{h1}[OH^-_{ads}] + k_{h2}[H_2O_{ads}])} \right) \varphi + 1} - 1 \right] \quad (I-3)$$

$$[e^-] = \frac{(k_{h1}[OH^-_{ads}] + k_{h2}[H_2O_{ads}])}{k_r} \dots$$

$$\dots \left[\sqrt{\left(\frac{4k_r}{k_e[O_{2ads}] (k_{h1}[OH^-_{ads}] + k_{h2}[H_2O_{ads}])} \right) \varphi + 1} - 1 \right] \quad (I-4)$$

From these expressions, free radical generation (source term) could be described by:

$$\frac{d[OH^\bullet]}{dt} = k_e[h^+][e^-] + (k_{h1}[OH^-_{ads}] + k_{h2}[H_2O_{ads}])[h^+] - \sum f(C) [OH^\bullet] \quad (I-5)$$

where free radical generation, accumulation and degradation are considered. Assuming pseudo steady state for the free radical balance and substituting the expressions for the $[e^-]$ and $[h^+]$:

$$R_{oxidation} = \eta f(C) \quad (I-6)$$

where,

$$\eta = A(\sqrt{B\phi + 1} - 1) \quad (I-7)$$

Accounting for radiative losses and charge recombination which hinder photocatalytic performance of a given system, the constants A and B represent the following,

$$A = \frac{(k_{h1}[OH^-_{ads}] + k_{h2}[H_2O_{ads}])}{k_r} (k_e[H^+] + [O_{2ads}] k_e) \quad (I-8)$$

$$B = \left(\frac{4k_r}{k_e[O_{2ads}] (k_{h1}[OH^-_{ads}] + k_{h2}[H_2O_{ads}])} \right) \quad (I-9)$$

The following expressions can be found in the literature, under different considerations. However, equation $\eta = A(\sqrt{B\phi + 1} - 1)$ has been experimentally validated on slurry reactors, considering different photocatalyst loadings, photoreactor geometries, and irradiance conditions (Valadés-Pelayo et al., 2015a, 2015b; Valadés-Pelayo et al., 2014; P. J. Valades-Pelayo et al., 2014).

Appendix J: Physical Based Model for Photoactivity on the Film as a Function of Coating Thickness.

The expressions presented in the section for radiative transfer (Appendix H) and the ones obtained in the chemical kinetics section (Appendix I), can be combined in order to obtain an expression that helps us determine the photocatalytic performance of the supported photocatalyst layer. One should keep in mind, that the boundary condition ϕ , must be determined by Monte Carlo ray-tracing techniques when geometries are complicated, as is the case on the Photo-CREC-Air reactor.

According to the radiative transfer section, the dependence of the absorption field in an absorbing-scattering photocatalyst layer can be approximated by:

$$\varphi(x) = \kappa \phi \left(\frac{R+1}{R-1} \right) e^{-2\sigma P_b L} e^{-\kappa x} \quad (\text{J-1})$$

where P_b represents the probability of absorption (high forward scattering media with $P_b=0.01$).

On the other hand, the photocatalytic dependence on the absorbed radiation, according to our simplified model is:

$$\eta = A(\sqrt{B\varphi + 1} - 1)f(C) \quad (\text{J-2})$$

A porous layer will be considered, such that the reaction is not confined to the photocatalyst layer surface, but instead reaction takes place within the layer. We can substitute φ into R , to obtain:

$$\eta = A \left(\sqrt{B\kappa \phi \left(\frac{R+1}{R-1} \right) e^{-2\sigma P_b L} e^{-\kappa x} + 1} - 1 \right) \quad (\text{J-3})$$

where B represents the extinction coefficient (m^{-1}) of the semiconductor. An extinction coefficient B of $0.6 \mu\text{m}^{-1}$ (within the range of anatase), albedo of 0.87 (reported for Degussa P25).

This equation can then be integrated within the whole layer:

$$\bar{\eta} = \int_0^L \eta(x) dx \quad (\text{J-4})$$

where, $\bar{\eta}$ represents the photocatalytic efficiency applied within the whole photocatalyst layer. Once integration is done, one is left with the following equation:

$$\bar{\eta} = A \left[u(0) - u(L) + \ln \left(\frac{u(L) + 1}{u(0) + 1} \right) \right] \quad (\text{J-5})$$

where:

$$u(x) = \left(B\kappa\phi \left(\frac{1+R}{1-R} \right) e^{-2\sigma P_b L} * e^{-\kappa x} + 1 \right)^{1/2} \quad (\text{J-6})$$

within the scope of the following experimental set-up, model parameters will be lumped in the following way:

$$B^* = B\kappa\phi \left(\frac{1+R}{1-R} \right) \quad (\text{J-6})$$

Appendix K: Parameter Estimation Coding for Differential Equations.

```

k1 = k(1);
k2 = k(2);
k3 = k(3);
%k3 = k(3);
%k2 = 0.0456;% Adsorption Constant L\microMol

Kpa = 0.15; %K linear adsorption for acetone dimensionless
Kpb=0.04; %K linear adsorption for acetaldehyde dimensionless
Ka=0.0456; %Adsorption constant L/microMol
Kb=0.0092; %Adsorption constant L/microMol

denominator = (1+Ka*y(1)+Kb*y(3));

r1 = ((k1+k2)*Ka*y(1))/(1+Kpa)/denominator;
r2 = ((k1+3*k2)*Ka*y(1)+2*k3*Kb*y(3))/denominator;
r3 = (k1*Ka*y(1)-k3*Kb*y(3))/(1+Kpb)/denominator;

F(1) = -r1;      %Acetone degradaton
F(2) = r2;      %CO2 producion
F(3) = r3;      %Acetaldehyde
F=F';

```

Figure 72: Differential equations in MATLAB code for parameter estimation.

Photodegradation of acetone with acetaldehyde as intermediate species was considered.

```
function F=Diff_EquationsAllT(t,y,k)
% System of ODE for the Kinetic Modeling
%t = independent Variable and y = Vector with the dependent variables
%
k1 = k(1);
k2 = 0.0456;% Adsorption Constant L\microMol

denominator = (1+k2*y(1));

r1 = k1*y(1)*0.85/(denominator);
r2 = 3*k1*y(1)/denominator;

F(1) = -r1;      %Acetone degradaton
F(2) = r2;      %CO2 produccion

F=F';
```

Figure 73: Differential equations in MATLAB code for parameter estimation. Photodegradation of acetone with no intermediate species was considered.


```

function F=Diff_EquationsAllT(t,y,k)
% System of ODE for the Kinetic Modeling
%t = independent Variable and y = Vector with the dependent variables
%
k1 = k(1); %Acetaldehyde to 1 C species
k2 = k(2); %Acetaldehyde to CO2
k4 = k(3); %1C species to CO2

Ka=0.0092; %Adsorption constant of acetaldehyde L/microMol
Kd=0.1; %Adsorption constant of 1 C species L/microMol
V=55.08; %Volume in L
m= 2.2; %photocatalyst weight
Airr=1042; %Irradiated area in cm2

ADS = (1+Ka*y(1)+Kd*y(3));
ADSp=ADS;

%Linear adsorption constants
kap=0.79*m/V;
kbp=3*m/V;
kdp=3.9*m/V;
kep=1.165*m/V;

a1 = k1*Ka*y(1); %Acetaldehyde to 1 C species
a2 = k2*Ka*y(1); %Acetaldehyde to CO2
d1 = k4*Kd*y(3); %Formaldehyde to CO2
r1 = -(a1+a2)/((1+kap)*ADSp);
r2 = (2*a2+d1)/ADSp;
r3 = (2*a1-d1)/(ADSp*(1+kdp));
F(1) = r1; %Acetaldehyde
F(2) = r2; %CO2 production
F(3) = r3; %1C Species
F=F';

```

Figure 74: Differential equations in MATLAB code for parameter estimation. Photodegradation of acetaldehyde with enclosed 1 carbon intermediate species was considered.

Curriculum Vitae

Name: Cristina Lugo Vega

Post-secondary Education and Degrees: Autonomous University of San Luis Potosi
San Luis Potos, S.L.P., Mexico
2004-2008 B.A.

Autonomous University of San Luis Potosi
San Luis Potos, S.L.P., Mexico
2009-2011 M.A.

The University of Western Ontario
London, Ontario, Canada
2012-2016 Ph.D.

Honours and Awards: North American Mobility Program Scholarship
NAMP, Mexico
2009

Council for Science and Technology Scholarship
CONACyT, Mexico
2009-2011

Council for Science and Technology Scholarship
CONACyT, Mexico
2012-2016

Chemical and Biochemical Engineering Seminar Series
Fall Seminar Speaker Award
2015

Related Work Experience Teaching Assistant
The University of Western Ontario
2013-2016

Research Assistant
The University of Western Ontario
2013-2016

Analytical Chemist
Minera Mexico
2012

Professor
 Technological University of San Luis Potosi
 2011-2012

Research Assistant
 Autonomous University of San Luis Potosi
 2009-2011

Publications:

a) Refereed publications

Lugo-Vega C., Serrano B. and de Lasa H., Immobilized Particle Coating for Optimum Photon and TiO₂ Utilization in Scaled Air Treatment Photo Reactors, *Applied Catalysis B: Environmental*, 198, 2011-2023, **2016**.

Lugo-Vega C., Serrano B. and de Lasa H., Energy efficiencies in Photo-CREC Air Photocatalytic Reactors, *Chemical Engineering Science*, Accepted on August 27, **2016**.

Lugo-Vega C., Moreira J., Serrano B. and de Lasa H., Kinetic Analysis Methodologies using Series-Parallel Models in Photo-CREC-Air Reactors , To be submitted to *Industrial & Engineering Chemistry Research* in September **2016**.

Lugo-Vega C., Valadez-Pelayo P., Serrano B. and de Lasa H., Validation of a Photon Absorption Physically Based Model in Supported TiO₂ films for Photo-CREC-Air Reactors, To be submitted to *Chemical Engineering Science* in December **2016**.

b) Oral Presentations:

Lugo-Vega C. Serrano B. and de Lasa H., “A TiO₂ Immobilized Coating Prepared via Spray Drying for a Photo-CREC Air Reactor”, Mexican Academy of Research and Education in Chemical Engineering (AMIDIQ), Puerto Vallarta, Mexico, **2016**.

Lugo-Vega C. de Lasa H. Serrano-Rosales B., “A TiO₂ Immobilized Coating Prepared Via Spray Drying for a Photo-CREC-Air Reactor”, International Congress of Chemical and Process Engineering CHISA, Invited Key Note Lecture, Prague Czech Republic, **2016**.

Lugo-Vega C. Serrano B. and de Lasa H., “A New Spray Coating Method for TiO₂ Immobilization in a Photo-CREC-Air Reactor”, American Institute of Chemical Engineering AICHE meeting, Salt Lake City, USA, **2015**.

Lugo-Vega C., Serrano B. and de Lasa H., “Photocatalytic conversion of Organic Pollutants in Air with High Quantum Yields in the Photo-CREC Air Unit”, Canadian Society for Chemical Engineering (CSChE) meeting, Niagara Falls, Canada, **2014**.

Sanchez-Castillo M.A., **Lugo-Vega C.** and Cruz-Barba L.E., “Selective and sequential functionalization of activated carbon using a rotatory DBD reactor”, Asia-Pacific Conference on Plasma Science and Technology (APCPST), Kyoto, Japan, **2012**.

Lugo-Vega C., Sanchez-Castillo M., “Surface Tailoring of Catalyst Supports with Non-isothermal Plasma Technology for Catalyst Design”, International Conference of the Mexican Association on Research and Education in Chemical Engineering, San Luis Potosi, Mexico, **2010**.